

Cutting the Last Cord with Wireless Power

Alanson Sample

A dissertation submitted in partial fulfillment of
the requirements for the degree of

Doctor of Philosophy

University of Washington

2011

Program Authorized to Offer Degree: Electrical Engineering

University of Washington
Graduate School

This is to certify that I have examined this copy of a doctoral dissertation by

Alanson Sample

and have found that it is complete and satisfactory in all respects,
and that any and all revisions required by the final
examining committee have been made.

Chair of the Supervisory Committee:

Joshua R. Smith

Reading Committee:

Joshua R. Smith

Brian Otis

Patel Shwetak

Date: _____

In presenting this dissertation in partial fulfillment of the requirements for the doctoral degree at the University of Washington, I agree that the Library shall make its copies freely available for inspection. I further agree that extensive copying of this dissertation is allowable only for scholarly purposes, consistent with "fair use" as prescribed in the U.S. Copyright Law. Requests for copying or reproduction of this dissertation may be referred to Proquest Information and Learning, 300 North Zeeb Road, Ann Arbor, MI 48106-1346, 1-800-521-0600, or to the author.

Signature_____

Date_____

University of Washington

Abstract

Cutting the Last Cord with Wireless Power

Alanson Sample

Chair of the Supervisory Committee:

Associate Professor Joshua R. Smith

Computer Science & Engineering and Electrical Engineering

Wireless power technology offers the possibility of "cutting the last cord", thereby removing the last remaining wired connections required to power and recharge our electronic devices. A long standing goal has been to seamlessly deliver wireless power to large areas, thereby enabling users the freedom and mobility to use their devices in an unencumbered fashion. The realization of this paradigm would enable an expansive array of new consumer electronic devices and usage models. Additionally, it would create implanted medical devices capable of long term sensing and actuation and would enable embedded sensors and sensor networks capable of nearly unlimited operational life times.

However, existing technology falls short of this vision. Inductive charging solutions are limited in range/orientation and require a docking station or precise placement for effective operation. Far-field wireless power techniques have greater range, but have limits on the maximum allowable power transmitted for safety reasons. As a result, existing far-field wirelessly powered devices, such as RFID tags, are extremely limited in capability.

This dissertation explores several methods of wirelessly powering electronic devices and presents techniques for rectification, power management, and system design. Demonstrated transfer ranges vary from meters to kilometers. While delivered power levels vary from microwatts to tens of watts. The methods presented provide wireless power to large volumes of space, rather than surface or point charging, and insures safety for the general public.

The first topic uses magnetically coupled resonators for wireless power delivery. New

analysis is presented that yields critical insight into key system concepts, such as frequency splitting, the maximum operating distance (critical coupling), and the behavior of the system as it becomes under-coupled. A new theoretical model has been developed and is validated against measured data, and shows an excellent agreement. An adaptive frequency tuning technique is demonstrated, which compensates for efficiency variations encountered when the transmitter to receiver distance and/or orientation are varied. This method allows the receiver to be moved to nearly any position and/or orientation within the range of the transmitter and still achieve a near constant efficiency of over 70% for a ranges of 0-70 cm. As an example application a wirelessly power laptop is demonstrated.

The second focus of this dissertation is on devices powered by far-field power transfer techniques. First, The Wireless Identification and Sensing Platform (WISP) has been developed as a programmable, battery-free sensing and computational platform, designed to explore sensor-enhanced radio frequency identification (RFID) applications. The WISP uses a 16-bit, ultra-low power microcontroller to perform sensing and computation, while exclusively operating from harvested RF energy at a range of 4.3 meters. Applications described in this document include photovoltaic enhanced RFID antennas for dual purpose energy harvesting and a capacitive touch interface for RFID tags. Our team has open sourced the WISP, and to date there are over 50 universities and research groups around the world actively working with it.

Additionally, the Wireless Ambient Energy Power (WARP) project has successfully demonstrated the ability to harvest ambient radio waves and use them to power both a commercially available home weather station and a custom built wireless sensor node. The node is capable of harvesting energy, sensing the environment, performing computation, and communicating wirelessly with a base station. The sensor node has been tested at a distance of 4.1 kilometers from a 916kW TV tower, resulting in an operational area of several tens of square kilometers, assuming line of sight to the tower.

TABLE OF CONTENTS

	Page
List of Figures	iii
List of Tables	viii
Chapter 1: Introduction	1
1.1 Motivation	1
1.2 Scope of Proposed Research	3
1.3 Dissertation Organization	5
Chapter 2: Background	6
2.1 Modern Wireless Power Systems	7
2.2 Electromagnetic Safety for Wireless Power Systems	9
2.3 Friis Path Loss and Moore's Law	11
Chapter 3: Wireless Resonant Energy Link	15
3.1 System Overview	16
3.2 Circuit Model and Transfer Function	18
3.3 Derivations of critical coupling and system parameters	22
3.4 Parameter Extraction and Measurement Techniques	25
3.5 Validation of Circuit Model and Measured Results	33
3.6 Adaptive Tuning for Range Independent Maximum Power Transfer	41
3.7 Summary	45
Chapter 4: Wireless Identification and Sensing Platform	49
4.1 Prior work	49
4.2 WISP Overview	50
4.3 Firmware & Power Management Algorithm	57
4.4 Power Budget	61
4.5 Communicating with the WISP	65
4.6 Experimental Results	68

Chapter 5: Photovoltaic Enhanced UHF RFID Tag Antennas	71
5.1 Motivation	71
5.2 System Overview	73
5.3 Two Solar-Enhanced RFID Antenna Designs	76
5.4 Reader Independent Operation	86
5.5 Summary	91
Chapter 6: A Capacitive Touch Interface for Passive RFID Tags	93
6.1 Motivation	93
6.2 Passive RFID Capacitive Sensing Architecture	95
6.3 Implementation and Experimental Results	98
6.4 Applications	103
6.5 Summary	108
Chapter 7: Wireless Ambient Radio Power	110
7.1 WARP TV Harvester	110
7.2 WARP Sensor Node	113
7.3 Summary	123
Chapter 8: Conclusion	125
8.1 Dissertation Summary	125
8.2 WISP Challenge	127
8.3 Future Work	128
Bibliography	134

LIST OF FIGURES

Figure Number	Page
2.1 Range scaling of radiative wirelessly powered devices. Upper line (left scale): microprocessor efficiency, measured in instructions per μJ . The doubling time is approximately 2 years. Lower line (right scale): range in meters at which sufficient power can be delivered wirelessly to run a workload of 60k instructions per second. Range doubling time is approximately 4 years for a constant computational load.	13
3.1 Sketch of the magnetically coupled resonant wireless power system consisting of an RF amplifier, on the left, capable of measuring the forward and reflected power. A two element transmitter, made of a signal turn drive loop and high Q coil, wirelessly powers the receiver on the right.	16
3.2 Equivalent circuit model of the wireless power system. Each of the four antenna elements are modeled as series resonators, which are linked by mutual inductances via coupling coefficients.	19
3.3 S_{21} magnitude as a function of frequency and transmitter to receiver coupling k_{23} for the simplified circuit model given the values in table I. The highlighted red volume is the over coupled regime, where frequency splitting occurs and transfer efficiency can be maintained independent of distance if the correct frequency is chosen.	21
3.4 Efficiency vs. critical coupling range: $ S_{21} _{critical}$ vs. $k_{critical}$ trade off curve as a function of the tuning parameter k_{lc} , with our system's operating point indicated (large dot at $k_{lc}=0.135$).	24
3.5 Photograph of the transmitter and receiver used in the wireless power system. For scale the outside diameter of the large coils is 59 cm.	27
3.6 Circuit diagram of the drive loop (left) and measured and extracted S_{11} data (right).	29
3.7 Circuit diagram of drive loop and transmit coil along with (left) and measured and extracted S_{11} data (right).	29
3.8 Concentric ring approximation for a spiral coil.	31
3.9 Approximation for calculating the mutual inductance of two coaxial spiral coils.	32

3.10 Comparison of experimental data (black dots) to the simplified transfer function (dotted blue line), and to the complete transfer function (red line). The simple model neglects parasitic cross coupling (e.g. k_{13}, k_{24}, k_{14}) and does not reproduce the amplitude difference between the upper and lower modes. The complete model reproduces this amplitude difference, which is explained by the phase of the parasitic coupling terms (k_{13}, k_{24}) relative to the non-parasitic terms (e.g. k_{23}) for the two resonant modes.	35
3.11 Measured $ S_{21} $ data (black dots) plotted in magnitude form. Each row of black dots represents a frequency sweep taken by the VNA every 5cm as the receiver was moved away from the transmitter. The mesh underneath the data is the theoretical model.	37
3.12 Diagram depicting the top view of the experimental setup where the receiver, as a single unit, is moved away from the transmitter. In this experiment the free variable is the coil to coil coupling (k_{23}) which varies as a function of the distance between the coils.	38
3.13 Predicted behavior of the wireless power system at the individual coil resonant frequency (f_o) using Neumann's formula along with the predicted critical coupling point (blue dot) and S_{21} measured data.	39
3.14 Calculated and measured frequency splitting plotted as a function of distance. The S_{21} magnitude of the two modes is shown on the left and frequency of the two modes is shown on right.	40
3.15 Extracted coupling coefficient with confidence bars and calculated coupling coefficients using the Neumann's formula (red line)	41
3.16 Automatic frequency tuning compared to a fixed drive frequency as a function of distance between the transmitter and receiver.	42
3.17 Diagram depicting the top view of the experimental setup where the receiver, as a single unit, is moved away from the transmitter. In this experiment the free variable is the coil to coil coupling (k_{23}) which varies as a function of the distance between the coils.	43
3.18 Automatic frequency tuning compared to a fixed drive frequency as a function of the angle between the transmitter and receiver. An angle of 0° degree corresponds to the coils facing each other, while 90° degrees corresponds to the receiver perpendicular to the transmitter. The transmitter to receiver spacing is 0.5 meters.	44
3.19 Diagram depicting the top view of the experimental setup where the orientation of the receiver is varied by angle θ at a fixed distance from the transmitter.	44
3.20 The magnitude of power transfer ($ S_{21} $) as a function of the coil to coil coupling (k_{23}) vs the loop to coil coupling (where $k_{12} = k_{34}$). This plot shows that given a particular range (i.e. k_{23}) there exists a loop to coil coupling that will maximize power transfer.	46

3.21	Wirelessly powered laptop computer. The battery has been removed and is visible in the lower right of the table. The wireless power system is able to provide all of the laptop's peak power consumption of 12 Watts at a range of 0.7 meters. Including the rectifier (which has not yet been optimized), the system efficiency (measured from amplifier output through to the laptop) is 50%.	48
4.1	Block Diagram of the WISP	51
4.2	Wireless Identification and Sensing Platform (WISP), version G2.0	52
4.3	WISP Data logger, version 4.0DL	52
4.4	Blue WISP, version 4.1DL	53
4.5	Schematic of the Analog Front End.	54
4.6	Oscilloscope plot of the demodulated data extracting data from the RF waveform transmitted by the RFID reader.	56
4.7	Block diagram of the power management algorithm for the WISP	59
4.8	Oscilloscope plot of the WISP responding to EPC queries along with its rectified voltage.	61
4.9	Rectified voltage (left scale) and output power at 1.9V (right scale) are plotted versus input power measurements using multi-meter and network analyzer for RF signal insertion into the antenna ports.	63
4.10	WISP performance: harvested voltage, Uplink Packet Errors, and Responses per Query as a function of input power.	70
5.1	Conceptual diagram of a solar-enhanced RFID tag antenna with RFID IC. VCC is connected to the positive bus of the solar cell via a high-impedance trace. RF2 and Ground are connected to the same port of the antenna, and RF1 is connected opposite them.	75
5.2	Diagram of the photovoltaic-enhanced antenna for an RFID IC. Solid black lines denote copper traces. The gray section represents the solar cell. A small, thin trace connects the positive terminal (bottom) of the solar cell to the IC, providing DC power. Lengths are given in mm, and trace widths are 1mm and 2mm.	77
5.3	Image of the photovoltaic-enhanced RFID antenna connected to an Alien Higgs-3 SOT-323 packaged RFID IC. The solar cell is manufactured by PowerFilm Inc. part number #SP3-37. The completed tag prototype has been mounted to a 1mm thick layer of Plexiglas for rigidity. This tag shows the viability of incorporating photovoltaics into RFID antennas while maintaining RF performance.(For clarity, this IC does not accept solar power)	79

5.4	Simulated and measured input impedances for the IC specific solar antenna. The bottom group of traces shows the real impedance and the top group shows the complex. Measurements show a small deviation between the copper version of the antenna and the antenna that incorporates the solar cell.	80
5.5	Read range of the prototype photovoltaic-enhanced RFID tag, using the Higgs-3 IC. Solar power was not used by the IC.	81
5.6	Solar-enhanced antenna design for WISP-based tag.	82
5.7	Inverted F antenna constructed from a solar cell and connected to the WISP.	83
5.8	Read rate as a function of distance for WISP tags using the solar-enhanced antenna. Equivalent distance is calculated assuming a 1 Watt transmitter and a 6 dBi transmit antenna.	85
5.9	Passive solar antenna-based data logger on a parcel.	87
5.10	State diagram for solar-enhanced, data-logging WISP.	88
5.11	Temperature and orientation data recorded by the solar-enhanced RFID platform during a simulated parcel shipment.	90
6.1	Block diagram of the capacitive touch sensor enhanced RFID tag. The antenna forms a sensing capacitor at low frequencies and its RC discharge rate is measured with the digital timer.	97
6.2	Image of the passive UHF RFID tag with a capacitive touch input and LED output for feed back.	99
6.3	Simulated and experimental results showing the S11 response of the RFID touch antenna when active by the user's finger and when left on touched.	102
6.4	Two RFID tag touch measurement events showing EPC Gen2 protocol and senses capacitor RC discharge. The top plot shows the untouched event and the bottoms plot shows the increase in discharge rate caused by the added capacitance of the user's finger.	104
6.5	Raw capacitive sensor data and identified touch events transmitted to the RFID reader form the RFID tag.	105
6.6	Touch enhanced UHF near-field RFID tag in the form factor of a credit card	107
7.1	Position 'A' indicates the location of the KING-TV tower which transmits 960 kW. The contour rings estimate the available receive power for the Seattle region (assuming line of sight and a 5dBi receive antenna).	111
7.2	Demonstration of a temperature and humidity meter (including LCD display) that is exclusively powered from ambient RF signals transmitted by the TV tower seen in the background, at a distance of 4.1 km.	112
7.3	Conceptual diagram of a deployment of WARP sensor nodes. The WARP nodes harvest ambient RF power from TV stations for operation and communicate back to a base station using an onboard radio.	115

LIST OF TABLES

Table Number	Page
3.1 Circuit Values Used to Evaluate the Simplified Model	22
3.2 Measured lumped elements values for each individual circuit elements of the experimental transmitter and receiver.	33

DEDICATION

to my dear wife, Brittany

Chapter 1

INTRODUCTION

Effective means of wireless power delivery can fundamentally change the way we interact with technology by eliminating the need for a wired connection for powering and recharging electronic devices. The focus of this research is to investigate methods of cutting that last cord, thereby enabling new devices and new applications. In the following section I provide motivation for this work by identifying several classes of applications that significantly benefit from wireless power. In the next section, I define the scope of my research and highlight several projects. Finally, I conclude this chapter with an organizational overview of the technical content presented in this dissertation.

1.1 Motivation

Wireless power technology offers the promise of “cutting the last cord,” allowing devices to be seamlessly powered and recharged as easily as data is transmitted through the air. The realization of this paradigm will fundamentally shift the way people use technology. Just as the advent of wireless communication technology has enabled an expansive array of mobile products, effective means of wireless power will allow for many new types of mobile devices and usage models to become feasible.

With ongoing advances in wireless communication and semiconductor technologies, consumer electronics, medical devices, and industrial equipment are becoming smaller, more portable, and typically more power hungry. However, users are still required to manually plug in these mobile devices, limiting ultimate mobility and disrupting use when the charge is depleted. Thus, there is the desire to augment these devices with wireless power capabilities to increase their mobility and reliability. One vision of wireless power is a “smart” cubical or work space, where a user’s devices are seamlessly powered and charged while he/she works. This could take the form of wirelessly charged computer peripherals, such

as mice, keyboards, hard drives, and monitors, which would effectively eliminate the tangle of wires and power adaptors that plague desks and conference rooms. It is also possible that such a work space could finally eliminate the need for users to constantly remember to recharge their personal devices, such as cell phones. Furthermore, as portable devices shrink in size, connectors become a larger fraction of the total system size. Wireless power offers the possibility of connector-free electronic devices, which could improve both size and reliability.

All of these applications require that the wireless power solution be capable of transferring large amounts of power (on the order of 10s of watts) efficiently and over distances ranging from a few centimeters up to a meter. Also, the wireless power system must be able to adapt to changes in the environment, whether it be variations in the distance and/or orientation of the transmitter to receiver, or changes in the power consumption of the load.

Aside from consumer electronics, there are other classes of applications, such as sensor nodes, that would greatly benefit from wireless power and recharging. For instance, embedded or implanted nodes that have the capability to sense the environment, perform computation, and communicate wirelessly have the potential to enable a wide range of applications, such as dense environmental monitoring, sensor rich home and work place automation, and self-identification and context awareness for everyday objects.

Towards these efforts, research on wireless sensor networks (WSNs) based on the mote sensing platform has been applied to many real-world problems, including wildlife, environment, and infrastructure monitoring. However, the lifetime of these devices is typically measured in weeks or months, making large-scale and/or long-term deployments impractical due to finite battery capacity and the resulting maintenance costs associated with battery replacement. Furthermore, the size, weight, and cost of batteries often limits the feasibility of many WSN applications.

On the other side of the sensor node spectrum are passive RFID tags. Passive tags are battery-free and powered wirelessly at a range of several meters. These tags are capable of wireless communication and rudimentary computation. While the functionality of today's passive RFID tags is extremely limited, they already represent an invisible layer of computing that is seamlessly embedded in many objects throughout our environment. Thus, there

is the desire to merge the best qualities of these two devices together, to enhance passive RFID tags with sensors and computing power, and to add wireless power capabilities to higher functioning sensor nodes.

1.2 Scope of Proposed Research

There are a variety of different wireless power transfer mechanisms that can be used to power consumer electronics and sensor nodes. Each method has its own unique strengths and weaknesses, which naturally lend themselves to different usage models (a detailed overview of these tradeoffs is presented in section 2.1).

First, a distinction is made between near-field and far-field wireless power transfer methods. The defining factor for far-field wireless power transmission is whether or not the power is broadcast as a propagating electromagnetic wave, which is launched from the antenna and does not return. This differs from near-field wireless power transmission, where energy is stored as a field in the vicinity of the antenna. Ideally, this energy is not lost or dissipated if unused by a load, rather the energy in the near-field is stored as expanding and collapsing fields, which oscillate in a cyclic manner. This region is referred to as the reactive near-field, and extends to a distance of approximately $r = \lambda/(2\pi)$. The beginning of the far-field region is approximated by the Fresnel parameter $r = D^2/(4\lambda)$, where D is the maximum overall dimension of the antenna. For the purposes of this report, we will not consider the area in between the reactive near-field and far-field regions, which is known as the radiative near-field. This region is characterized by complex and nonuniform \vec{E} and \vec{H} fields, which do not return to the antenna.

The second distinction is made between using deliberate or “planted” wireless power transmitters vs. unintended or “wild” sources of wireless power, such as ambient radio waves that can be harvested by a receiver. It is true that in most cases the optimal solution is to design a complete end-to-end system, consisting of a dedicated power transmitter and a receiver built into the end device; this is certainly the case for consumer electronics, which require large amounts of power and space efficient solutions. However, for sensor nodes that are inherently low in power and more flexible in form factor, it would be advantageous to harvest ambient radio waves so that dedicated power delivery infrastructure does not need

to be deployed in remote monitoring applications.

The Wireless Resonant Energy Link (WREL) project (pronounced “whirl”) uses RF resonators that are coupled magnetically to form a near-field wireless power transfer system. Potential applications include powering: cell phones, laptops, and TVs, as well as more specialized usages, such as implanted medical devices. One of the advantages is that magnetically coupled resonators (MCRs) can be used to transfer large amounts of power safely and efficiently over usable distances. However, this technology is not as mature as others, and a significant portion of this research is focused on analyzing and measuring the underlying power transfer mechanism. Additionally, I present an adaptive frequency tuning technique, which compensates for efficiency variations encountered when the transmitter to receiver distance and/or orientation is varied. The method demonstrated allows a fixed-load receiver to be moved to nearly any position and/or orientation within the range of the transmitter and still achieve a near constant efficiency of over 70% for a range of 0-70 cm.

The Wireless Identification and Sensing Platform (WISP) is a programmable, battery-free sensing and computational platform designed to explore sensor-enhanced radio frequency Identification (RFID) applications. It uses a 16-bit, ultra-low power microcontroller to perform sensing and computation while exclusively operating from harvested RF energy. A standard set of sensors that are typically installed on the WISP include: temperature, ambient light, rectified voltage, and acceleration. Since the WISP is a reconfigurable, PCB based RFID tag, new and innovative applications can be easily investigated. I present a method for increasing the range and read rate of RFID tags as well as proposing a novel sensing method that will enhance the functionality of passive tags.

The last topic that I will focus on is the Wireless Ambient Radio Power (WARP) project. This work has many similarities to the WISP and wireless sensor nodes, but the transmitters that wirelessly power WARP devices were never intended to be sources of far-field wireless power. Consider that radio frequency signals provide a near ubiquitous energy source, due to the large number of TV, radio, cellular, and WiFi transmitters distributed throughout our urban environments. While the traditional use of RF energy is information transmission, it is possible to harvest, convert, and store this energy using dedicated devices. I present work showing the feasibility of harvesting this power to do temperature sensing tasks, and I

have developed a full featured sensor node capable of sensing the environment; performing computation, and communicating wirelessly with a base station, all while being powered off of harvested RF energy.

1.3 Dissertation Organization

This dissertation is organized as follows: Chapter 2 provides background information on wireless power systems, by briefly highlighting notable historical research efforts in the field of wireless power. Section 2.1 presents a detailed overview of the tradeoffs between different wireless power methods and describes typical usage models for each method. Next, section 2.2 addresses health and safety concerns for wireless power systems and outlines the current regulatory landscape. In particular, it identifies that Specific Absorption Rate (SAR) is the key metric that should be used for determining the safety limits for RF magnetically coupled resonator systems. Additionally, section 2.3 provides a case study that describes how the range at which a device (such as an RFID tag) can be wirelessly powered, using far-field techniques, has doubled every four years due to Moore's Law and advances in the semiconductor industry.

Chapter 3 describes my work on the Wireless Resonant Energy Link project. In this section I present a new analysis that yields critical insight into the design of practical systems and presents a method of adaptive tuning that compensates for variations in transmitter to receiver orientation and distance. The next three chapters present research I have done related to the Wireless Identification and Sensing Platform. Chapter 4, is a detailed discussion of the design and characterization of the WISP. Chapter 5 presents a novel, photovoltaic enhanced UHF RFID tag antenna for dual purpose energy harvesting. Chapter 6 presents an antenna design for a capacitive touch interface for passive RFID tags. In chapter 7, I describe the research I have done on harvesting TV signals as a source of energy to power sensor nodes capable of transmitting data back to a base station. Finally, this dissertation is concluded in chapter 8 where I provide a summary of the work presented and outline future research topics.

Chapter 2

BACKGROUND

Interest in wireless power is certainly not new and significant research efforts have gone into exploring this field. A notable historical example is Nikola Tesla's work during the turn of the 19th century on electrostatic induction. His experimental apparatus is known as a Tesla coil, which capacitively couples high intensity electric fields between two points [60]. Later in his career, Tesla demonstrated wireless power transmission using radio frequency waves and is credited with the invention of the radio [63].

In the 1960s, William C. Brown pioneered the field of microwave power transmission using rectennas (or rectifying antennas) [3]. Demonstrations using high gain transmitters and rectennas for receiving and rectifying have shown wireless power transfer of 30 kW over a distance of one mile, with total end-to-end efficiency of 84% [39]. Today NASA, along with several Universities around the world, are continuing Brown's work in the effort to beam solar energy, collected in space, down to the earth.

In 2007, Kurs et al [36] demonstrated resonant, non-radiative or evanescent wave wireless power transfer. This work shows impressive efficiencies at short to moderate ranges with the potential to safely transfer 10s of watts of power. However, significant work needs to be done before this method of delivering wireless power can become a general purpose solution.

Confounding the concept of wireless power is overuse of the phrase to include any method of transferring energy without a wired connection. For instance, the WildCharge Pad from Pure Energy Solutions, Inc. uses ohmic conduction (i.e. physical contact), but doesn't have a physical wire. Other transfer methods that have been given the confusing label "wireless power" in literature include acoustic and mechanical vibration and thermal conduction. For the purpose of this report, wireless power will refer to quasi-static or dynamic electromagnetic energy transfer.

2.1 Modern Wireless Power Systems

Presently, several wireless power techniques are being pursued. It is useful to categorize these efforts in terms of their underlying power transfer mechanism to understand the implications for maximum range, efficiency, and mobility. Additionally, the tradeoffs between the absolute magnitude of the power transfer versus safety concerns will be discussed.

Far-field techniques use propagating electromagnetic waves that transfer energy the same way radios transmit signals. This method has been successfully used to power UHF RFID tags, which have no batteries and an operating range of ~ 10 meters [1, 54]. One of the drawbacks to far-field approaches is the inherent tradeoff between directionality and transmission efficiency. There are many examples of RF and microwave systems that use high gain antennas to transfer power over kilometer distances at efficiencies of over 90% [3, 39]. These systems suffer from the need for sophisticated tracking and alignment equipment to maintain a line of sight (point to point) connection in unstructured and dynamic environments.

Alternatively, RF broadcast methods, which transmit power in an omni-directional pattern, allow for power transfer anywhere in the coverage area. In this case, mobility is maintained, but end to end efficiency is lost since power density decreases with a $1/r^2$ dependence. This results in received power levels many orders of magnitude less than what was transmitted [52].

Inductive coupling (or near-field) techniques do not rely on propagating electromagnetic waves. Instead, they operate at a distance that is less than a wavelength of the signal being transmitted. Applications include rechargeable toothbrushes and the recent proliferating “power” surfaces [24]. These techniques can be very efficient, but are limited to transmission distances of about a centimeter. Alternatively, near-field RFID pushes the limit on distance by sacrificing efficiency. Near-field tags have a range of tens of centimeters, but only receive power in the microwatt range with 1 – 2% transmission efficiency [1].

Previously demonstrated magnetically coupled resonators used for wireless power transfer [5, 6, 32, 34, 37, 38, 68] have shown the potential to deliver power with more efficiency than far-field approaches and at longer ranges than traditional inductively coupled schemes.

However, this prior work is limited to a fixed distance and orientation, with efficiency falling off rapidly when the receiver is moved away from its optimal operating point.

Finally, laser based wireless power systems have shown promising results. In this case, the light beams are still propagating electromagnetic waves. However, the conversion method to DC relies on the quantum nature of light rather than its electromagnetic properties. Additionally, laser based systems are inherently point to point transfer methods and still suffer from the need for sophisticated tracking and alignment equipment to maintain the line of sight connection [8]. It is worth while to note that for typical solar cells and solar energy harvesting applications there is not a dedicated or man-made transmitter. This suggests the possibility of harvesting other sources of lower frequency electromagnetic energy that are not used for the purpose of wireless power.

All of the aforementioned techniques use different underlining energy transfer mechanisms and have vastly different usage models and trade offs. However, none of the wireless power solutions that exist today truly meet the vision of a useful general purpose wireless power system. First and foremost a wireless power system should be safe for use by the general public in uncontrolled environments. Second, it should have a range beyond a few millimeters, and should allow for device mobility in terms of orientation and range in uncontrolled environments. Third, a wireless power delivery system should provide enough power to the end device so that it can do useful work.

Finally, it is not sufficient to simply develop a mechanism to transfer energy wirelessly. It is necessary to consider the implications to the entire system, particularly the receive device. Significant research efforts need to be done to address the following issues: maintaining high RF to DC rectification efficiency as the source impedance (antenna output) and load resistance (application) varying. Second, power management algorithm and circuit blocks need to be developed that can handle variable and intermittent power from a wireless power transfer mechanism. The rectification and/or conversion of RF to DC power has significant impacts on the performance of the system especially when the antennas output impedance is variable and when the load power is variable.

2.2 Electromagnetic Safety for Wireless Power Systems

Recently, the use of coupled magnetic resonators has demonstrated the ability to achieve relatively high power transfer efficiency over relatively long distances [32,36]. Such methods offer the potential to deliver power in configurations not confined to close contact between the transmitter and receiver. A wide variety of human exposure conditions may be presented, depending on usage model and antenna geometry.

It is advantageous to operate wireless power systems based on coupled magnetic resonance in the low MHz range (approximately 1-20 MHz). For lower frequencies, it is difficult to achieve high-Q coils with dimensions appropriate for mobile devices. The shorter wavelengths of higher frequencies limit the spatial extent of the near-field coupling interaction. It may be particularly desirable to operate within bands designated internationally for Industrial, Scientific, and Medical purposes (e.g. 13.56 MHz).

From an RF safety perspective, it is important to identify the conditions under which potential product embodiments may demonstrate compliance with international safety guidelines. Very little work on exposure to wireless power systems is available in the current literature. Yuan *et al.* evaluated the influence of nearby persons on the transmission efficiency of a wireless power system using simplified models, but human exposure was not evaluated [67].

Further, the understanding of appropriate evaluation metrics continues to be the source of much confusion. Some have attempted to assess compliance based on incident fields [57]. However, for near-field exposure scenarios, incident field assessment significantly overestimates human exposure [31,44] and cannot be used for accurate compliance evaluation. For near field systems, compliance should be evaluated in terms of Specific Absorption Rate (SAR), in W/kg.

At the international level, safety guidelines for EM exposure of workers/general public and controlled/uncontrolled environments have been issued by the International Commission on Non-Ionizing Radiation Protection (ICNIRP Guidelines, 1998 [23]) and the Institute of Electrical and Electronics Engineers (IEEE C95.1-1999 [25] and IEEE C95.1-2005 [27]). The ICNIRP Guidelines form the basis for national regulations in several countries such as

the countries of the EU. The legally enforced values in the USA are based on a mixture of the NCRP(National Council on Radiation Protection and Measurements) 1986 [45] and IEEE 1992 [26] guidelines.

Between 100 kHz and 10 GHz, ICNIRP provides basic restrictions for electromagnetic fields in terms of the Specific Absorption Rate (SAR) in the body in order to prevent whole-body heat stress and excessive localized tissue heating. For the general public, a whole-body averaged SAR limit of 0.08 W/kg and a localized SAR limit of 2 W/kg in the head and trunk (averaged over 10 grams of tissue) are provided. In the latest version of IEEE C95.1, these same SAR limits are applied for the general public between 100 kHz and 6 GHz [27]. The SAR limit for the extremities (and for the pinnae in IEEE C95.1-2005) is 4 W/kg averaged over 10 grams of tissue, although the IEEE and ICNIRP standards have different definitions of extremities. Additionally, IEEE C95.1-1999 [25], IEEE C95.1-1992 [26] and US regulations define a limit of 1.6 W/kg averaged over any 1 gram of tissue.

The frequency range of interest for wireless power transmission is in a transition region where a second basic restriction is also provided to prevent electrostimulation of muscle and nerve tissues. ICNIRP provides a basic restriction on current density in mA/m² for frequencies between 1 Hz and 10 MHz, and IEEE C95.1-2005 provides a basic restriction on induced electric field between 3 kHz and 5 MHz. These basic restrictions are more limiting for pulsed fields having low duty cycles, whereas SAR limits are more limiting for continuous wave exposure [27]. SAR limits will be applied in this paper as they are more relevant for the system investigated.

Both standards have also derived reference levels for worst-case incident electric field strength (V/m) and magnetic field strength (A/m and μ T). Reference levels are derived from the basic restrictions based on uniform plane wave and whole body exposure with the most effectively coupling polarization. The reason for deriving reference levels is that the incident fields are often much easier to measure than SAR or induced fields. However, in the strongly nonuniform and reactive near field region, the incident fields are poorly correlated to the basic restrictions, and they significantly overestimate the real exposure [44]. Evaluations of near-field communication (NFC) systems [7] and contactless smartcard readers [31] have demonstrated this for systems operating in the low MHz.

2.3 Friis Path Loss and Moore's Law

As part of the larger discussion on wireless power, it is important to identify key, game changing factors, which were not applicable to wireless power pioneers such as Tesla and Brown. First and foremost, the innovation in integrated circuit manufacturing over the last few decades has dramatically decreased the amount of power consumed by electronic devices. Secondly, advancements in our understanding of the effects of radio waves on the human body have set safety limits on the amount of power that can be legally transmitted from an antenna. The result is that, although the amount of power that can be transmitted in the far-field will not increase, the amount of power required for a particular computational load has decreased, and will continue to do so over time. The following case study outlines the implication for range scaling as a function of advances in the semiconductor industry. This particular example focuses on far-field based wireless power transfer techniques applicable to UHF RFID systems.

There are regulatory limitations on the amount of RF power that can be transmitted for health and safety reasons, as well as to limit interference with other devices using the same spectrum. For instance, in the United States the Federal Communication Commission (FCC) limits the power transmitted in the Industrial, Scientific, and Medical (ISM) radio band (902 MHz - 928 MHz) to 4W (EIRP) [18]. Effective Isotropic Radiation Power (EIRP), also known as Equivalent Isotropic Radiation Power, refers to the peak power density that a theoretical isotropic antenna (which distributes power evenly in all directions) would produce for a given input power. Basically, the FCC limits the amount of power per unit volume to insure safety.

The second factor that defines the range at which a load can be wirelessly powered is the fundamental propagation of the electromagnetic wave through space. In an ideal case, the power radiating from an isotropic source travels in a uniform sphere that grows in size as the wave travels away from the source. Since the surface area of the sphere increases with distance, the power density at any one location (i.e. fix surface area) on the sphere will decrease with distance. This phenomenon is described in the Friis transmission equation (2.1), also referred to as the Friis path loss equation.

$$P_R = P_T G_T G_R \left(\frac{\lambda}{4\pi r} \right)^2 \quad (2.1)$$

The power received is denoted as P_R ; power transmitted is P_T , transmit and receive antenna gains are G_T and G_R , λ is wavelength, and r is range from transmit to receive antenna. We can rewrite this to solve for range as a function of the other parameters (2.2).

$$r = \left(\frac{P_T G_T G_R}{P_R} \right)^{1/2} \left(\frac{\lambda}{4\pi} \right) \quad (2.2)$$

If we interpret P_R as the power required to execute a certain workload, then it is straightforward to turn this expression into a range feasibility condition, setting P_R to be the minimum power necessary to execute a fixed workload and r is then the maximum range at which that workload can be wirelessly powered.

Transistor scaling, predicted by Moore's law, is driving down the minimum power requirements to perform a fixed computational workload (a fixed number of instructions per second) because with each technology generation the minimum achievable energy per instruction drops.

Figure 2.1 presents historical and extrapolated microprocessor efficiency scaling alongside range scaling. The upper line, microprocessor efficiency, is in units of instructions per μJ . (These units were chosen because they turn out to yield the same numerical scale as meters.) The microprocessor efficiency data was derived from historical data sheets. An exponential fit of the data yields the following expression (2.3) for the efficiency scaling.

$$\text{Moore's Law : } \frac{\text{Instruction/sec}}{P_R} \propto 2^{0.46t} \quad (2.3)$$

Next, the Friis transmission equation (2.1) is used to extrapolate the range at which a fixed work load can be powered (bottom line), given constant transmit power, frequency, and antenna gains. An exponential fit of this line yields the range scaling expression in equations (2.4).

$$\text{Friis}(Moore(t)) : \text{Distance} \propto 2^{0.23t} \quad (2.4)$$

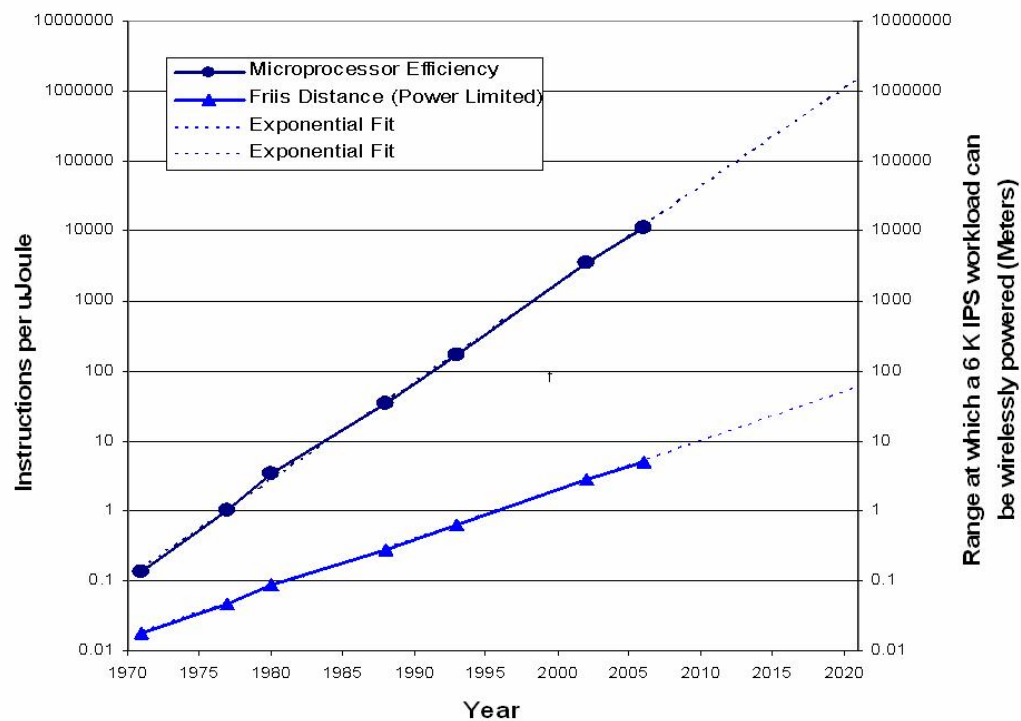


Figure 2.1: Range scaling of radiative wirelessly powered devices. Upper line (left scale): microprocessor efficiency, measured in instructions per μ J. The doubling time is approximately 2 years. Lower line (right scale): range in meters at which sufficient power can be delivered wirelessly to run a workload of 60k instructions per second. Range doubling time is approximately 4 years for a constant computational load.

Thus, the doubling time for microprocessor efficiency is about 2 years, while the doubling time for the range (at which a fixed work load can be powered) is about 4 years. From this, we can see that Moore's law is a key enabler of usable wireless power systems. For example, if scaling continues at the same rate until 2020, we would expect that sufficient power for the 60k IPS workload (approximately the work load of a WISP) would be available at a range of greater than 40m.

It is important to note that the Friis-Moore range scaling argument will most likely not hold true for RFID tags or other ultra-low power systems in the future, due to some fundamental limitations of CMOS technology. The problem is that the efficiency at which RF power can be rectified into DC power will not hold constant with time (i.e. process nodes). Since constant electric field scaling, which has driven the semiconductor market for the last 30 years, is no longer viable in deep sub-micron technology, the threshold voltages for transistors are no longer decreasing.

This means that even though the amount of harvested power needed from the antenna is decreasing (since the required power for an application is decreasing), there will not be sufficient voltage to meet the voltage threshold of the diode connected transistors, assuming a fixed line impedance (i.e. voltage to current ratio). As a result, it becomes increasingly harder to both effectively impedance match and maintain rectifier efficiency. Thus, even though the instructions per μJ will most likely continue to increase with time as predicted, energy conversion will be a limiting factor for RFID. This issue is not a factor for high power applications, where there is typically sufficient voltage to activate the rectifier diodes/transistors.

Chapter 3

WIRELESS RESONANT ENERGY LINK

Advances in wireless communication and semiconductor technology have enabled a wide variety of portable consumer electronic, medical, and industrial devices. However, users are still required to manually plug in these mobile devices, limiting ultimate mobility and disrupting use when charge is depleted. Furthermore, as portable devices shrink, connectors become a larger fraction of system size. Wireless power offers the possibility of connector-free electronic devices, which could improve both size and reliability. Thus, there is the desire to use wireless power technology to eliminate the remaining wired power connection.

Previously demonstrated magnetically coupled resonators used for wireless power transfer [5, 6, 32, 34, 37, 38, 68] have shown the potential to deliver power with more efficiency than far-field approaches, and at longer ranges than traditional inductively coupled schemes. However, this prior work is limited to a fixed distance and orientation, with efficiency falling off rapidly when the receiver is moved away from its optimal operating point.

In my work presented here [53] we extend prior analysis of coupled magnetic resonance to elucidate several key system concepts including: frequency splitting, critical coupling, and impedance matching. We present a model of magnetically coupled resonators in terms of passive circuit elements and derive system optimization parameters. Additionally, a method for automatically tuning the wireless power system is demonstrated so that the maximum possible transfer efficiency is obtained for nearly any distance and/or orientation as long as the receiver is within the working range of the transmitter. This is important from a practical standpoint because in many applications, such as laptop recharging, the range and orientation of the receive device with respect to the transmit device varies with user behavior [65].

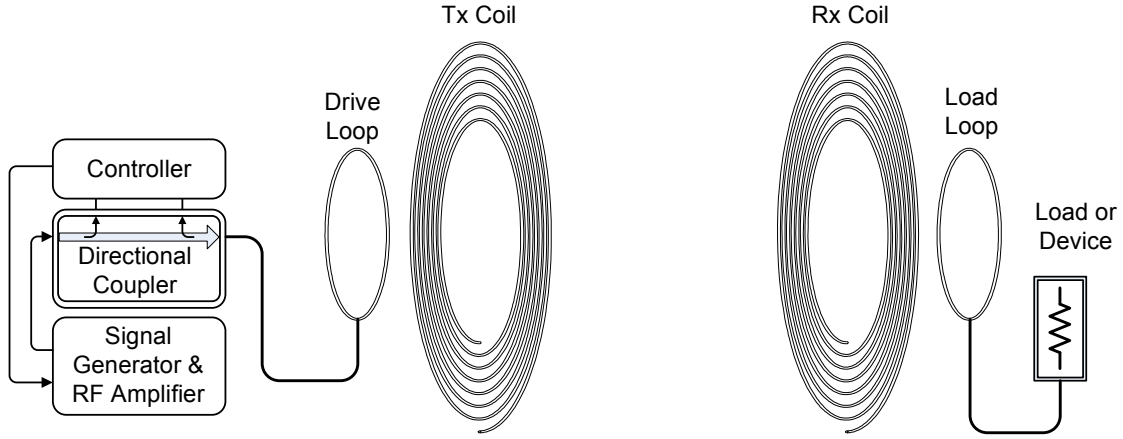


Figure 3.1: Sketch of the magnetically coupled resonant wireless power system consisting of an RF amplifier, on the left, capable of measuring the forward and reflected power. A two element transmitter, made of a signal turn drive loop and high Q coil, wirelessly powers the receiver on the right.

3.1 System Overview

Figure 3.1 shows a diagram of a wireless power system using magnetically coupled resonators. The transmit antenna consists of a single turn drive loop and a multi-turn spiral coil. When the RF amplifier powers the drive loop the resulting oscillating magnetic field excites the Tx coil which stores energy in the same manner as a discrete LC tank. Another way to think about this two element transmitter is as a *tuned* step-up transformer, where the source is connected to the primary (the Tx loop) and the secondary (the Tx coil) is left open. The receive side functions in a similar manner, although a load replaces the power source and the system functions as a step-down transformer from the viewpoint of the receive coil.

The key interaction occurs between the two coils each of which is a high-Q LCR tank resonator. Just as the loop and coil are magnetically coupled, the transmit and receive coils share a mutual inductance which is a function of the geometry of the coils and the distance between them. In order to gain an intuitive understanding of how magnetically coupled resonators can efficiently transfer energy back and forth, it is useful to recall the properties of coupled oscillating systems.

Consider the case of two pendulums connected by a spring, which is analogous to magnetically coupled LCR tanks [20]. In this classic physics example, the two pendulums will form a single system which can oscillate in two modes: one of higher and one of lower frequency than the fundamental frequency of an individual pendulum. Furthermore, the frequency separation of the two modes is dependent on the stiffness (or coupling) of the spring. As this stiffness decreases, the degree of frequency separation (referred to as frequency splitting) also decreases until the two modes converge to the fundamental frequency of a single pendulum. This indicates that when driving coupled resonators, there can be more than one mode or tuned frequency. This also means that the resonant frequency of the system will change as a function of the coupling, and in the case of the wireless power system, coupling is dependent on the distance between the transmit and receive coils.

Another significant property of coupled oscillators is that the amount of coupling defines the rate of energy transfer, not its efficiency [20]. For the coupled pendulums the spring constant defines how much energy is transferred from one mass to the other per cycle. The stiffer the spring, the more energy is imparted per cycle; efficiency, on the other hand, is determined entirely by energy losses, due to friction in a pendulum or equivalently parasitic resistance in the coils. To the extent that these losses can be neglected, energy not transferred to the receive coil remains in the transmit coil. Thus, even if the coupling is very small (limiting the rate of energy transfer), the efficiency can still be very high, for coils that are high in Q . This is a somewhat counterintuitive result for wireless power systems, especially when compared to the case of omni directional far-field antennas which show a $1/r^2$ dependence for efficiency, and inductive coupling which has a $1/r^3$ dependence.

Finally, the mechanisms for driving and extracting work from coupled resonant systems add additional constraints. To highlight this, the pendulum example can be modified by attaching a dashpot to extract work from one of the masses while sinusoidally driving the other pendulum at one of the system's resonant frequencies. If the amount of power transferred through the spring each cycle is not enough to provide power to the load of the dashpot, the magnitude of the pendulum oscillation will begin to decay. In order to avoid this situation, the stiffness of the spring can be increased so that it imparts more energy per cycle, bringing the system back into equilibrium. This means that for every load there

is a minimum amount of coupling that is necessary to maintain the system at equilibrium. Equivalently, when driving the wireless power system with an RF source and using a load resistor on the receiver to extract work from the system, the amount of coupling defines how much energy is transferred per cycle. This means that there is a distance (called the critical coupling point) beyond which the system can no longer drive a given load at maximum efficiency.

The following sections will build upon the concepts of frequency splitting, critical coupling, and damping/impedance matching. First, an analytic model of the magnetically coupled resonator system is presented in section 3.2. This is followed by derivations of key system parameters and figures of merit in section 3.3. Section 3.4 compares our model and theoretical predictions of system performance to measured results. Finally, section 3.6 describes adaptive tuning techniques used to achieve near constant efficiency vs. distance while the receiver is within range of the transmitter.

3.2 Circuit Model and Transfer Function

The magnetically coupled resonator system can be represented in terms of lumped circuit elements (L , C , and R). Figure 3.2 shows a straightforward circuit diagram that can be used for hand analysis or for SPICE simulations.

The schematic consists of four resonant circuits, linked magnetically by coupling coefficients k_{12} , k_{23} , k_{34} . Starting from the left, the drive loop is excited by a source with finite output impedance, R_{source} . A simple one-turn drive loop can be modeled as an inductor (L_1) with parasitic resistance, R_{p1} . A capacitor (C_1) is added to make the drive loop resonant at the frequency of interest. The transmit coil consists of a multi-turn air core spiral inductor (L_2), with parasitic resistance (R_{p2}). The geometry of the Tx coil determines its self-capacitance which is represented as C_2 . Inductors L_1 and L_2 are connected with coupling coefficient k_{12} ; the receive side is defined similarly. Finally, the transmitter and receiver coils are linked by coupling coefficient, k_{23} . A typical implementation of the system would have the drive loop and Tx coil built into a single device such that k_{12} would be fixed. Similarly, k_{34} would also be fixed. Thus k_{23} is the remaining uncontrolled value which varies as a function of the distances between the transmitter to receiver.

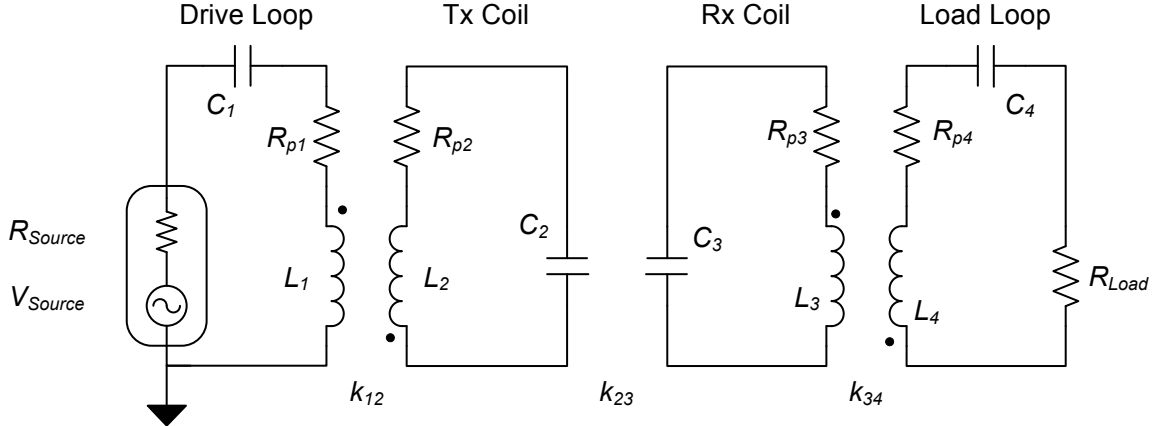


Figure 3.2: Equivalent circuit model of the wireless power system. Each of the four antenna elements are modeled as series resonators, which are linked by mutual inductances via coupling coefficients.

This circuit model provides a convenient reference for analysis of the transfer characteristics of a magnetically coupled resonator system. For the sake of simplicity the cross coupling terms (k_{13} , k_{24} , k_{14}) are neglected in the following analysis. The simplified model where Kirchhoff's voltage law can be applied to determine the currents in each resonant circuit in equation (3.1), where the coupling coefficient is defined in equation (3.2).

$$\begin{aligned}
 I_1 \left(R_{Source} + R_{p1} + j\omega L_1 + \frac{1}{j\omega C_1} \right) + j\omega I_2 M_{12} &= V_S \\
 I_2 \left(R_{p2} + j\omega L_2 + \frac{1}{j\omega C_2} \right) + j\omega (I_1 M_{12} - I_3 M_{23}) &= 0 \\
 I_3 \left(R_{p3} + j\omega L_3 + \frac{1}{j\omega C_3} \right) + j\omega (I_4 M_{34} - I_2 M_{23}) &= 0 \\
 I_4 \left(R_{Load} + R_{P4} + j\omega L_4 + \frac{1}{j\omega C_4} \right) + j\omega I_3 M_{34} &= 0
 \end{aligned} \tag{3.1}$$

$$k_{xy} = \frac{M_{xy}}{\sqrt{L_x L_y}}, \quad 0 \leq k_{xy} \leq 1 \tag{3.2}$$

These four KVL equations are simultaneously solved for the voltage across the load resistor and yield equation (3.3), with the substitution in equation (3.4).

$$\frac{V_{Load}}{V_{Source}} = \frac{i\omega^3 k_{12} k_{23} k_{34} L_2 L_3 \sqrt{L_1 L_4} R_{load}}{\left(k_{12}^2 k_{34}^2 L_1 L_2 L_3 L_4 \omega^4 + Z_1 Z_2 Z_3 Z_4 \right) + \omega^2 \left(k_{12}^2 L_1 L_2 Z_3 Z_4 + k_{23}^2 L_2 L_3 Z_1 Z_4 + k_{34}^2 L_3 L_4 Z_1 Z_2 \right)} \quad (3.3)$$

$$\begin{aligned} Z_1 &= R_{p1} + R_{Source} + j\omega L_1 - j/(\omega C_1) \\ Z_2 &= R_{p2} + j\omega L_2 - j/(\omega C_2) \\ Z_3 &= R_{p3} + j\omega L_3 - j/(\omega C_3) \\ Z_4 &= R_{p4} + R_{Load} + j\omega L_4 - j/(\omega C_4) \end{aligned} \quad (3.4)$$

The system transfer function (3.3) is plotted in figure 3.3 for the circuit values shown in Table I. This plot shows S_{21} magnitude as a function of frequency and coupling coefficient k_{23} . For consistency, power transfer will be represented in terms of linear magnitude scattering parameters ($|S_{21}|$), which is important experimentally since it can be measured with a vector network analyzer for later comparison. The entire wireless power transfer apparatus can be viewed as a two-port network (one port being the input, fed by the source, and the other the output, feeding the load). Using equation (3.3) one can calculate the equivalent S_{21} scattering parameter using [11, 43] which results in equation (3.5).

$$S_{21} = 2 \frac{V_{Load}}{V_{Source}} \left(\frac{R_{Source}}{R_{Load}} \right)^{1/2} \quad (3.5)$$

In figure 3.3, frequency splitting is clearly visible as the value of k_{23} is increased. A SPICE simulation reveals that indeed the lower frequency mode of the two coils is in phase, while the higher frequency mode is 180° out of phase. As the coupling between the coils decreases, the frequency separation also decreases until the two modes converge at f_o . This point is called the critical coupling point and represents the farthest distance at which maximum power efficiency is still achievable (since k_{23} is proportional to $1/distance^3$). When k_{23} is greater than $k_{critical}$, the system is said to be overcoupled and operating at either resonance will result in maximum power transfer efficiency. Conversely, when k_{23} is less than $k_{critical}$, the system is undercoupled and the amount of power delivered to the

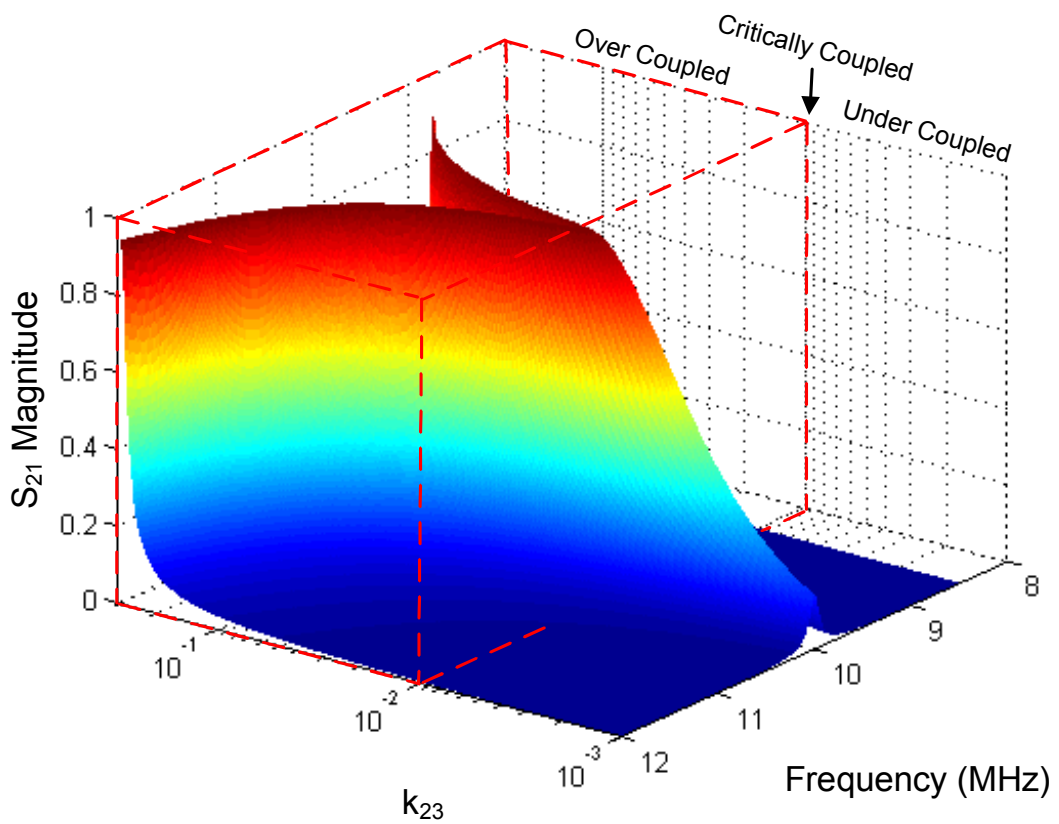


Figure 3.3: S_{21} magnitude as a function of frequency and transmitter to receiver coupling k_{23} for the simplified circuit model given the values in table I. The highlighted red volume is the over coupled regime, where frequency splitting occurs and transfer efficiency can be maintained independent of distance if the correct frequency is chosen.

Table 3.1: Circuit Values Used to Evaluate the Simplified Model

PARAMETER	VALUE
$R_{\text{source}}, R_{\text{Load}}$	50Ω
L_1, L_4	$1.0 \mu\text{H}$
C_1, C_4	235 pF
R_{p1}, R_{p4}	0.25Ω
K_{12}, K_{34}	0.10
L_2, L_3	$20.0 \mu\text{H}$
C_2, C_3	12.6 pF
R_{p2}, R_{p3}	1.0Ω
k_{23}	0.0001 to 0.30
f_0	10 MHz
Frequency	8 MHz to 12 MHz

load begins to fall off precipitously with distance. The red dashed box outlined in figure 3.3 encloses the ‘magic regime’ where near-constant efficiency vs. distance can be achieved if the correct frequency is selected. This is dramatically different from typical far-field or near-field systems where efficiency drops off rapidly with distance. An adaptive frequency tuning method, used to insure that the maximum possible transfer efficiency is achieved at any distance within the ‘magic regime’ is described in Section 3.6.1.

3.3 Derivations of critical coupling and system parameters

Further analysis of the transfer function (3.3) allows insight into which circuit parameters can be used to optimize the performance of the wireless power system. First, the equation of critical coupling will be derived by substituting the term for series quality factor and resonant frequency, shown in equation (3.6), into the transfer function (3.3).

$$Q_i = \frac{1}{R_i} \sqrt{\frac{L_i}{C_i}} = \frac{\omega_i L_i}{R_i} = \frac{1}{\omega_i R_i C_i}, \quad \omega_i = \frac{1}{\sqrt{L_i C_i}} \quad (3.6)$$

$$\left(\frac{V_{\text{Load}}}{V_{\text{Source}}} \right) |_{\omega=\omega_0} = \frac{i k_{cc} k_{lc}^2 Q_{coil}^2 Q_{loop}^2}{k_{cc}^2 Q_{coil}^2 + (1 + k_{lc}^2 Q_{coil} Q_{loop})^2} \quad (3.7)$$

Here the “ i_{th} ” subscript denotes the circuit elements in figure 3.2 for example, $i = 1$ denotes the elements in the drive loop (L_1, C_1, R_{p1}). It should be noted that the expression for ω_i represents the free resonant frequency of each loop and coil, which does not include the damping factor attributed to the resistance in the LCR tank. This approximation has a negligible effect on ω_i and only accounts for a deviation of $\pm 0.25\%$ in the final transfer function. For simplicity, the system is defined to be symmetrical, with the quality factor of the Tx and Rx coils equal, $Q_{coil} = Q_2 = Q_3$, and the quality factors of the Tx and Rx loops equal, $Q_{loop} = Q_1 = Q_4$. The symmetric loop-to-coil coupling, $k_{12} = k_{34}$, will be denoted k_{lc} . We will also assume $R_{source} = R_{load}$, $R_{p1} \ll R_{source}$, $R_{p4} \ll R_{load}$, and that the uncoupled resonant frequency of each element is defined to be ω_0 . To maintain consistency, the notation for the symmetric case, coil to coil coupling (k_{23}) will be renamed k_{cc} . Finally, for the sake of brevity, only the derivation for the voltage gain at the center frequency ω_0 is presented in equation (3.7). This function represents a 2D slice of figure 3.3 along the center frequency of 10 MHz, whose apex is the critical coupling point of the system. Furthermore, equation (3.7) is equivalent to voltage gain in equation (3.3) for $\omega = \omega_0$.

In order to find the function that predicts critical coupling point $k_{critical}$, the derivative of (3.7) is taken with respect to k_{cc} . Setting the result to zero and solving for k_{cc} yields equation (3.8), where all variables are defined to be positive.

$$k_{critical} = \frac{1}{Q_{coil}} + k_{lc}^2 Q_{loop} \quad (3.8)$$

Here $k_{critical}$ defines the extent of the ‘magic regime’ as shown in figure 3.3. In order to find magnitude at the critical coupling point, $k_{critical}$ is substituted back into k_{cc} in equation (3.7). The resulting equation represents the maximum efficiency achievable at the furthest possible operation point before the system becomes under-coupled. Using equation (3.5) and recalling that $R_{load} = R_{source}$, this voltage gain (V_{Load}/V_{Source}) at the critical coupling point can be converted into the scattering parameters, which will be denoted $|S_{21}|_{critical}$ in equation (3.9).

$$|S_{21}|_{critical} = \frac{k_{lc}^2 Q_{coil} Q_{loop}}{1 + k_{lc}^2 Q_{coil} Q_{loop}} = \frac{k_{lc}^2 Q_{loop}}{k_{critical}} \quad (3.9)$$

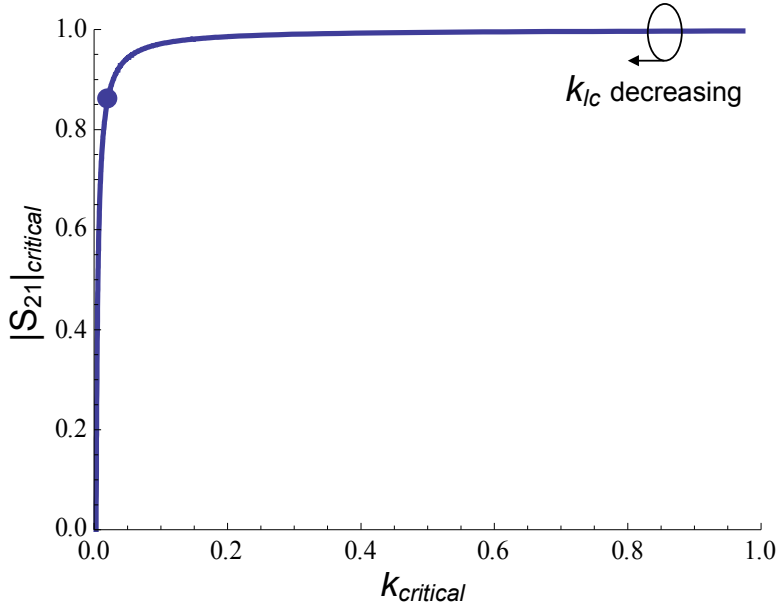


Figure 3.4: Efficiency vs. critical coupling range: $|S_{21}|_{critical}$ vs. $k_{critical}$ trade off curve as a function of the tuning parameter k_{lc} , with our system's operating point indicated (large dot at $k_{lc}=0.135$).

Recall that in order to maximize range, we must minimize $k_{critical}$ because this increases the extent of the ‘magic regime’, which spans from $k_{critical}$ to 1.0. Examining equation (3.8) shows that reducing k_{lc} lowers $k_{critical}$ and therefore increases range. However, according to equation (3.9), reducing k_{lc} also reduces efficiency. Indeed, the choice of k_{lc} trades off the efficiency level in the ‘magic regime’ (height of the V-shaped ridge) vs. the extent of the ‘magic regime’ (spatial length of V-shaped ridge). Figure 3.4 is a plot of this trade off curve, $|S_{21}|_{critical}$ vs. $k_{critical}$, as a function of the common parameter k_{lc} .

The area under this trade off curve serves as a useful figure of merit (FOM) for system performance. An optimal wireless power system, which could losslessly deliver power at an infinite range (coupling $\rightarrow 0$) would have a FOM of unity. For the symmetrical case the FOM integral can be evaluated analytically. Assuming that $Q_{coil} > 1$, the area under the tradeoff curve is equation (3.10).

$$FOM = \int_0^1 |S_{21}|_{critical} dk_{critical} = 1 - \frac{1}{Q_{coil}} - \frac{\ln Q_{coil}}{Q_{coil}} \quad (3.10)$$

The FOM is only dependent on Q_{coil} and is independent of Q_{loop} . The quality factor of the resonators (coils) entirely determines this measure of system performance, which approaches unity in the limit of infinite Q_{coil} . The measured Q_{coil} values for our system are around 300 and 400, corresponding to $FOM = .978$ and $FOM = .982$. Choosing a feasible value of Q_{loop} is the next important design question. To derive a guideline, we will find an expression for the ‘knee’ of the range-efficiency tradeoff curve, which is defined as the point at which the slope equals unity in figure 3.4. Solving $d|S_{21}|_{critical}/dk_{critical} = 1$ for $k_{critical}$, we find:

$$k_{criticalknee} = Q_{coil}^{-1/2} \quad (3.11)$$

If Q_{loop} is too small, then even when setting k_{lc} to its maximum value of 1.0, $k_{critical}$ will not be able to reach $k_{criticalknee}$. To find the minimum necessary Q_{loop} value, we can solve equation (3.8) for Q_{loop} with $k_{critical} = k_{criticalknee}$ and $k_{lc} = 1$, which yields $Q_{loop} = (Q_{coil}^{1/2} - 1)Q_{coil}^{-1} \approx Q_{coil}^{-1/2}$ for large Q_{coil} . Specifically, a good operating point on the tradeoff curve should be achievable as long as $Q_{Loop} > Q_{coil}^{-1/2}$. For $Q_{coil} = 300$, this condition becomes $Q_{loop} > 0.06$. In our working system the loaded Q_{loop} values are around 0.9, about one order of magnitude larger than this limit.

The key conclusion is that Q_{Coil} determines system performance (as measured by our FOM), as long as a minimum threshold value of Q_{loop} is exceeded. The actual value of Q_{loop} (less than 1 for our system) is dominated by the source and load impedances. The larger Q_{Coil} is, the smaller the required minimum Q_{loop} . Conversely, moving to a more demanding load (with Q_{loop} below the current threshold value) can be accomplished by sufficiently increasing Q_{Coil} .

3.4 Parameter Extraction and Measurement Techniques

The model derived in section 3.2 provides a useful transfer function of the wireless power system. However, this circuit model is expressed in terms of R_i , L_i , and C_i and does not

reflect the physical geometry of the loops and coils. In order to compare the model to a real world system the values for inductance, capacitance, and resistance must be determined for each of the four resonant circuits. Additionally, the mutual inductance between the four resonant circuits is dependent on the radius and number of turns of the coils and loops as well as the distance between the elements.

One of the significant challenges when comparing the theoretical model to measured data is the accurate estimation of these free parameters. For example, published closed-form solutions for estimating the self capacitance of a helix or spiral resonators are only accurate to within 10-15% [15, 40]. Furthermore, when calculating the wire resistance, approximations can be made for both ohmic loss and high frequency skin depth, but the oxidation of the metal, mechanical surface conditions, and the quality of solder joints on the loops cannot easily be modeled. Since small inaccuracies in the calculations of these parameters will cause the quality factor of the resonators to vary significantly, we rely on empirically measured determined circuit parameter values.

In RF and microwave engineering resonant structures are often used as the building blocks for filters, oscillators, and impedance transformers. As a result a number of standard measurement techniques have been developed to extract parameters such as resonant frequency, coupling coefficient, and unloaded Q factor [29]. These techniques typically use a Vector Network Analyzer (VNA) to measure the scattering parameters of a Device Under Test (DUT) and then employ a computer to solve for the quantities of interest. Since a VNA can sample a large number of data points the problem space is over defined, allowing for a reliable fit with error estimation. These techniques have been adapted to measure circuit values for the drive and load loops, as well as for the transmit and receive coils.

Figure 3.5 shows the experimental setup used to validate the theoretical model. The transmitter on the left consists of a small drive loop centered within a flat spiral transmit resonator. The drive loop is 28 cm in diameter, with a series connected variable capacitor used to tune the system to 7.65 MHz. An SMA connector is also placed in series so that an RF amplifier can drive the system, as depicted in the circuit diagram in figure 3.2. The large transmit coil starts with an outer diameter of 59 cm and spirals inwards with a pitch of 1 cm for approximately 6 turns. The resonant frequency of \sim 7.65 MHz was



Figure 3.5: Photograph of the transmitter and receiver used in the wireless power system. For scale the outside diameter of the large coils is 59 cm.

determined experimentally and is not intended to correlate with the resonant frequency of the mathematical example in section 3.2. Since it is difficult to accurately predict the self capacitance of the coils, the resonant frequency is tuned by manually trimming the end of the spiral until each coil individually resonates at ~ 7.65 MHz. The receiver is constructed similarly. All elements are made of 2.54 mm diameter copper wire and is supported by Plexiglas armatures.

3.4.1 Parameter Extraction and Estimation

Section 3.4.1.1 and 3.4.1.2 describe the measurement techniques used to independently determine the lumped circuit values for each of the four resonant circuits. These values will be inserted back into the transfer function 3.3 for later comparison to measured data. Since the mutual inductance and thus coupling coefficient is not directly measurable, the algorithm presented in section 3.4.1.3 is used to calculate the coupling of each of the loops and coils at varying distances.

3.4.1.1 Extraction of Loop Parameters

First, a Vector Network Analyzer (VNA) is used to measure the scattering parameters of a Device Under Test (DUT) as a function of frequency. Next, an impedance model of the DUT is fitted to the complex S_{11} data using an unconstrained nonlinear optimization routine to solve for the free variables. Since a VNA can sample a large number of data points, the problem is over-constrained, allowing for a reliable fit with error estimation.

Figure (3.6) shows a circuit diagram of a single loop with input impedance Z_{in} as seen by the source. Equation 3.12 represents a mathematical model of the circuit model of the single loop. Equation 3.13 is the transform to used convert the impedance parameters (Z_{11}) to scattering parameters (S_{11}). In order to determine the capacitance, inductance, and parasitic resistance of the drive and load loops, each device is isolated from the rest of the system and a VNA is used to measure its S_{11} scattering parameters. This measurement consists of a 1601 point frequency sweep centered at 7.65 MHz with a span of 4 MHz and is shown in the right panel of figure (3.6).

Next the model in equation 3.13 and 3.12 is fitted to the S_{11} data using an unconstrained nonlinear optimization function for the free variables C , R_p , and L . The right side of figure (3.6) shows the raw data and fitted model for the drive loop. The coefficient of determination (R^2) is used to quantify the quality of the fit, where $0 \leq R^2 \leq 1$ with a value 1 indicating a perfect match between the fitted model and measurements. In this case the drive loop $R^2 = 0.9999$, and the lumped circuit values are reported in Table II.

$$Z_{in} = R_p + j\omega L + \frac{1}{j\omega C} \quad (3.12)$$

$$S_{11} = \frac{Z_{in} - 50}{Z_{in} + 50} \quad (3.13)$$

3.4.1.2 Extraction of Coil Parameters

The method for extracting the circuit parameters for the resonant coils is complicated by the fact that there is no direct way to connect the coils to the VNA. To work around this issue, the loops that were characterized in the previous section are used to magnetically

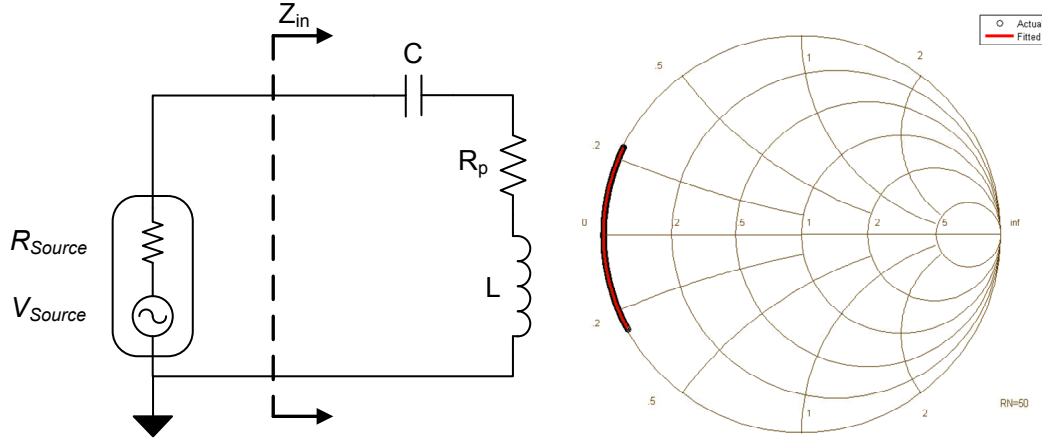


Figure 3.6: Circuit diagram of the drive loop (left) and measured and extracted S_{11} data (right).

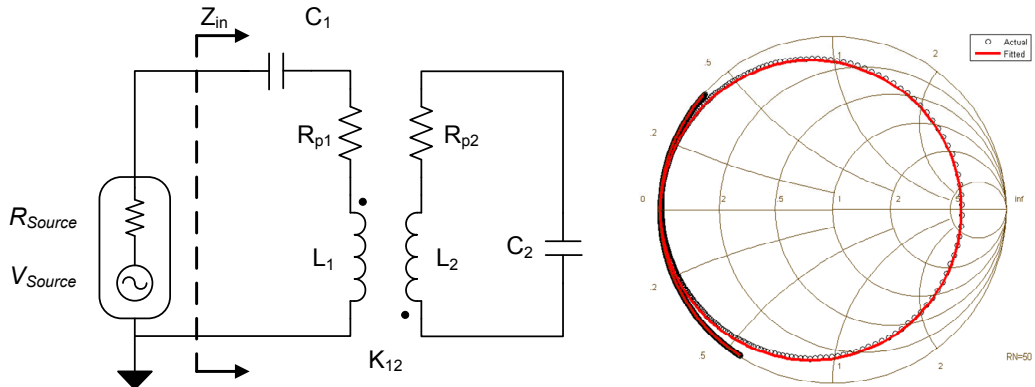


Figure 3.7: Circuit diagram of drive loop and transmit coil along with (left) and measured and extracted S_{11} data (right).

couple in to the coils, and the two body system is then measured and analyzed. The left panel of figure 3.7 shows a circuit diagram of the measurement setup.

The circuit is analyzed as an ideal transformer and Z_2 in equation 3.14 is a transformation of the impedance of the coil as seen from the primary side. In the derivation for input impedance the values of Z_2 always appears in a ratio with L_2 , so that the values of L_2 , C_2 , and R_{p2} cannot be directly disambiguated. Thus, equation 3.14 is written in terms of Q

factor, coupling coefficient, and resonant frequency of the coil. Next the fitting routine is used to find the free parameters Q , f_o , and k_{12} with the constants of the loop determined in the previous step. The right panel of figure 3.7 shows the measured S_{11} data for the drive loop and Tx coil and the resulting model fit. The extracted values lumped circuit are reported in Table II, and the R^2 value of the fit is 0.9999. Although not critical for characterizing the coils, the inductance will be estimated using Neumann's formula in the next section and R_p and C can be calculated from the extracted value of the unloaded Q and resonant frequency. However, the model validation could equally be done using the asymmetric Q form of the transfer function as described by equations 3.7.

$$Z' = \frac{Z_2}{L_2} = j\omega(1 + k^2) + \frac{\omega_o^2}{j\omega} + \frac{\omega_o}{Q_o} \quad (3.14)$$

$$Z_{in} = R_1 + \frac{1}{j\omega C_1} + \frac{j\omega L_1 Z'}{j\omega k^2 + Z'} \quad (3.15)$$

$$S_{11} = \frac{Z_{in} - 50}{Z_{in} + 50} \quad (3.16)$$

3.4.1.3 Calculation of Self and Mutual Inductance

The coupling coefficients that link the four resonant circuits are key parameters for predicting the behavior of the system. Since each coupling coefficient is dependent on the mutual-inductances between two elements and the self-inductances of each, it is necessary to calculate both these quantities for the spiral coil resonators.

In order to find the self-inductance of the coil resonators, the technique suggested in [10] is used to approximate a flat spiral as a series of concentric loops of wire. Figure 3.8 shows a conceptual diagram of the model, where each turn of the spiral is replaced with a loop, and the pitch of the spiral defines the spacing between each loop. Using Neumanns formula for concentric, axial rings [46] the equations for self-inductance and mutual-inductance are shown in equations 3.17 and 3.18, respectively.

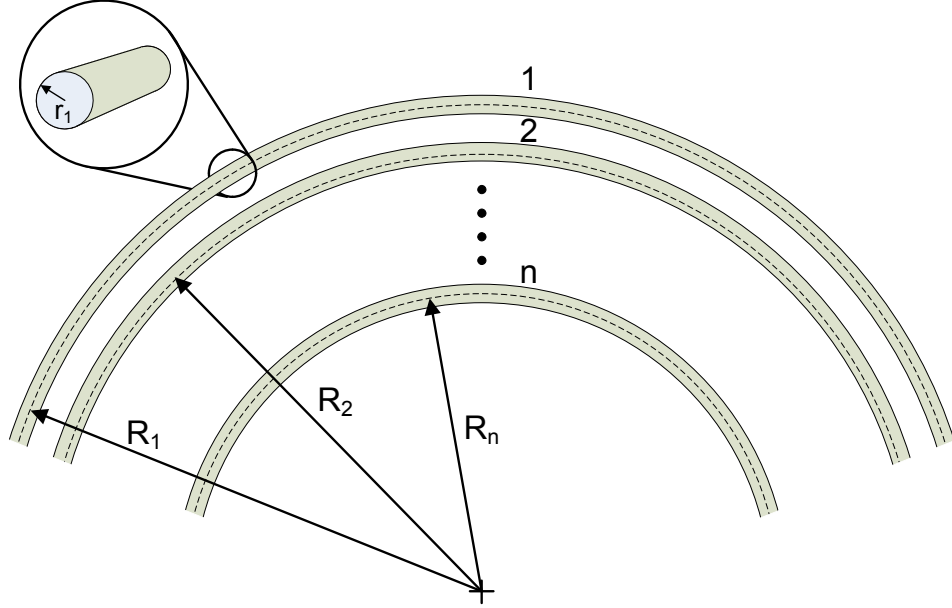


Figure 3.8: Concentric ring approximation for a spiral coil.

$$L_i = \frac{\mu_r \mu_o R_i}{4} + \mu_o R_{ii} (R_i - r_i) \int_0^\pi \frac{\cos(\phi) d\phi}{\sqrt{R_i^2 + (R_i - r_i)^2 - 2R_i(R_i - r_i) \cos(\phi)}} \quad (3.17)$$

$$M_{ij} = \mu R_i R_j \int_0^\pi \frac{\cos(\phi) d\phi}{\sqrt{R_i^2 + R_j^2 + z^2 - 2R_i R_j \cos(\phi)}} \quad (3.18)$$

Here, the radius of the ring is R_i and the wire radius is r_i . The parameters z in equation 3.18 represents the distance between two rings along the common axis, and is zero when calculating self inductance. Using equation 3.19 the total self inductance of the spiral coil (L_{spiral}) can be calculated by summing the inductance (L_i) contributed by each ring and the mutual inductance (M_{ij}) each ring experiences from its neighbors.

$$L_{spiral} = \sum_{i=1}^n L_i + \left(\sum_{i=1}^n \sum_{j=1}^n M_{ij} \right)_{\text{for } i \neq j} \quad (3.19)$$

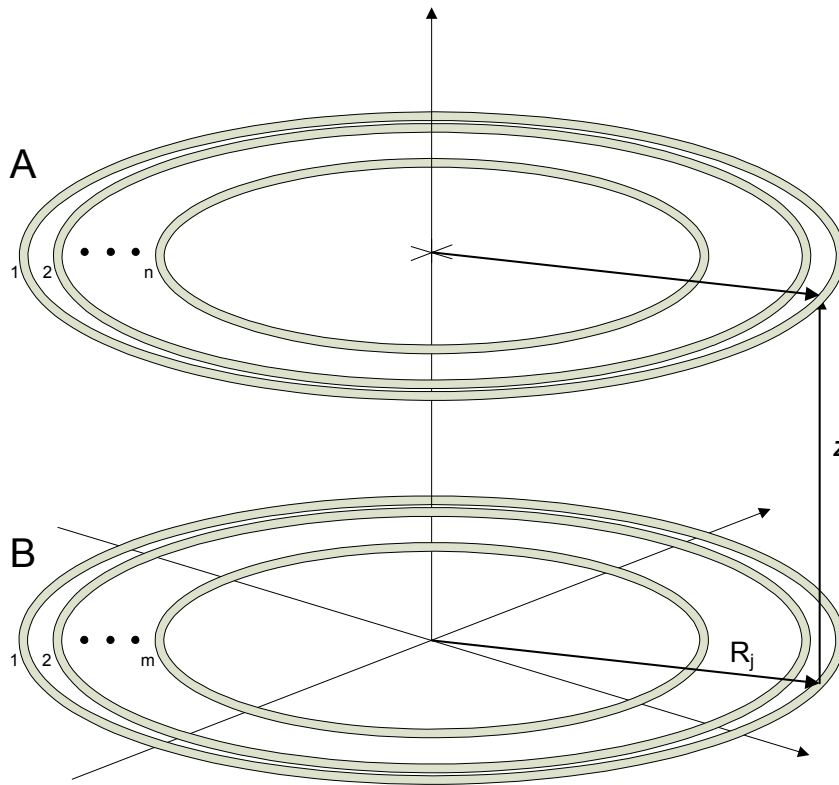


Figure 3.9: Approximation for calculating the mutual inductance of two coaxial spiral coils.

In order to find the mutual inductance between two coils or between a loop and a coil, the concentric ring approximation can be expanded upon to include two devices separated by distance. Figure 3.15 shows the diagram of the formula setup where the upper series of rings represents coil 'A' and lower set of rings represents coil 'B'. Here the two coils are separated by a distance z along the common axis of the rings. Equation 3.20 sums the mutual inductance each ring experiences from all the elements of the other body, resulting in the total mutual inductance. Equation 3.21 is used to calculate coupling coefficients of the two coils using their self and mutual inductance. In later section, this technique for calculating the coupling coefficients for varying distances will be used along with the circuit model to predict the behavior of the wireless power system.

Table 3.2: Measured lumped elements values for each individual circuit elements of the experimental transmitter and receiver.

TRANSMITTER		RECEIVER	
COMPONENT	VALUE	COMPONENT	VALUE
L_1	0.965 uH	L_4	0.967 uH
C_1	449.8 pF	C_4	448.9 pF
R_{p1}	0.622 Ω	R_{p4}	0.163 Ω
R_{source}	50 Ω	R_{load}	50 Ω
Q_1	0.91	Q_4	0.93
F_1	7.64 MHz	F_4	7.64 MHz
K_{12}	0.1376	K_{34}	0.1343
Q_2	304.3	Q_3	404.4
F_{o2}	7.66 MHz	F_{o3}	7.62 MHz
L_2	39.1 uH	L_3	36.1 uH
C_2	11.04 pF	C_3	12.10 pF
R_{p2}	6.19 Ω	R_{p3}	4.27 Ω

$$M_{ab} = \left(\sum_{i=1}^n \sum_{j=1}^m M_{ij} \right) \quad (3.20)$$

$$k_{ab} = \frac{M_{ab}}{\sqrt{L_a L_b}} \quad (3.21)$$

A summary of the extracted parameters for each of the individual elements from the experimental setup depicted in figure 3.5 are shown in Table II. All of the parameters extracted had a R^2 value of over 0.9999, which indicates, with high confidence, that the values model the system accurately.

3.5 Validation of Circuit Model and Measured Results

The process of comparing the theoretical model of the wireless power system to measured results will be presented in two steps. First, sections 3.5.1 and 3.5.2 use extracted values for coupling coefficient k_{23} from the complex S_{21} data to validate the circuit model independent of coupling (i.e. k_{23} is the only unknown variable from Table II and is extracted from the overdetermined S_{21} measurements). Second, section 3.5.3 uses Neumann's formula to

predict all of the coupling coefficients in the system, thus enabling a full prediction of system performance using only the lumped circuit values from Table II.

In this experiment, the transmitter and receiver (shown in figure 3.17) are placed facing each other along their common axis. This is depicted in figure 3.5.3 which represents a top view of the experimental setup. Ports one and two of a VNA are connected to the drive and load loops, respectively. Thus, the source and load resistance of the system is $50\ \Omega$. The drive loop and Tx coil are set a fixed distance apart (13.5 cm), thus keeping k_{12} constant. The Rx coil and load loop are similarly fixed at 13.5 cm. Finally, the receiver (as a single unit) is moved away from the transmitter along the common axis. The S_{21} scattering parameters are recorded every 5 cm, from 10-130 cm.

3.5.1 Effects of Parasitic Cross Coupling

Figure 3.10 compares experimentally measured $|S_{21}|$ data to the ideal model in equation (3.3) to a more complete asymmetric model that includes parasitic cross couplings terms (k_{13}, k_{24}, k_{14}). The agreement between the complete model and the experimental data is excellent. The difference in the magnitude of the $|S_{21}|$ peaks for the upper and lower modes can be explained by considering the phase of the two modes.

Based on the dynamics of coupled resonators [20], one expects that in the lower frequency mode the current in the transmit coil should be in phase with the current in the receive coil; in the higher frequency mode, the coil currents should be anti-phase (180 degrees out of phase). In the lower mode, in which the Tx coil and Rx coil are in phase, the parasitic feed-through from the drive loop to the Rx coil (associated with coupling constant k_{13}) contributes constructively to the magnitude of the current in the receive coil. In the upper mode, the Rx coil phase is inverted but the parasitic feed-through is not, so the feed-through interferes destructively with the Rx coil current. Similar arguments apply to the other parasitic couplings. The fact that the magnitude of the mode differences are modeled well only when parasitic couplings are included (as shown in figure 3.10) supports this conclusion.

A discrete matching network or shielded transformer could be used to directly connect

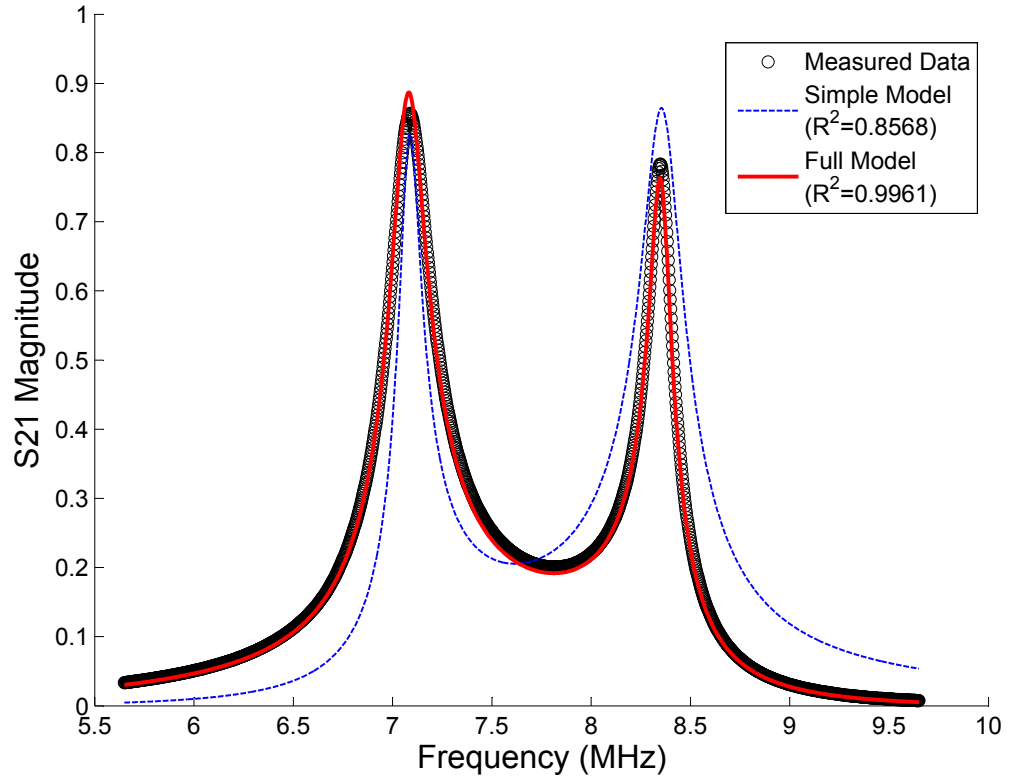


Figure 3.10: Comparison of experimental data (black dots) to the simplified transfer function (dotted blue line), and to the complete transfer function (red line). The simple model neglects parasitic cross coupling (e.g. k_{13}, k_{24}, k_{14}) and does not reproduce the amplitude difference between the upper and lower modes. The complete model reproduces this amplitude difference, which is explained by the phase of the parasitic coupling terms (k_{13}, k_{24}) relative to the non-parasitic terms (e.g. k_{23}) for the two resonant modes.

the source/load to the coils. This would eliminate the cross coupling term and simplify the model, and possibly also simplify system construction. On the other hand, the parasitic feed-through benefits system performance in the lower mode, and this benefit would be lost by eliminating the drive and load loops. Additionally, a discrete matching network would introduce extra power loss and reduce overall system efficiency.

3.5.2 Model with Extracted Coupling Coefficient vs Measured Data

Figure 3.11 shows a 3D plot of measured S_{21} data in linear magnitude form, depicted by black dots. These dots form striped rows, each of which correspond to a frequency sweep of data points taken with a VNA. Each row of dots (or frequency sweep) represents a VNA measurement taken every 5 cm as the receiver is moved away from the transmitter. The mesh underneath the measured data represents the transfer function of the circuit model using extracted and interpolated values for coupling coefficients. Frequency splitting, the point of critical coupling, and damping are clearly visible. For each of the frequency sweeps, R^2 was calculated to quantify the correspondence between theory and measurements. The average R^2 value for the 25 measurements is 0.9875. It is important to note that both figure 3.10 and figure 3.11 show a slight under prediction for the high frequency mode and a slight over prediction for the low frequency mode. This is believed to be due to capacitive detuning and/or capacitive coupling (which is not modeled) and becomes more significant at close range.

3.5.3 Model with Calculated Coupling Coefficients vs Measured Data

In the preceding section the model was compared to measured data for discrete values of coupling coefficients. Since the circuit model itself does not explicitly model distance, it is necessary to calculate the coupling between each inductive element as a function of distance. In the following analysis these calculated values of coupling coefficients, along with the L,C,R values listed in Table II, are inserted into the transfer function of the full system and are compared to measured results. In order to present a clean comparison of theory and measured results, figure 3.13 shows the magnitude of the measured scattering

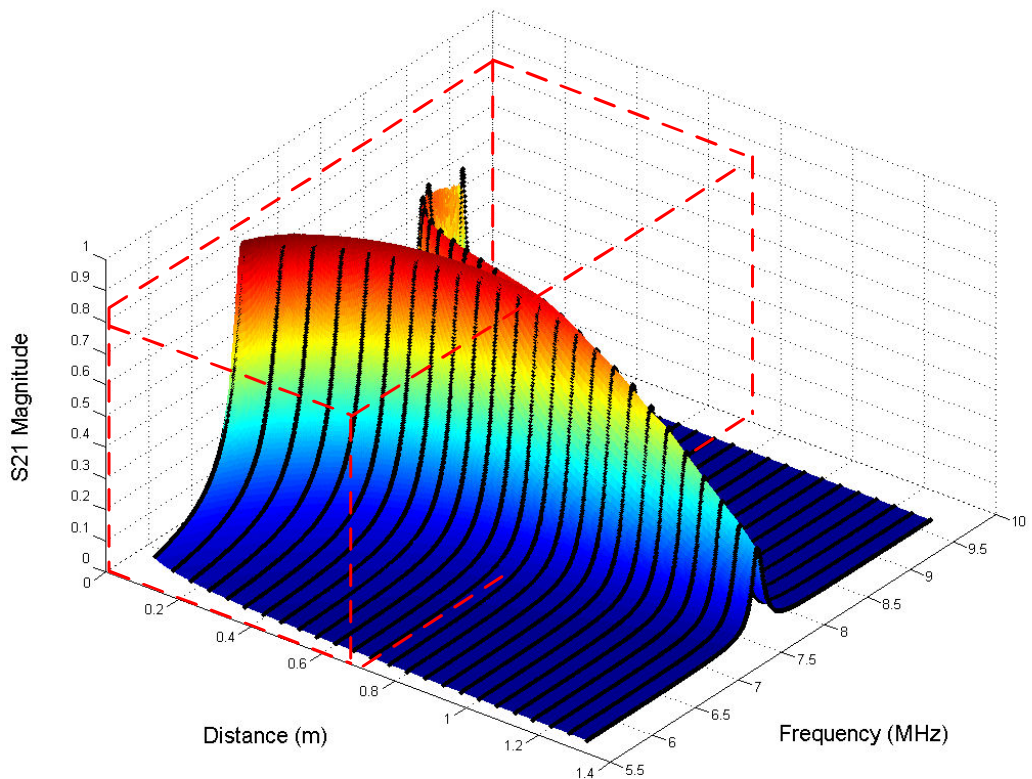


Figure 3.11: Measured $|S_{21}|$ data (black dots) plotted in magnitude form. Each row of black dots represents a frequency sweep taken by the VNA every 5cm as the receiver was moved away from the transmitter. The mesh underneath the data is the theoretical model.

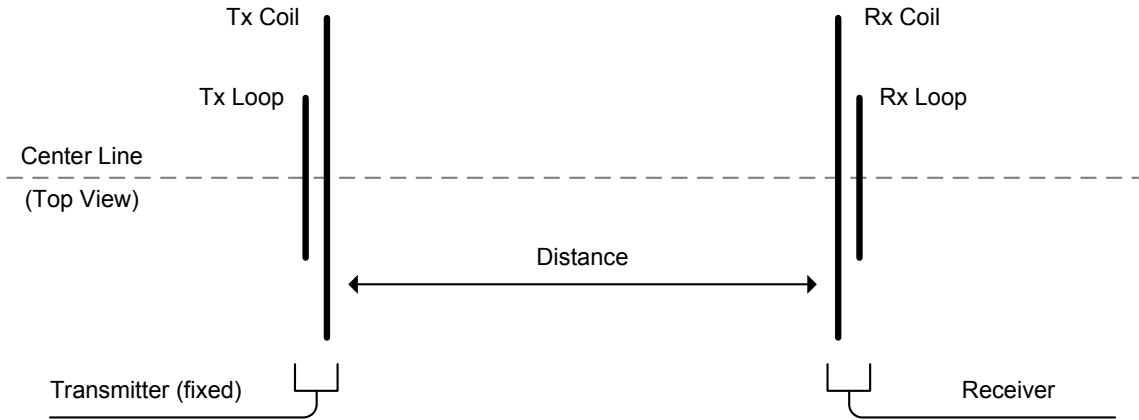


Figure 3.12: Diagram depicting the top view of the experimental setup where the receiver, as a single unit, is moved away from the transmitter. In this experiment the free variable is the coil to coil coupling (k_{23}) which varies as a function of the distance between the coils.

parameter ($|S_{21}|$), as a function of system distance, at the center frequency ($f_o = 7.65$ MHz). When the distance between the transmitter and receiver is small, the system is over-coupled and the magnitude of the power transferred is small at this operating frequency. This is a result of frequency splitting, which causes resonant modes at frequencies higher and lower than the center frequency of ω_o . As the distance is increased, the system becomes critically coupled and the magnitude is at its highest. As the distance between the coils is further increased, the system becomes under-coupled and the magnitude of the transferred power begins to fall. The calculated red line of system performance in figure 3.13 shows a good match with the measured data. The blue marker on the plot shows the predicted value for the critical coupling point, using the asymmetrical form of equation (3.8) and (3.9), along with Neumann's formula to calculate the distance for coupling coefficient k_{23} .

Frequency splitting is further investigated in figure 3.14, which shows the calculated and measured magnitude for each mode of the system as a function of distance (left) along with the resonant frequency of each mode as a function of distance (right). Here, the derivative of the transfer function is taken with respect to ω , and set to zero to calculate the maximum magnitude for a given distance. The discontinuity in the prediction of the high frequency branch occurs when the two modes begin to merge near the critical coupling point. This

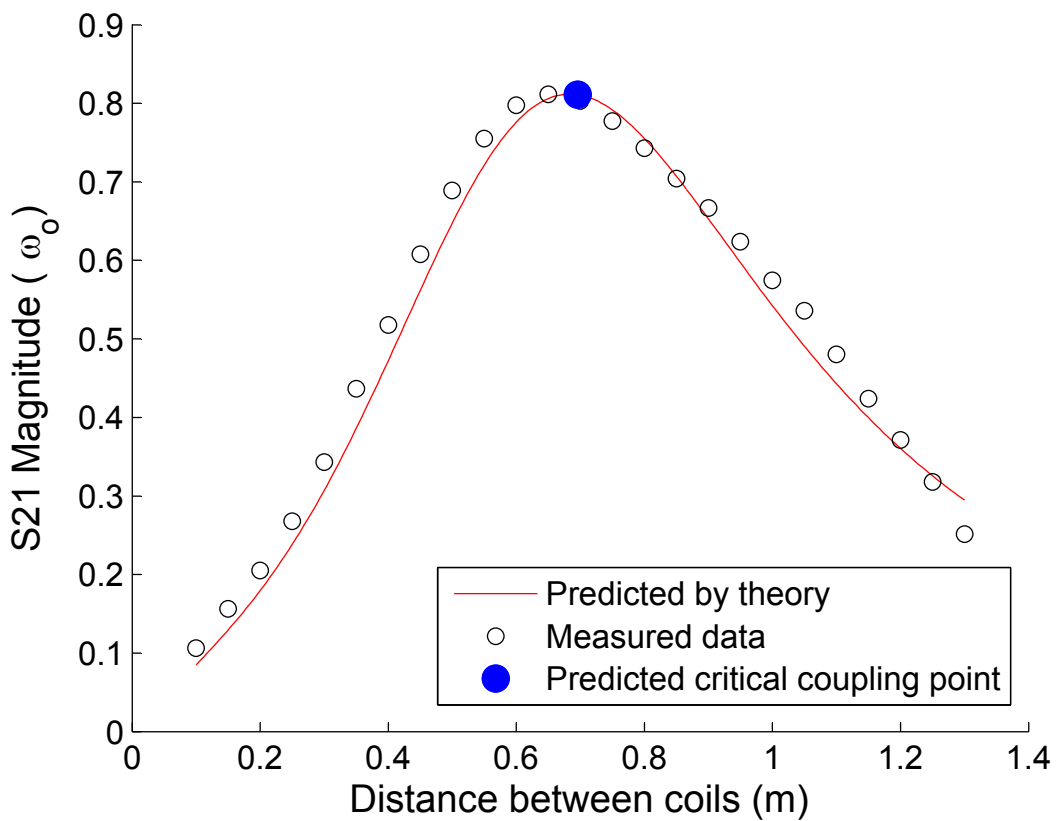


Figure 3.13: Predicted behavior of the wireless power system at the individual coil resonant frequency (f_o) using Neumann's formula along with the predicted critical coupling point (blue dot) and S_{21} measured data.

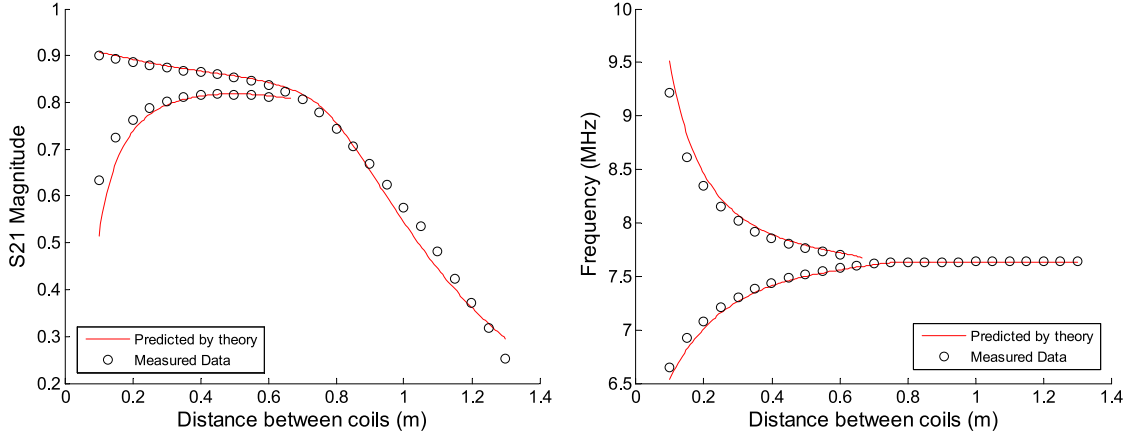


Figure 3.14: Calculated and measured frequency splitting plotted as a function of distance. The S_{21} magnitude of the two modes is shown on the left and frequency of the two modes is shown on right.

results in a non-zero slope for the peaks of the smaller high frequency mode, and thus the derivative does not reach zero. Here the circuit model plus Neumann's formula shows a good prediction of the performance of the wireless power system. The magnitude vs. frequency plot in figure 3.14 shows a noticeable under-prediction for the high frequency mode at small distances. It is believed this is caused by capacitive detuning having a more pronounced effect as the transmitter and receiver are moved very close to each other.

Figure 3.15 compares extracted and predicted coupling coefficients for the coil to coil coupling, k_{23} (left panel) and loop to coil coupling with the assumption that $k_{12} = k_{34}$ (right panel). The error bars show the confidence of the unconstrained nonlinear optimization fitting routine. For long distances the extracted and calculated values for coupling show good agreement. However, at shorter ranges, the calculated method shows an over prediction of coupling. This over prediction manifests itself in figure 3.11 as an under estimation of the high frequency magnitude at short ranges.

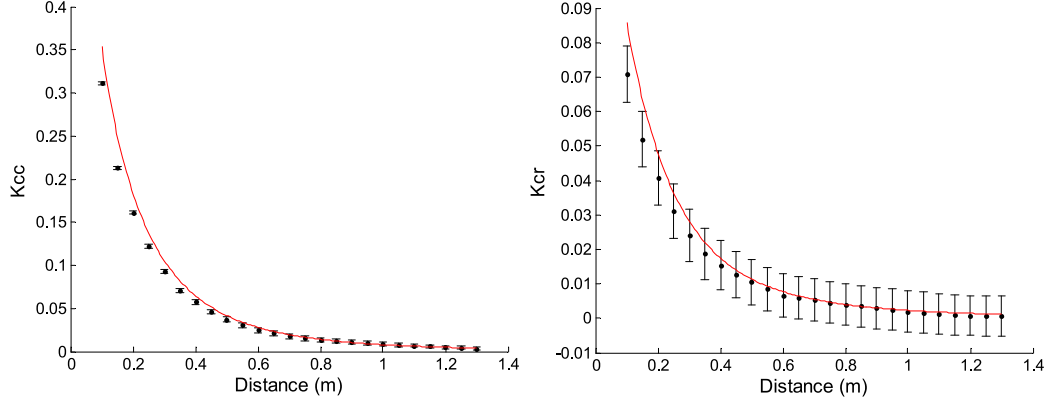


Figure 3.15: Extracted coupling coefficient with confidence bars and calculated coupling coefficients using the Neumann's formula (red line)

3.6 Adaptive Tuning for Range Independent Maximum Power Transfer

A necessary component for a compelling wireless power system is the ability to operate at a multitude of distances and orientations without the need for precision manual tuning.

3.6.1 Automatic Frequency Tuning

Using frequency splitting presented here, it is possible to design a system that automatically adjusts to provide maximum possible efficiency as a user moves the receiver to locations within the system's working range (i.e. $k_{23} > k_{critical}$). Introducing a directional coupler between the amplifier and drive loop, as shown in figure 3.1, allows the transmit system to continuously measure the incident and reflected power as a function of frequency. Since this system forms a transmission line, the power not consumed by the load or lost to parasitic resistance is reflected back to the source.

Figure 3.16 shows a graph of transfer efficiency vs. distance for the fixed frequency case of $f_o = 7.65MHz$, and the auto-frequency tuning case. The experiment is done in the same manner as the VNA measurements in the previous section. The receiver was incrementally moved away from the transmitter along the system's common axis; the source resistance was the 50 ohm amplifier/decoupler and the load resistance was a 50 ohm RF

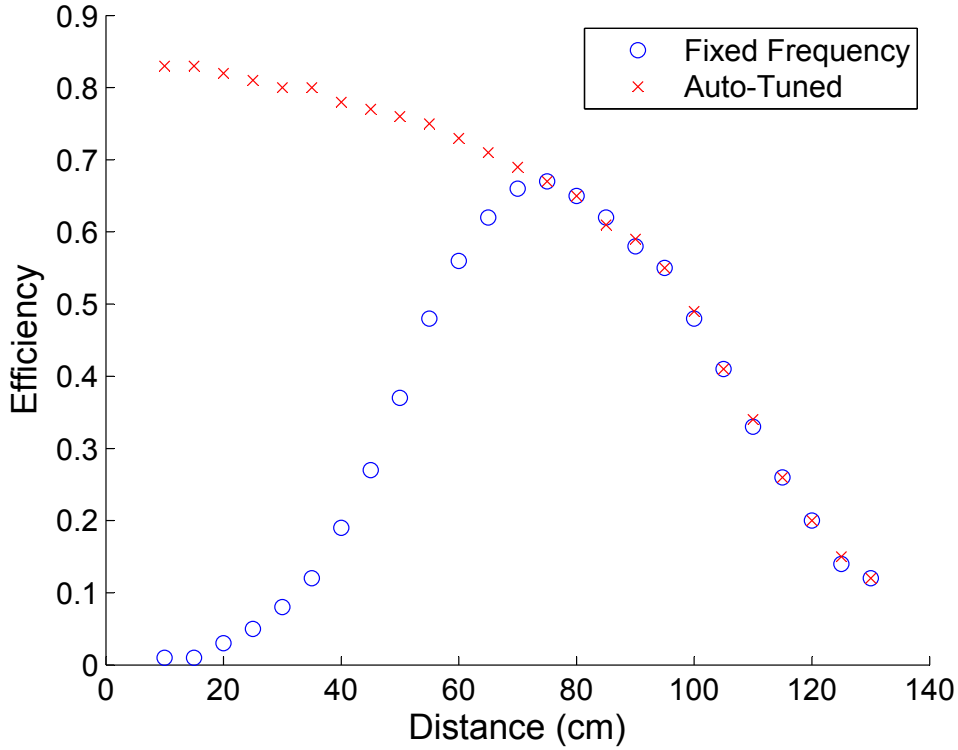


Figure 3.16: Automatic frequency tuning compared to a fixed drive frequency as a function of distance between the transmitter and receiver.

power meter. In this case, the transmitted power was 30 Watts as opposed to the signal level measurements done with the VNA. When the frequency tuning is enabled, the controller picks the maximum resonant peak and tracks it as the receiver is moved away from the transmitter. The plot shows that at short ranges the system is very efficient compared to the fixed-frequency case. As distance is increased the efficiency decreases slowly until the critical coupling point where the two modes merge and the system returns to the under-coupled regime.

One of the key principles of this system is that frequency splitting is a function of the coil to coil coupling coefficient. In the above analysis, we show how the coupling, and therefore the power transfer, varies as a function of distance along the transmission axis. The coupling will also vary with orientation. As long as the receiver is sufficiently close to

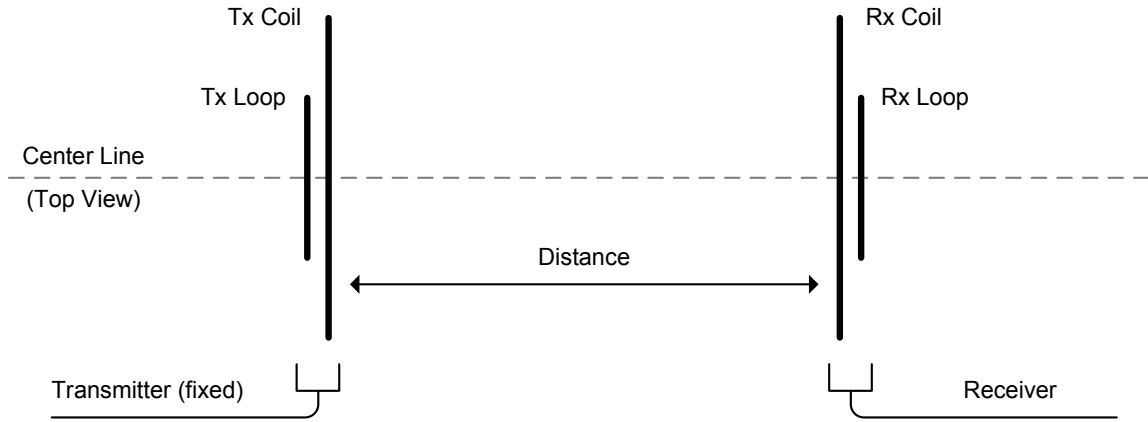


Figure 3.17: Diagram depicting the top view of the experimental setup where the receiver, as a single unit, is moved away from the transmitter. In this experiment the free variable is the coil to coil coupling (k_{23}) which varies as a function of the distance between the coils.

the transmitter, almost any orientation and/or position will cause some amount of mutual inductance between the two coils. If this mutual inductance results in sufficient coupling (i.e. $k_{23} > k_{critical}$) automatic frequency tuning can be used to find the frequency that will result in the highest possible transfer efficiency. To demonstrate orientation independence figure 3.18 shows a plot of power transfer efficiency versus orientation as the receiver is rotated from $0^\circ - 90^\circ$, for both fixed-frequency and auto-tuned operation. Here the receiver unit is placed on axis at a fixed distance of 50 cm as depicted in figure 3.19. As the receive coil is rotated, the amount of magnetic flux that passes through the opening of the coil decreases. Thus, the fixed frequency case experiences the same trend of transitioning from the over-coupled to critical-coupled to under-coupled regimes as in the previous examples. When frequency tuning is applied, a nearly constant efficiency can be obtained until the receiver is rotated past 65° .

3.6.2 Impedance Adaptation Techniques for Narrow band Operation

For regulatory reasons, it may be desirable for the wireless power system to be able to function in a narrower band than the frequency tuning systems described so far. For example,

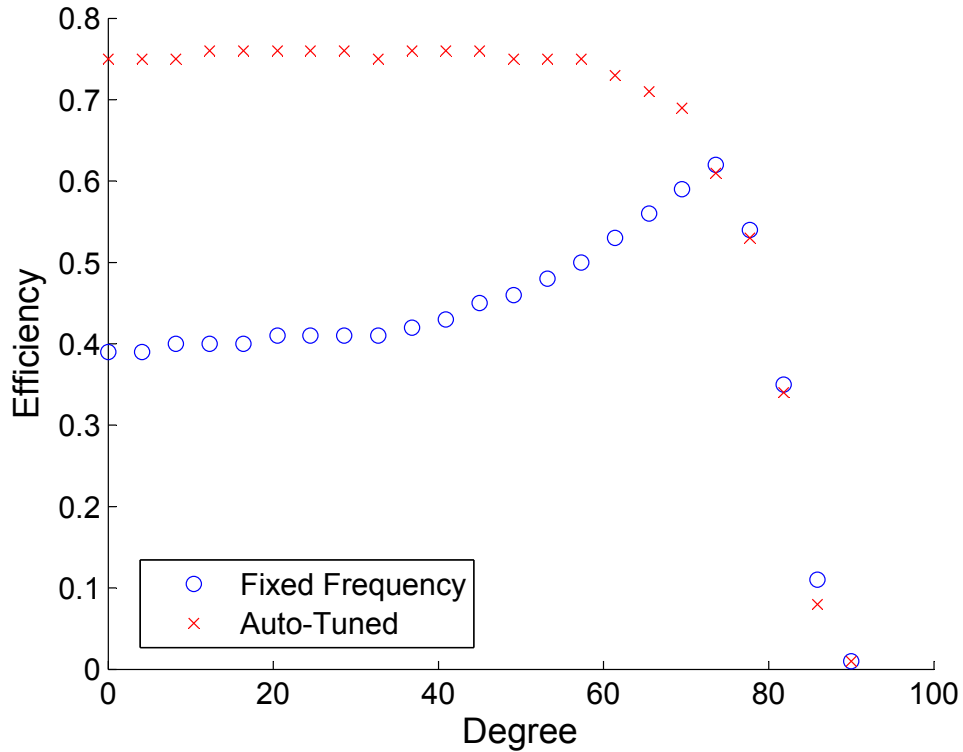


Figure 3.18: Automatic frequency tuning compared to a fixed drive frequency as a function of the angle between the transmitter and receiver. An angle of 0° degree corresponds to the coils facing each other, while 90° degrees corresponds to the receiver perpendicular to the transmitter. The transmitter to receiver spacing is 0.5 meters.

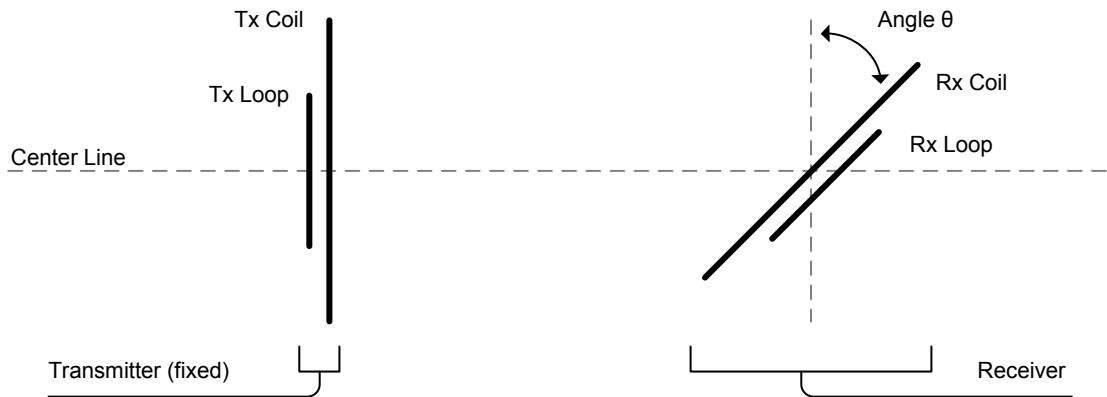


Figure 3.19: Diagram depicting the top view of the experimental setup where the orientation of the receiver is varied by angle θ at a fixed distance from the transmitter.

one might want the wireless power system to stay inside an ISM band. This section describes narrow band wireless power transfer schemes that can support range and orientation adaptation by tuning system parameters other than frequency.

Rather than considering k_{lc} to be a static design parameter to be optimized (as above), one can consider it a dynamically variable impedance matching parameter that can enable range adaptation without frequency tuning. Figure 3.20 shows a plot of S_{21} magnitude as a function of k_{23} and k_{lc} (for symmetric loop to coil coupling). This figure shows that adapting the loop to coil coupling to compensate for a non-optimal k_{23} is another method for adapting to varying range and orientation.

If the system is driven at ω_0 and the wireless power system is operating in the over-coupled regime ($k_{23} > k_{critical}$), frequency splitting will result in the system being off resonance, and little to no power will be transferred. To bring the efficiency of the system back to a maximum, k_{lc} can be decreased, causing $k_{critical}$ in equation (3.8) to decrease, until $k_{23} = k_{critical}$, at which point maximum power transfer can resume. In a laboratory demonstration we have successfully implemented a form of this tuning method that allows tuning for a variety of Tx-Rx distances (k_{23} values) with a hand adjustment of a loop that can be rotated about its coil, thereby changing k_{lc} . The k_{lc} adaptation method has the advantage of allowing operation at a single frequency ω_0 , which would be advantageous for band-limited operation. Thus, it is of practical interest to develop electronically controllable techniques for k_{lc} tuning. As noted earlier, the system's loops can be replaced by discrete matching networks; making these matching networks electronically variable could allow for automatic k_{lc} tuning.

3.7 Summary

One compelling usage scenario is a workspace where devices such as laptops, cells phones, and USB peripherals are seamlessly powered and recharged as easily as data is transmitted through the air. As a final demonstration of the potential of this type of wireless power system, figure 3.21 shows a laptop being continuously powered via the magnetically coupled resonators. Here the laptop battery has been removed and the wireless power system is providing all the power needed for operation. The signal generator, amplifier, and directional

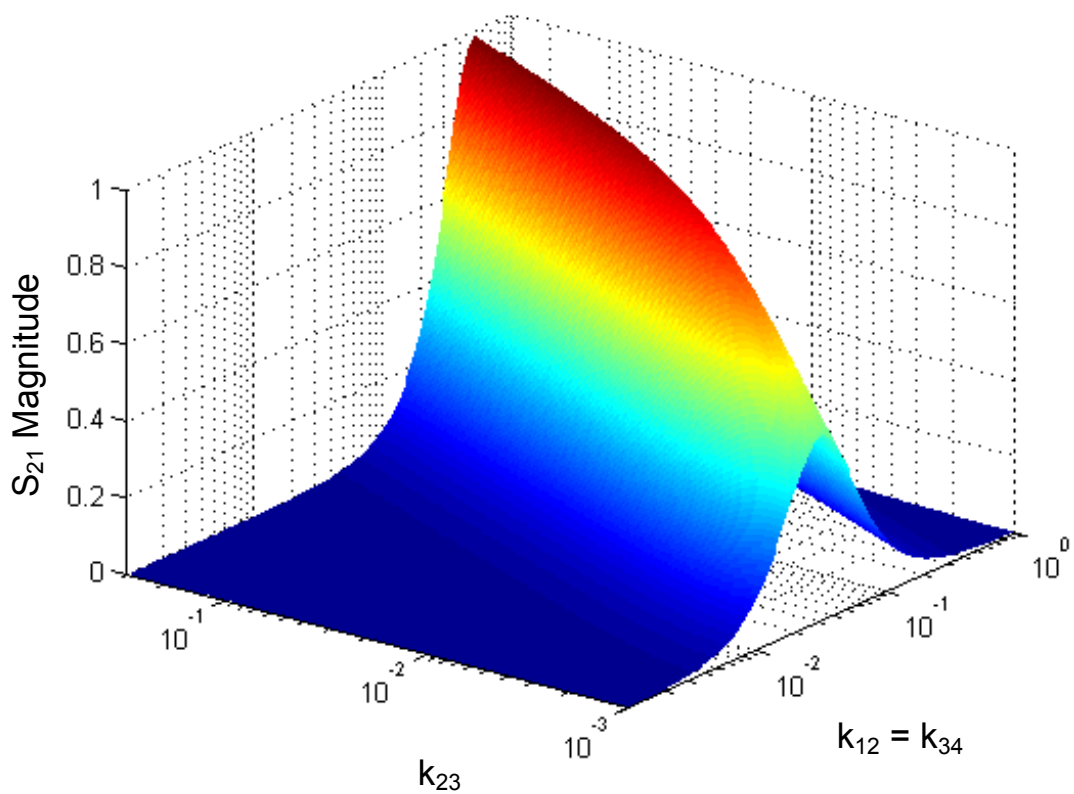


Figure 3.20: The magnitude of power transfer ($|S_{21}|$) as a function of the coil to coil coupling (k_{23}) vs the loop to coil coupling (where $k_{12} = k_{34}$). This plot shows that given a particular range (i.e. k_{23}) there exists a loop to coil coupling that will maximize power transfer.

coupler can be seen in the background (top left corner) and are controlled by a computer. The amplifier drives the same 28 cm transmit loop and 59 cm transmit coil from the earlier experiments. The receiver is placed 0.7 meters from the transmitters and consists of a smaller 28 cm coil and a 30 cm loop, seen in the foreground. A simple bridge rectifier is used to provide DC power to the modified laptop power brick. In this demonstration the removed battery has been placed next to the laptop (visible in the lower right). The RF amplifier output to DC laptop input efficiency is 50% (which includes the efficiency of the non-optimized rectifier and power brick).

The use of magnetically coupled resonators for wireless power transfer offers many exciting opportunities and design challenges. In this chapter I have presented new analysis that yields critical insight into design of practical systems, including the introduction of key figures of merit that can be used to compare systems with vastly different geometries and operating conditions. A circuit model is presented along with a derivation of key system concepts such as frequency splitting, the maximum operating distance (critical coupling), and the behavior of the system as it becomes under-coupled. This theoretical model is validated against measured data and shows an excellent average coefficient of determination (R^2) of 0.9875. An adaptive frequency tuning technique is demonstrated, which compensates for efficiency variations encountered when the transmitter to receiver distance and/or orientation are varied. The method demonstrated in this paper allows a fixed-load receiver to be moved to nearly any position and/or orientation within the range of the transmitter and still achieves a near constant efficiency of over 70% for a range of 0-70 cm.

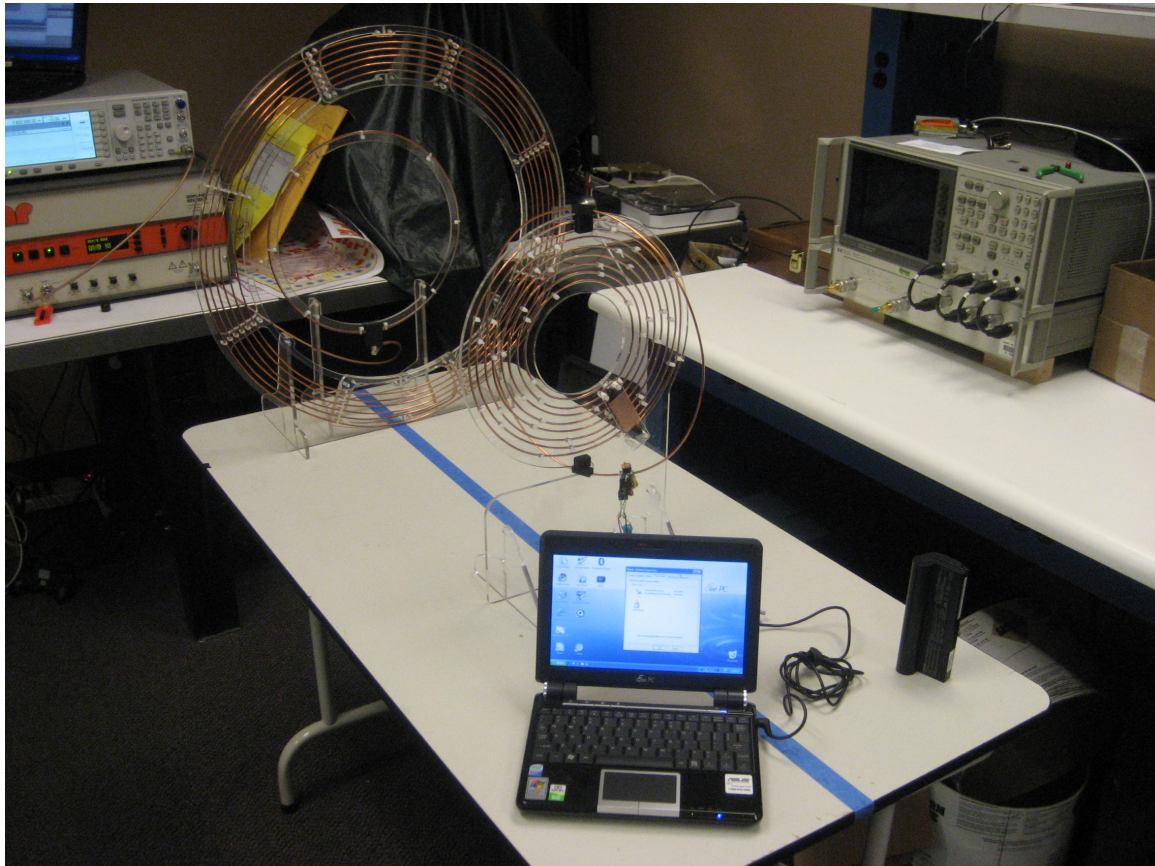


Figure 3.21: Wirelessly powered laptop computer. The battery has been removed and is visible in the lower right of the table. The wireless power system is able to provide all of the laptop's peak power consumption of 12 Watts at a range of 0.7 meters. Including the rectifier (which has not yet been optimized), the system efficiency (measured from amplifier output through to the laptop) is 50%.

Chapter 4

WIRELESS IDENTIFICATION AND SENSING PLATFORM

Over the last decade, advances in integrated circuit design and RFID manufacturing techniques have enabled a cost effective method for producing passive Radio Frequency Identification (RFID) tags capable of reporting a unique ID when queried. These devices typically consist of a printed antenna bonded to an integrated circuit (IC), and are completely powered from the RF energy transmitted by an RFID reader. Once the tag is powered on, the ICs digital logic analyzes data from the RFID reader and responds with a unique ID when necessary [19].

One of the motivations for my work on RFID is to capture the truly wireless, micro-computing nature of passive RFID tags, and explore applications beyond simple barcode replacement. My objective has been to investigate the building blocks and algorithms necessary to create a general purpose Wireless Identification and Sensing Platform. Referred to as a WISP, this device will be an enhanced passive RFID tag, with sensing and computing capabilities, that remains completely wirelessly powered.

4.1 Prior work

To date, there are several approaches for incorporating sensing capabilities into RFID. Active tags, a subclass of RFID tags, use batteries to power their communication circuitry, sensors, and microcontroller. Active tags benefit from relatively long wireless range (approximately 30 m) and can achieve high data and sensor activity rates. However, the batteries required by active tags are disadvantageous for device cost, lifetime, weight, and volume.

In contrast, passive sensor tags receive all of their operating power from an RFID reader and are not limited by battery life. There are several examples of application-specific, non-programmable passive tags with integrated temperature and light sensors, as well as an Analog to Digital Converter (ADC) [12, 35]. One attractive feature of passive sensor

tags is the prospect of permanently embedding them in objects for structural, medical, or product monitoring. Another advantage is their suitability for applications in which neither batteries nor wired connections are feasible, due to weight, volume, cost, or other reasons. One limitation of purely passive sensor tags is the required proximity to an RFID reader. However, other methods such as solar, thermal, or kinetic energy harvesting could be used as a secondary power source, if needed.

A further consideration is the configurability and computational power of RFID sensor tags. Existing devices are generally fixed-function with respect to sensory inputs and they lack computational capabilities. A commercially available RFID tag with some additional functionality is described in [41]; however, this device can only transmit one bit of sensor data in addition to its ID. Furthermore, it is limited by a short read range, due to its 125 kHz operating frequency.

4.2 WISP Overview

As part of my work on developing wirelessly powered systems based on UHF RFID technology have published several articles on the design and performance of the Wireless Identification and Sensing Platform (WISP), a battery-free, programmable RFID sensor device [54, 55], shown in figure 4.4. Compliant with the Electronic Product Code (EPC) Class 1, Generation 2 protocol, WISP can transmit 64 bits of data per query and is fully configurable due to its ultra-low power 16-bit general-purpose microcontroller. Similar to conventional passive UHF RFID tags, WISP has no batteries and is completely powered via the RF energy transmitted by an RFID reader.

The WISP is manufactured as a printed circuit board (PCB), which offers a number of benefits when compared to traditional Integrated Circuit (IC) tag designs. A few of these advantages include low development cost, fast design cycles, and easy debugging and measurement of circuit parameters. The PCB implementation allows the flexibility to physically add and remove sensors and/or peripherals to create devices for new applications. In contrast, IC implementations offer the ability to customize components and to decrease power consumption (yielding better range), as well as creating devices with a smaller form factor and at a lower cost when manufactured in high volume.

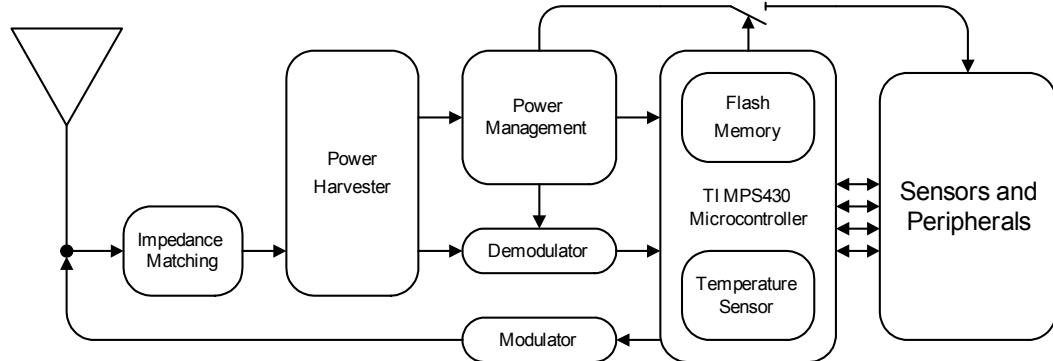


Figure 4.1: Block Diagram of the WISP

A block diagram of the WISP is shown in figure 4.1 and is similar in function to traditional IC RFID tags. The antenna is balanced by an impedance matching network and is fed into the RF power harvester. The Radio Frequency (RF) signal transmitted by the RFID readers is rectified into DC voltage to power the rest of the tag. The demodulator block converts the Amplitude Shift Keyed (ASK) data that is superimposed on the RF carrier into a logic level stream of serial data. This extracted serial data is parsed by the MSP430 microcontroller (MCU) to receive downlink data from the reader. Uplink data is sent via the modulator circuit, which back-scatters the signal by changing the antenna impedance. Finally, the microcontrollers internal temperature sensor, as well as any external sensors, are powered and measured by the MCU.

Since the power consumption of the microcontroller, sensors, and peripherals are much greater than that seen in traditional passive RFID technology, the WISP duty cycles between active and sleep mode. In sleep mode, the WISP shuts down and reduces its current consumption to a few micro-amps and energy is accumulated by the harvesting RF power over multiple EPC queries. Once sufficient voltage is obtained, the WISP polls sensors and communicates with the RFID reader.

Figure 4.2 depicts the WISP platform, made of a four layer FR4 PCB with components on both sides and an integrated dipole antenna. The WISP in its base configuration has

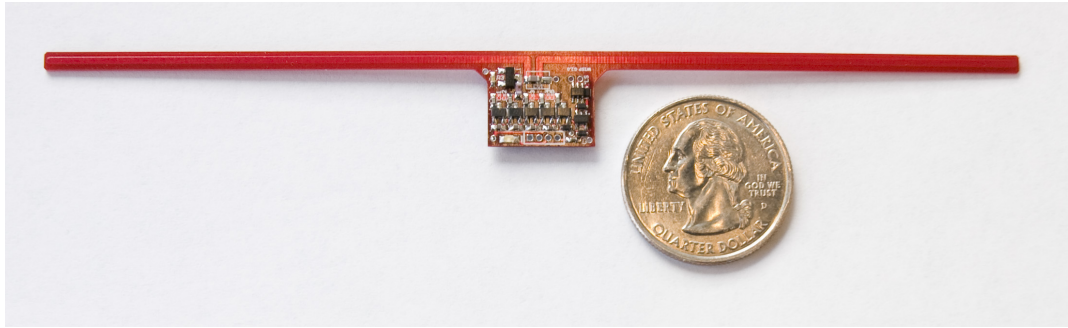


Figure 4.2: Wireless Identification and Sensing Platform (WISP), version G2.0

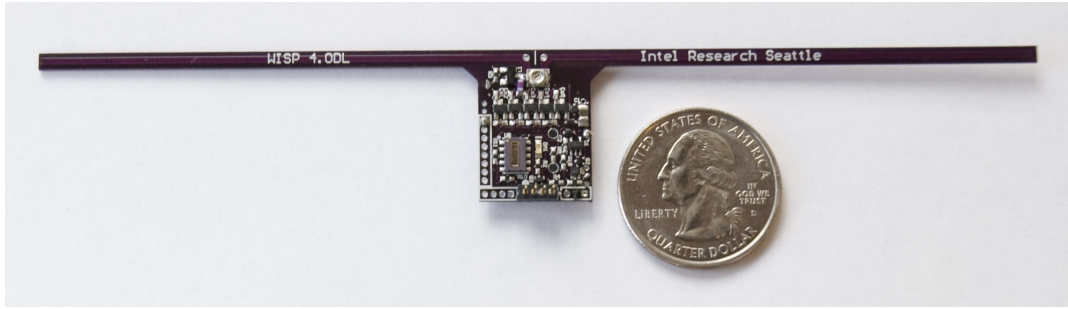


Figure 4.3: WISP Data logger, version 4.0DL

several onboard sensors: a circuit for measuring the rectified supply voltage, a temperature sensor, and a 3D accelerometer. Small header pins expose all ports of the microcontroller for expansion to daughter boards, external sensors, and peripherals. Finally, a low current surface mount LED is included in the design. Figure 4.3 shows the data logger version of the WISP which has additional features, such as a larger microcontroller, a real time clock, external EEPROM, and an optional 0.1 Farad super capacitor for extended lifetime. Figure 4.4 shows WISP 4.1 DL which is the latest version of the WISP. This version contains the same feature set as its 4.0 but has a smaller MSP430 which has less power consumption.

4.2.1 Analog Front End

The defining characteristic of far field RFID systems is that tags can be read at a significant distance, generally on the order of 2-10 meters. For passive RFID, this requires that the



Figure 4.4: Blue WISP, version 4.1DL

RFID reader transmits sufficient energy to power the tag at large distances. However, due to regulatory limits on the amount of power that can be transmitted and the path loss associated with electromagnetic propagation, there is very little power that actually reaches the tags. Therefore, the power harvesting circuit must maximize the operating distance by converting the very limited incoming RF power to DC power with sufficient voltage to activate the tag. The RF power received by the WISP's dipole antenna is fed to the analog front end depicted in Figure 4.5. A discrete matching network is used to provide the maximum power transfer from the antenna to the rectifier. RF Schottky diodes, specifically designed for 915MHz low power applications, were selected to make a five-stage voltage doubling circuit. This circuit converts the AC input signal to DC power which is fed into a storage capacitor.

For RF rectifiers of this type, the input and output impedances are not well isolated. Further confounding the problem, the output impedance of the rectifier is fairly high; an undesirable trait for any power source. This means that as the load on the rectifier changes the input impedance also changes, resulting in the analog front end becoming mismatched to the antenna. This leads to the problem of selecting values for the impedance matching network when it is not possible to guarantee constant input impedance.

To determine the correct values for the matching network the operating cycle of the WISP must be taken into account. First, the WISP is most effective at storing harvested energy when it is in sleep mode, as the current consumption is minimal. Second, the

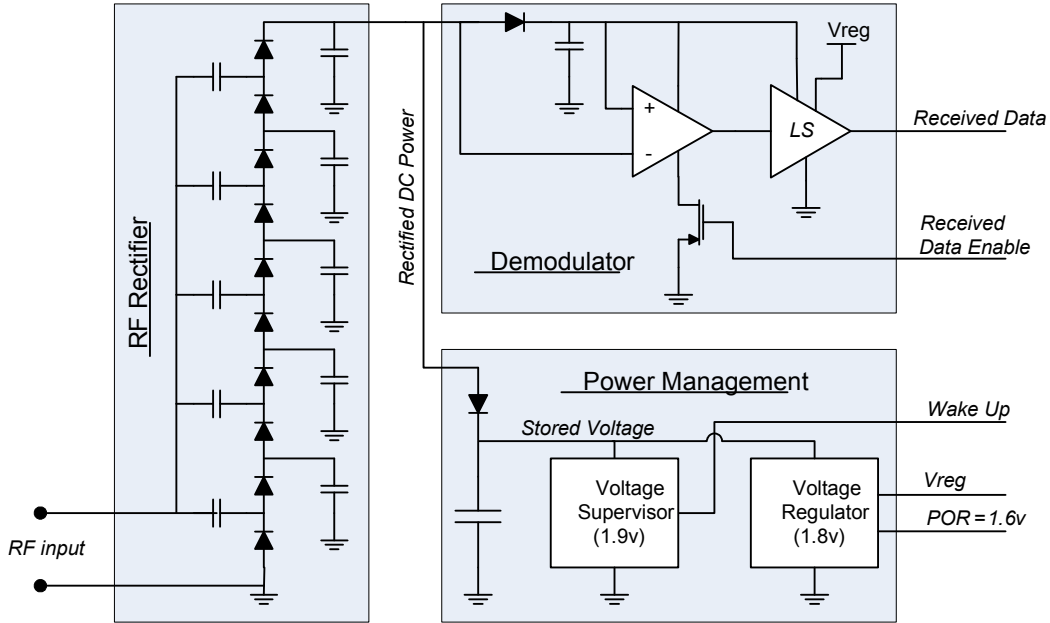


Figure 4.5: Schematic of the Analog Front End.

WISP will spend most of its time repeatedly charging up to 1.9 V and then discharging to approximately 1.8 V. Thus, to determine the correct matching values, the WISP is placed into sleep mode and the impedance matching network is swept with a variable capacitor until 1.9 V is produced for the lowest possible input power. Stated another way, the key parameter for maximizing the read distance of the WISP is minimizing the quiescent current consumption so that the minimum operating voltage of 1.9 V (supervisor threshold) can be rectified with the lowest possible input power.

4.2.2 Demodulation and Modulation

The EPC Gen 2 standard defines that reader-to-tag communication uses ASK modulation on a carrier wave in the range of 902-928 MHz. When not transmitting data, the carrier waveform remains at a constant amplitude; when bits are transmitted, the amplitude of the carrier drops to at least ten percent of its normal value, and the phase of the carrier may be reversed. The duration of the continuous waveform between these low amplitude pulses indicates logical “ones” or “zeros”.

Figure 4.5 shows a schematic of the WISP's demodulator circuit. The output of the harvester is fed through the diode, which supplies power to the comparator and acts as a reference for the level shifter. A capacitor is used to filter out transients while allowing proper biasing at varying distance and received power levels. When activated, the current consumption of the comparator functions as a constant-current source, pulling current through the diode. In this way, the voltage drop across the diode is used as a detector, where current supplied by the harvester (high amplitude RF modulation) results in positive voltage, and a lack of current (low amplitude RF modulation) yields negative voltage. The comparator is used to generate a rail-to-rail logic level waveform, and the level shifter converts the unregulated logic level to the regulated logic level. It is important to optimize current consumption and speed when choosing a comparator. Further savings can be achieved by disabling the comparator when there is insufficient voltage to start up the MSP430.

An example of a demodulated signal is shown in figure 4.6. This oscilloscope plot shows the 915 MHz RFID waveform and the resulting demodulated signal. Note that time frame is 20 μ S per division and thus, the individual cycles of the 915 MHz carrier are not visible. However, the ASK modeled data is visible as gaps in the carrier and enveloped signal. RFID tags do not actively transmit radio signals. Instead, they modulate the impedance of their antenna which causes a change in the amount of energy reflected back to the reader. This modulated reflection is typically called backscatter radiation. In order to change the impedance of the antenna, a transistor is placed between the two branches of the dipole antenna. When the transistor conducts current, it short-circuits the two branches of the antenna, changing the antenna impedance. In the non-conducting state, the transistor has no effect on the antenna and thus, the power harvesting and data downlink functions occur as if it were not present. This impedance modulation is currently implemented with a 5 GHz RF bipolar junction transistor, which allows for effective shunting of the 915 MHz carrier wave.

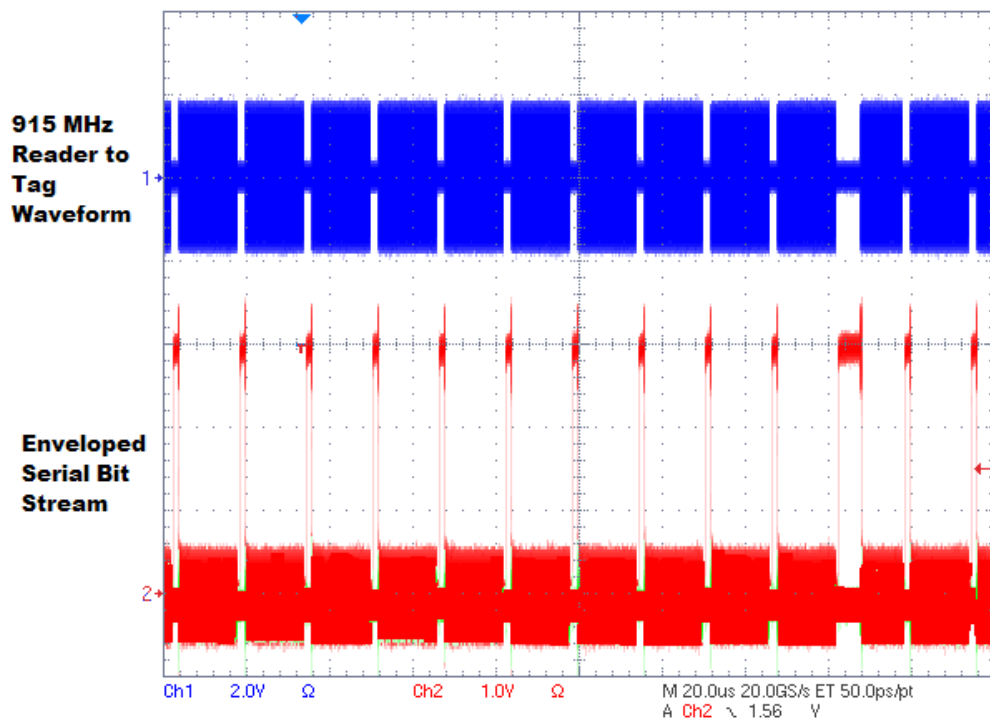


Figure 4.6: Oscilloscope plot of the demodulated data extracting data from the RF waveform transmitted by the RFID reader.

4.2.3 Digital Section and Power Conditioning

Since the power available to RFID tags is extremely limited, careful component selection must be made to minimize current consumption. As advances in IC manufacturing now allow discrete components with less than $1 \mu\text{A}$ of current consumption and operation at 1.8 V, it is now possible to construct working, wirelessly powered RFID tags with discrete components.

The general purpose computation capabilities of WISP are provided by an ultra-low power microcontroller. This 16-bit flash microcontroller, the MSP430F1232, can run at up to 4 MHz with a 1.8 V supply voltage and consumes approximately $600 \mu\text{A}$ when active at those frequency and voltage settings. Of particular interest for low power RFID applications, the MSP430 has various low power modes. Its minimum RAM-retention supply current is only $0.1 \mu\text{A}$ at 1.5 V. The device provides over 8 kilobytes of flash memory, 256 bytes of RAM, and a 10-bit, 200 kilo-samples-per-second Analog to Digital Converter (ADC). The low power consumption of this relatively new device is a critical factor in enabling use of a general purpose microcontroller in passive RFID systems.

Another critical design consideration is operation with uncertain power supply conditions. Because the available RF power varies greatly throughout device operation, supervisory circuitry is necessary to wake and sleep the device based on the supply voltage level. WISPs use a 1.9 V supervisor and a 1.6 V power-on-reset to control device state and reset the microcontroller, respectively. The supervisor provides roughly 100 mV of headroom on the storage capacitor above the 1.8 V of regulator voltage. This serves to buffer the supply voltage from dropping below 1.8 V, due to the large power consumption of the microcontroller in active mode.

4.3 Firmware & Power Management Algorithm

The WISP is essentially a software defined RFID tag, which uses the MSP430 to implement the EPC Class-1 Generation-2 protocol and performs sensing and computation tasks. There are significant challenges when developing applications on the WISP as compared to battery powered embedded systems. Primarily, there is no guarantee that a given task can be

completed before running out of power. Although the voltage supervisor provides headroom above 1.8 V, the rate at which the energy stored in the supply capacitor is consumed is directly affected by the design choices of the programmer. Failure to properly manage sleep cycles when the WISP harvests energy or inefficient coding practices can result in poor performance.

The WISP software can be described on three levels. At the lowest level is the power management algorithm, which is responsible for managing the device state, including sleep vs. active modes. Built on that is the communication layer, which enables bi-directional communication by sampling downlink data bits, implementing a Gen 2 state machine, and generating uplink data bits. The third level is the application layer where users implement custom function and encoding data in the appropriate EPC packets.

4.3.1 Power Management Algorithm

Meeting the low power requirements of passive RFID tags requires that the MCU consumes, on average, as little power as possible. As mentioned previously, this is achieved by duty cycling between active and low power sleep states. The key is that the WISP receives a constant amount of power as defined by Friis path loss equation (4.2) for a set distance. When the WISP is in active mode the power consumption far exceeds the power harvested. However, when the WISP is in sleep mode, the total current consumption of all the circuits is a few micro-amps and there is a net power gain which charges the storage capacitor. Therefore, duty cycling does not simply yield lower power consumption; it represents two different states: power harvesting and active operation.

The state diagram for the power management layer is shown in figure 4.7. State transitions are primarily driven by hardware interrupts from the voltage supervisor, which indicate if there is sufficient energy stored for operation. Initially, the WISP is away from an RFID reader and is in a power down state. When the WISP is brought within range of a reader, it begins to harvest power and the voltage across the storage capacitors begins to rise. At approximately 1.6 V the MSP430 powers up in a reset state and begins executing code. Since this event is not driven by the supervisor, it is important that the code enters sleep

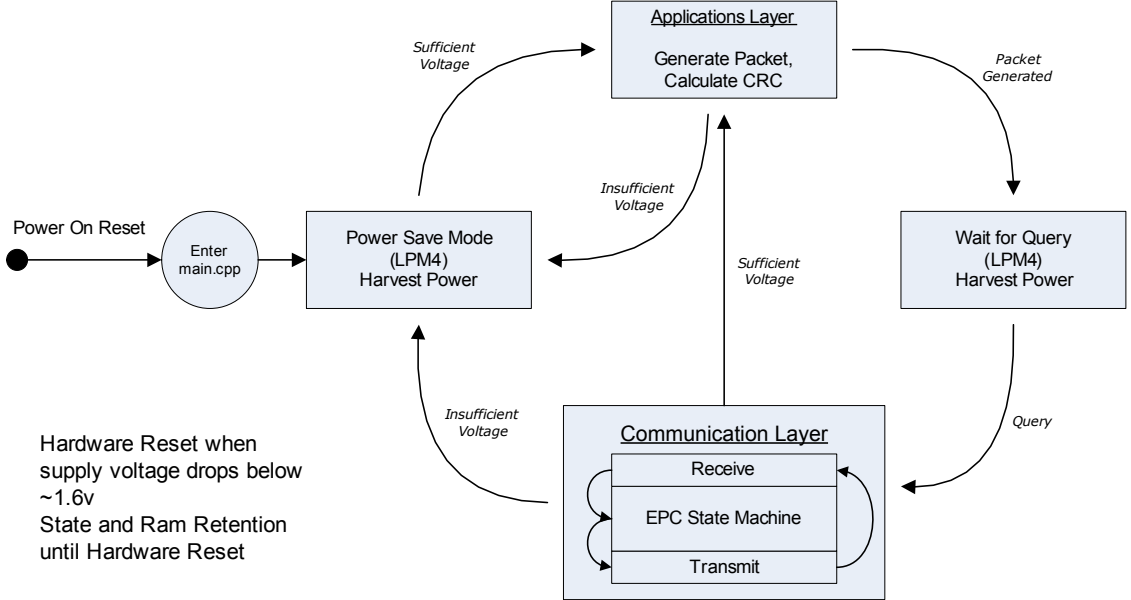


Figure 4.7: Block diagram of the power management algorithm for the WISP

mode (LMP4) as quickly as possible in order to repeatedly avoid brownout on start up. Once in LMP4, the WISP waits for sufficient voltage (1.9 V), as indicated by the supervisor interrupt. Next, the state machine transitions to the application layer, which performs user defined functions, such as sensor measurements. Here, an EPC packet is generated and the WISP sets up and waits for a communication interpret which indicates the beginning of an EPC packet. In the communication layer, the WISP processes the incoming data, executes the EPC Gen 2 protocol, and transmits its response. While not shown in figure 4.7, the communication layer often reports the same data twice to increase communication reliability.

4.3.2 Communication and Application Layers

A considerable challenge when programming the MSP430 involves meeting the timing constraints of the EPC protocol while still maintaining a low clock frequency. RFID tags that have custom state machines are designed at the hardware level to receive and send data using the EPC protocol. The general-purpose MSP430 must be carefully tuned to perform

EPC communication, both for receiving and transmitting data. In particular, a mix of C and assembly language is used where the C code maintains ease of configurability for the firmware for different sensor applications, and the assembly code allows fine-grained control of the timing of the MSP430 for EPC communication.

As previously described, the demodulator envelops and thresholds the Phase-Reversed Amplitude Shift Keyed (PR-ASK) signal from the reader into a serial data stream representing the data bits 1 and 0 as long and short pulses, respectively. To interpret data from the reader, the MSP430 uses the periodic edge of the waveform as a hardware interrupt, and then during the interrupt service routine re-samples the bit line to detect a 1 or 0 during the differentiated part of the waveform. This data is quickly shifted into memory before repeating this process. To detect the end of a transmission, a timer is refreshed during each bit. When bits are no longer received the timer expires, the packet is interpreted and, if appropriate, a response is sent to the reader. A detailed description of how the WISP uses and implements the EPC specification is described in section 4.5.

Figure 4.3 shows a set of EPC queries and responses along with the charge/discharge cycle of the WISP. Since the operating voltage range of the WISP occurs between 1.9 V - 1.8 V the rectified voltage appears to be nearly constant. In actuality, the WISP enters active mode at 1.9 V, consumes the energy in the storage capacitor until approximately 1.8 V, then enters a sleep state and harvests power until 1.9 V is reached. This duty cycling can be seen in the packet transmitted plot. Here, the WISP does not respond to every packet sent by the reader, instead it spends most of its time in a sleep state.

Performing application level tasks, such as sensor measurement, is generally done in tight conjunction with the EPC protocol. In this scenario, the completion of a receive/transmit cycle triggers the application layer to immediately take a sensor measurement; generate the desired EPC packet; and setup for a Query. This protocol centric approach works well for sensor driven applications where data is requested from the RFID tag at regular intervals. However, applications which leverage the wirelessly powered computing capability of the WISP benefit from a loose coupling with the communication layer.

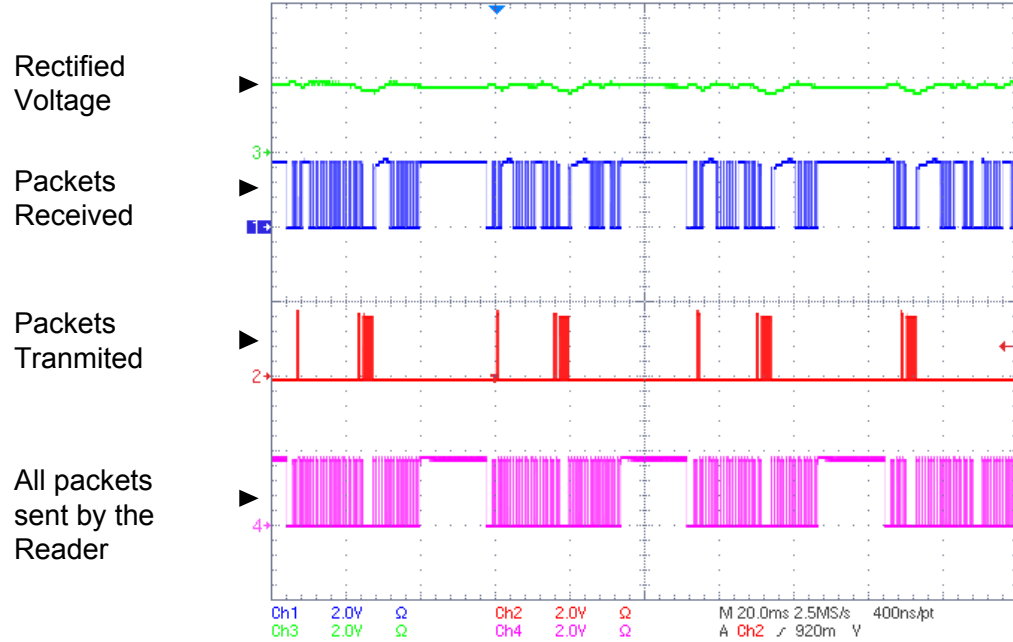


Figure 4.8: Oscilloscope plot of the WISP responding to EPC queries along with its rectified voltage.

4.4 Power Budget

One of the significant challenges of incorporating microcontrollers, sensors, and peripherals into passive RFID technology is the ability to manage the large power consumption of these devices. For example, the MSP430F1232 running at 3 MHz consumes approximately 470 μ A at 1.8 V. The resulting power consumption is significantly larger than typical passive RFID tags. Under these conditions the harvester cannot continuously supply power to the WISP during a single reader query.

One method to overcome this challenge is to use a large storage capacitor (on the order of ten microfarads) to accumulate charge over multiple EPC queries. Once sufficient voltage is obtained, the WISP can operate in a burst mode, polling sensors and communicating with the RFID reader. This approach of duty cycling is often used in low power applications; however, this presents a challenge for RFID networks when the WISP is not necessarily able to respond to each reader query.

The next section examines the issues related to powering the WISP from three perspectives: first is the received RF power required to turn on the device, the second is the operating duty cycle based on input power, and the last is the energy needed in the storage capacitor for active operation of the microcontroller and additional sensors.

4.4.1 Turn On Power Requirement

In the presence of the RFID reader, the WISP's RF rectifier will charge the storage capacitor until the power input to the device equals the power lost due to quiescent current.

$$P_{in} = P_{loss} \equiv V_{rectified} * I_{loss} \quad (4.1)$$

Thus, a key parameter for maximizing the read distance of WISP is minimizing the quiescent current consumption so that the minimum turn on voltage of 1.9V (supervisor threshold) can be rectified with the lowest possible input power. In order to characterize the system, a network analyzer was used to inject a continuous 915 MHz waveform into the antenna ports of the WISP. Figure 4.9 shows the resulting plot of rectified voltage and output power vs. input power when the WISP is in sleep mode. Rectified voltage was measured with the WISP in sleep mode (only quiescent current draw), and shows the minimum input power needed to start operation. After the 1.9 V supervisor threshold has been met, the rectified voltage continues to increase with input power, until the over-voltage protection diode activates at 5.4 V. In the actual implementation of the WISP, the MPS430 activates at 1.9 V and starts consuming power. Thus, the rectified voltage never rises above the supervisor threshold. Using the minimum input power needed for activation from figure 4.9, the expected operating distance for the WISP can be calculated with the logarithmic form of the Friis equation (4.1) for path loss, with a term for polarization loss included.

$$P_R = P_T - 20 \log \left(\frac{4\pi d}{\lambda} \right) + G_T + G_R - L_P \quad (4.2)$$

The transmit power of the reader $P_T = 30$ dBm (which is equivalent to 1 Watt). Its center frequency is 915 MHz, corresponding to wavelength $\lambda = 0.33$ m. The transmit antenna gain $G_T = 6$ dBi (this yields an effective isotropic radiated power of 4 WEIRP, the

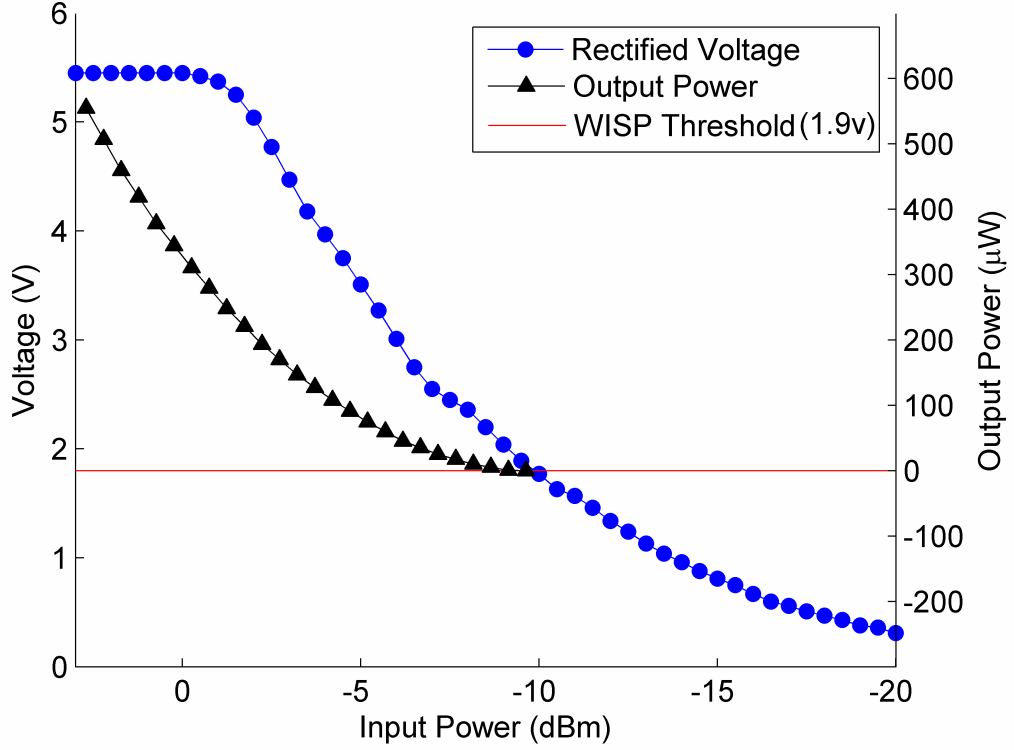


Figure 4.9: Rectified voltage (left scale) and output power at 1.9V (right scale) are plotted versus input power measurements using multi-meter and network analyzer for RF signal insertion into the antenna ports.

United States regulatory limit for this ISM band). The receive antenna gain $G_R = 2$ dBi (the standard gain figure for a dipole antenna), and the polarization loss $L_P = 3$ dB. Lossed L_P occurs because only half of the power transmitted from the circularly-polarized transmit antenna is received by the linearly-polarized receive dipole antenna. Using the operating thresholds of -9.5 dBm from figure 4.9, equation (4.2) predicts a maximum operational range of 4.3 m.

4.4.2 Duty Cycle

While rectified voltage (rather than power) determines the maximum achievable range, the operational duty cycle (percentage of the time WISP can be active), is determined by the

amount of rectified power. In practice, the rectified voltage will typically remain near the threshold voltage (1.9 V). This is due to the operation of the supervisor, which transitions the WISP from sleep to active mode, resulting in the consumption of power whenever the stored voltage exceeds this operating point. Therefore, it is important to characterize the output power of the harvester at 1.9 V. Figure 4.9 shows the result of output power versus input power at 1.9 V. This is accomplished by fixing the output voltage at 1.9 V using a power supply and measuring the amount of current that is supplied by the WISP. Then, the duty cycle of WISP (percentage of the time in active mode) is estimated as the ratio of rectifier output power to WISP active power consumption.

$$\frac{P_{out}}{P_{active}} = \frac{T_{on}}{T_{on} + T_{sleep}} = DutyCycle \quad (4.3)$$

In this equation, P_{out} is the output power of the WISP, P_{active} is the active power consumption, T_{on} is the time in active mode, and T_{sleep} is the time in sleep mode. For example, the power rectified at 0 dBm (310 μ W) divided by the active power consumption (1.8 V * 600 μ A = 1.12 mW) yields a duty cycle of 27%.

4.4.3 Active Energy Consumption

Since the rectifier cannot supply enough power for continuous operation, it is important to quantify the amount of energy that needs to be stored in order to power the WISP during active periods. During one EPC Gen 2 communication cycle, the complete WISP (not just the microcontroller) consumes on average 600 μ A * 1.8 V = 1.08 mW. A single query takes 2 ms including reader and tag communication. Using the expression for the energy stored in a capacitor ($E = \frac{1}{2}CV^2$, with C=10 μ F), the amount of voltage headroom needed above 1.8 V is 116 mV, resulting in a total minimum voltage threshold of 1.91 V for a complete packet transmission. It should be noted that the MSP430 will operate down to 1.7 V, even though this value is below the specified supply voltage. However, operation is not guaranteed; it has been observed that the Digitally Controlled Oscillator (DCO) can begin to slow down. Thus, it is not recommended that the designer rely on the extra 100 mV of headroom below 1.8 V. In the case of the previous example, the use of 16 mV out of specification headroom

(1.90 mV - 116 mV) has proven to give reliable results.

The same method for calculating the required stored energy can be used when selecting sensors for the WISP platform. Sensor tasks and packet generation are generally done prior to the EPC query. However, it is reasonable to assume that when performing sensor applications the MCU will exhibit similar current consumption. Inequality (4.4) expresses an energy feasibility condition for a particular sensor; the energy required to read the sensor must not exceed the usable stored energy. This expression can be used to calculate the capacitor size and voltage headroom required to operate a particular sensor, which in turn determines the range at which the sensor can be operated.

$$V_{dd} (I_s + I_w) T \leq \frac{1}{2} C (V_{rec}^2 - V_{dd}^2) \quad (4.4)$$

The current consumption for the sensor and WISP are I_s and I_w , respectively; C is the capacitance of the storage capacitor and T is the total time of active operation. The rectified voltage is V_{rec} and V_{dd} is the required operating voltage. Assuming that the sensor has the same voltage supply as the WISP, $V_{dd} = 1.8$ V. The left hand side of inequality (4.4) represents energy consumed by the sensor and WISP during one measurement. The right hand side represents usable stored energy above V_{dd} , the minimum operating voltage of WISP. Inequality (4.4) makes it clear that the limiting factor when selecting sensors is not only the current consumption (which determines power), but also the total required execution time of the sensor and WISP (energy, rather than power).

4.5 Communicating with the WISP

The EPC Class-1 Generation-2 protocol (henceforth referred to as Gen 2) was designed to rapidly identify tags with static IDs. However, when implementing sensing applications with the WISP, it is necessary to transmit and receive higher order data. The Gen 2 protocol provides several mechanisms that can be used to implement a two way communication layer. First, the WISP can send uplink data by overloading the identifier and by using Gen 2 Read command. Secondly, applications that need to transmit data to the WISP (e.g. to actuate its behavior), can use the Select command and the Write command.

4.5.1 Overloading the Identifier

The Gen 2 protocol efficiently reads tag identifiers, and by overloading the identifier to include sensor data, a collection of WISPs can also report data efficiently. In our initial applications, the identifier was replaced with the smaller tag identifier and the sensor data of interest. This approach breaks the semantics of the protocol and limits the interoperability of WISPs and standard tags.

The Gen 2 specification allows for the transmission of up to 496 bits of identifier, while current tags generally have an identifier of only 96 bits. Hence, up to 400 bits of sensor data can be piggybacked along with the ID, enabling data from different devices to be differentiated while at least partially maintaining the original semantics. Unfortunately, by sending sensor data along with the identifier the read time per tag is increased and the time required to read data from a particular tag can be prohibitively high. For many sensing applications, particularly those that use a large number of devices, reading all sensor data from every tag will be undesirable and overloading the identifier may be insufficient to meet the application requirements.

4.5.2 EPC Gen 2 Read Command

After singulating a tag, the reader can issue a series of Read commands to read the contents of tag memory, with each command eliciting up to 512 bytes of data. Before issuing a Read command, the reader requests a temporary, random 16 bit handle from the tag. This handle is used in the Read command to address the tag, and an arbitrary number of Read operations can be issued in sequence. Using this mechanism, a reader can selectively read sensor data stored in the user memory of a single WISP.

Using the Read command to gather sensor data has drawbacks with respect to efficiency and flexibility. First, to read new data from a WISP the device must again be singulated and a new handle must be obtained. With a large number of tags, singulation is time intensive. Even in the best case, where a single device is selected with the Select command, the singulation process must still be conducted, albeit with only a single tag responding and a new handle must be obtained; only then can data be read from the WISP. This results in

a large amount of the WISP's active time being spent on protocol overhead. Additionally, the identifier of the device with the desired data must be known prior to the read event, along with detailed knowledge of the memory layout with respect to sensor data location.

By overloading the identifier or using the Read command, basic sensing applications can be implemented using the WISP. However, when deciding which technique to use, the energy cost must also be considered. Specifically, using the Read command consumes more energy than returning the data with the ID. This presents a trade-off between range and speed, with the proper balance being largely application specific.

4.5.3 EPC Gen 2 Select Command

The Select command is intended to limit the number of tags that respond in a Query round. For example, a collection of retail items may have identifiers that indicate their model number and the Select command can be used to inventory only items of a given model by providing a memory pointer and bitmask which matches only that model. However, this mechanism can be repurposed to function as a general purpose broadcast channel, with the pointer and mask being interpreted by the WISP software as opcodes and data. As an example, we have implemented software for the WISP which interprets Select commands as instructions to blink LEDs.

4.5.4 EPC Gen 2 Write Command

Along with the general purpose broadcast facility of the Select command, the Gen 2 Write command can be used for unicast down-link communication. After a tag is singulated, the reader can write arbitrary memory locations on the tag in 2 byte words. Additionally, the BlockWrite command can be used to write up to 256 words at a time. This mechanism can be used to transfer data to the WISP. For example, to store location information on the tag as it moves through a supply chain. Additionally, a WISP could be programmed to look to certain memory locations for parameters that affect its operation. For example, to modify the sampling rate of the WISP, the Write command could be used to transmit the desired rate to a known memory location and the WISP would refer to this value when setting its

sampling rate.

4.6 Experimental Results

Figure 4.10 shows experimental results of the WISP performance: rectified output voltage, tag responses per reader query, and the rate of tag-to-reader packet errors are plotted vs. received power (dBm). The experimental set up consisted of an EPC Gen 1 RFID reader driving a 6 dBi circularly-polarized patch antenna. The readers antenna and WISP were placed one meter apart and one meter above the ground to minimize multipath effects. An adjustable attenuator inserted between the reader and its antenna was used to vary the power transmitted to the WISP.

Finally, equation (4.2) is used to calculate the path loss over the one meter separation between the WISP and RFID reader. Thus, the WISP received power is defined as reader transmit power (1 Watt), minus variable attenuator, minus transmission path loss. It should be noted that the 1 watt source represents peak output power of the RFID reader, while the average output power (not considered here) is highly dependent on reader transmission rate and the specific implementation of the EPC Gen 2 protocol.

To measure rectified Output Voltage, the WISP is placed in its low power state and voltage is averaged over a ten second interval using an oscilloscope. This is necessary to account for the variation in output power as the reader implements the EPC protocol. The resulting plot shows the WISP turns on with a peak received power level of -5.9 dBm, which is significantly more than the average power level of -9.5 dBm measured with the network analyzer in figure 4.10. In order to verify that this difference in turn-on threshold is caused by lower average power in the experimental setup, the RFID reader was replaced with a 915MHz, 1 W continuous wave source and the turn on power was found to be -8.7 dBm. The 0.8 dBm difference between the continuous source and the network analyzer is thought to be due to impedance mismatch between the dipole and the analog front end of the WISP as well as antenna non-idealities. The 2.8 dBm difference between the continuous source and the RFID reader is then due to lower average power output by the reader.

The plot of tag Responses per Query shows the number of successful tag responses received by the reader normalized over the total number of queries made. This is equivalent

to the operating duty cycle of the WISP and, as expected, is proportional to received power. The response rate drops to zero at -7 dB because there is insufficient voltage for operation. At 0 dBm input power, section 4.4 predicted an operational duty cycle of 27% using equation (4.1), which is close to the experimental value of 25% from figure 4.10. The reason that duty cycle (unlike turn-on voltage) is not diminished by the lower average power of the RFID reader is because duty cycle is normalized to the query rate of the reader. In other words, Responses per Query excludes times in which the reader is not transmitting.

The Uplink Packet Error represents the percent of query responses made by the tag that are not correctly received by the RFID reader. Due to the limited data interface with the RFID reader selected for the experiment, the number of reader rejected uplink packets is not directly available. To collect this data, the WISP counts the number of query responses it has made and reports the current tally as data encoded in each uplink packet. When the RFID reader application software receives gaps in the running tag response tally an error is recorded. Figure 4.10 shows that as received power decreases to the point at which sufficient voltage can no longer be rectified for operation, the uplink packet error rate increases. It is theorized that this system instability is due to the brown out state of the MPS430, along with the ring oscillator, used as the system clock, becoming detuned as the 1.8 V regulator drops out.

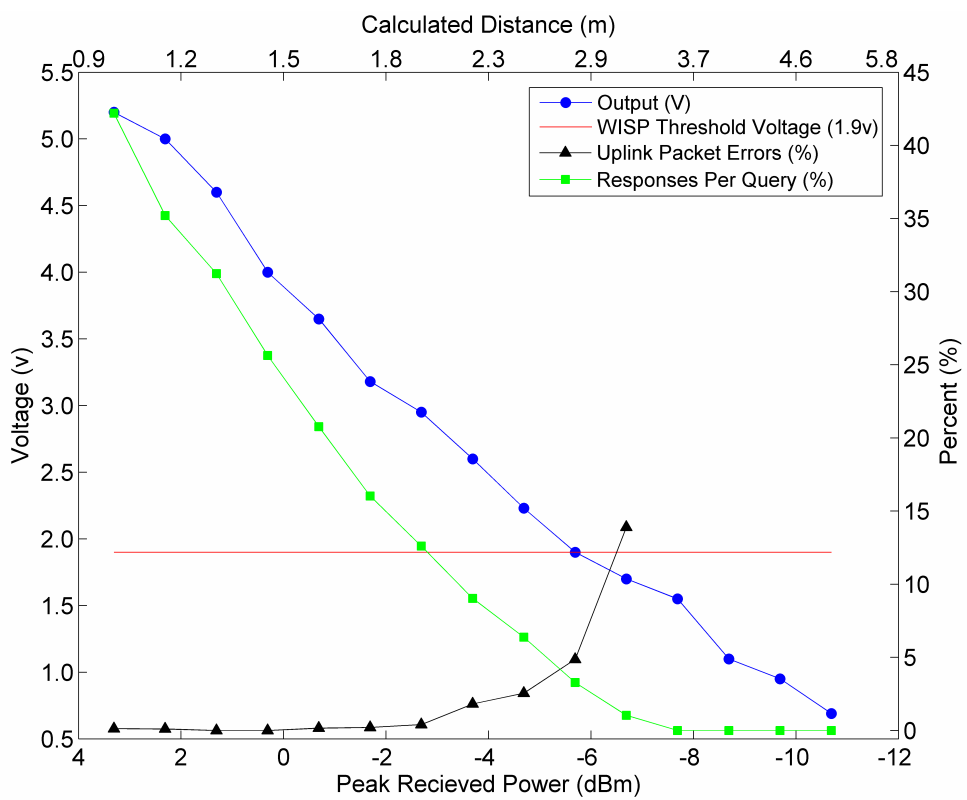


Figure 4.10: WISP performance: harvested voltage, Uplink Packet Errors, and Responses per Query as a function of input power.

Chapter 5

PHOTOVOLTAIC ENHANCED UHF RFID TAG ANTENNAS

The most significant barrier to improving passive RFID tag performance for both fixed function ID tags and enhanced RFID tags is the limitation on the amount of power that can be harvested for operation. This paper presents a novel approach for incorporating solar harvesting capability into existing passive RFID tags without increasing the parts count or changing the tag assembly process. This approach employs the tags antenna as a dual function element in which the antenna simultaneously harvests RF energy; communicates with the RFID reader; and harvests solar energy for auxiliary power. This is accomplished by using low cost, printable photovoltaics deposited on flexible substrate to form part of the antennas radiating structure. Several prototype UHF RFID antennas are demonstrated using commercially available thin film, amorphous silicon solar cells. To quantify the improvement in tag performance, WISP was used as an initial test vehicle. The effective read range of the tag was increased by six times and exceeded the readers sensitivity limitations. Additionally, the new antenna allowed for sensing and computing operations to take place independent of the RFID reader under typical office lighting conditions.

5.1 Motivation

Development in Radio Frequency Identification (RFID) technology has produced battery-free RFID tags, capable of wirelessly reporting a unique ID over a distance of several meters while being exclusively powered by harvested RF energy. Although the functionality of these commercial RFID tags is extremely limited, today's tags are essentially a wireless micro-computing platform, with an RF transceiver and a nearly unlimited lifetime. Several research efforts are pushing passive RFID beyond simple barcode replacement and are exploring the broader space of wirelessly powered devices. These enhanced RFID tags transcend the rigid EPC classification structure, providing sensing, arbitrary computing, data

logging, user interfacing, and actuation functionality, all while being powered wirelessly by the RFID reader [9, 12, 35, 54, 56, 66]. As future applications demand greater RFID tag functionality and increased operating range, the amount of harvestable power will become an even more critical design constraint.

The reliance of RFID tags on power transmitted from RFID readers creates two significant limitations. First, the operational region of a tag is limited to the physical zone covered by the RFID reader. Tags outside the zone are left un-powered. This means that, in order to increase the space over which the tag can operate, it is necessary to increase the number of RFID readers and reader antennas to cover the larger space. This can be cost prohibitive and requires significant effort to effectively instrument an environment. Thus, most RFID applications are limited to a specific, well defined work space, or the RFID tags are only read (i.e. powered on) at gateways or portals for tracking purposes. Important applications like logging of sensor data during shipping do not appear to be practical using only reader power, as the infrastructure necessary to instrument such a large area with readers would be prohibitively expensive. The second limitation resulting from reliance on reader power is that from the tags perspective, available power varies unpredictably as the tag is moved throughout the readers coverage zone. This is particularly limiting for enhanced RFID tags, where different tasks such as sensing, computing, storing data, and communication require different amounts of power. Therefore, it is desirable to utilize additional energy sources to increase the functionality, read range, reliability, and read rate of RFID tags.

There are a variety of energy sources that may be harnessed to power enhanced RFID tags, such as solar, thermal, mechanical vibration, or ambient RF energy. Harvestable energy from these sources varies from less than one μW to a few mW, depending on the technology and environment [47]. Initial work combining solar cells with RFID tags has shown promising results [14, 64]. However, these techniques are not compatible with traditional high volume RFID manufacturing techniques. Both solutions require a bulky and costly external crystal silicon solar cell, approximately the size of a small battery pack. Considering that the small size and low cost of RFID tags are the key features that enable their ubiquitous deployment, it is necessary that the enhancement of a tag with a photovoltaic power source not reduce the deployability of the device.

This paper presents a novel, dual purpose RFID tag antenna that simultaneously harvests RF energy, communicates with the RFID reader, and harvests solar energy for auxiliary power. The goal is to leverage modern printed photovoltaic manufacturing techniques, which produce thin, low-cost, flexible solar cells, and integrate them into printed RFID antennas. This work presents an initial prototype, which shows the feasibility of construction of a solar-enhanced antenna for an RFID IC. Additionally a WISP tag is augmented with a solar-enhanced antenna, yielding a 6x range improvement. Finally, reader-independent operation is explored using a solar-enhanced WISP under typical office lighting conditions.

5.2 System Overview

In order for a solar-enhanced RFID antenna to be successfully integrated into either fixed function ID or enhanced RFID tags, it is necessary that the replacement of the standard antenna with solar cells does not alter the manufacturability or usability of the device. Recent breakthroughs in printed electronics have allowed for low cost, printed solar cells that can be manufactured in high volume and in a roll-to-roll process [21]. Generally speaking, the manufacturing processes for solar cells are compatible with present day RFID antenna printing techniques, although there can be variations between manufacturers due to the type of application and the material properties. In both cases, metal traces for DC electrodes and antenna elements can be screen printed, applied with a material printer, or chemically deposited and etched. Solar material is typically applied as a thin film with a squeegee type application, screen printing process, or deposited with a material printer [21].

There are several examples of solar cells integrated with antennas. The authors in [22] present a GPS patch antenna that employs a poly crystalline solar cell patterned on the patch element. Additionally, solar-enhanced slot antennas are presented in [33,58,62], which utilize amorphous silicon cells on a flexible substrate. These efforts focus on the advantages of a fully integrated design, which reduces size and weight, while maximizing surface area for solar harvesting. However, the amount of power gained by reusing the relatively small surface area of the antenna for power harvesting does not significantly improve the power budgets for the proposed applications, which include satellites, GPS for motor vehicles, and battery powered consumer electronics.

The opposite is true for RFID tags, where the power that can be harvested by photovoltaics covering the RFID labels surface area is sufficient to completely power the tag. As an example, PowerFilm, Inc. manufactures flexible, thin-film solar cells that produce 2-4 mW/cm² under full sunlight. This means that even under low lighting conditions, where only a fraction of this power is available, there will be ample power for RFID ICs. Typically RFID tags consume between 10 μ W to 100 μ W of power.

Figure 5.1 shows a conceptual diagram of a solar-enhanced RFID tag. The antenna can be printed onto standard, flexible substrates, with the antenna electrodes themselves printed in copper or silver. The key attribute of this design is that the solar cell is part of the radiating structure of the antenna. This has the advantage of keeping the overall surface area of the final label consistent with current standard label designs as well as reducing material costs. In order to optimize the benefits of the solar antenna, the solar panels area and number of cells must be selected based on the requirements of the application and the particular RFID IC used.

The top image in figure 5.1 shows an exaggerated side view of a typical amorphous silicon solar cell unit. Since the individual cells are connected in series to produce the desired output voltage, the positive and negative electrodes of each cell are interleaved, creating a highly capacitive interface. One might assume that the PN junction of the solar cell would rectify the RF signal. However, at UHF frequencies, the RF energy takes the low impedance capacitive path between electrodes. The result being the AC equivalent model shown below the side view in figure 5.1. Since the capacitance of the junctions is effectively very large, the cell performs very similarly to a uniform metal sheet at UHF frequencies.

In order to use the solar energy harvested by the hybrid antenna, the RFID tag must be able to accept DC power as well as RF signals. To achieve this, the IC will need to be modified to expose the un-regulated power supply node, which is typically the rectifier output. Considering that many commercial RFID tags are four pin devices providing two ground connections, it is reasonable to repurpose one of the redundant ground pins for DC input. This is highlighted in the “strap detail” in figure 5.1. The last major design challenge is to ensure proper isolation between the DC power input and the RF signal so that RF noise does not compromise the performance of the IC. We propose using a thin metal trace

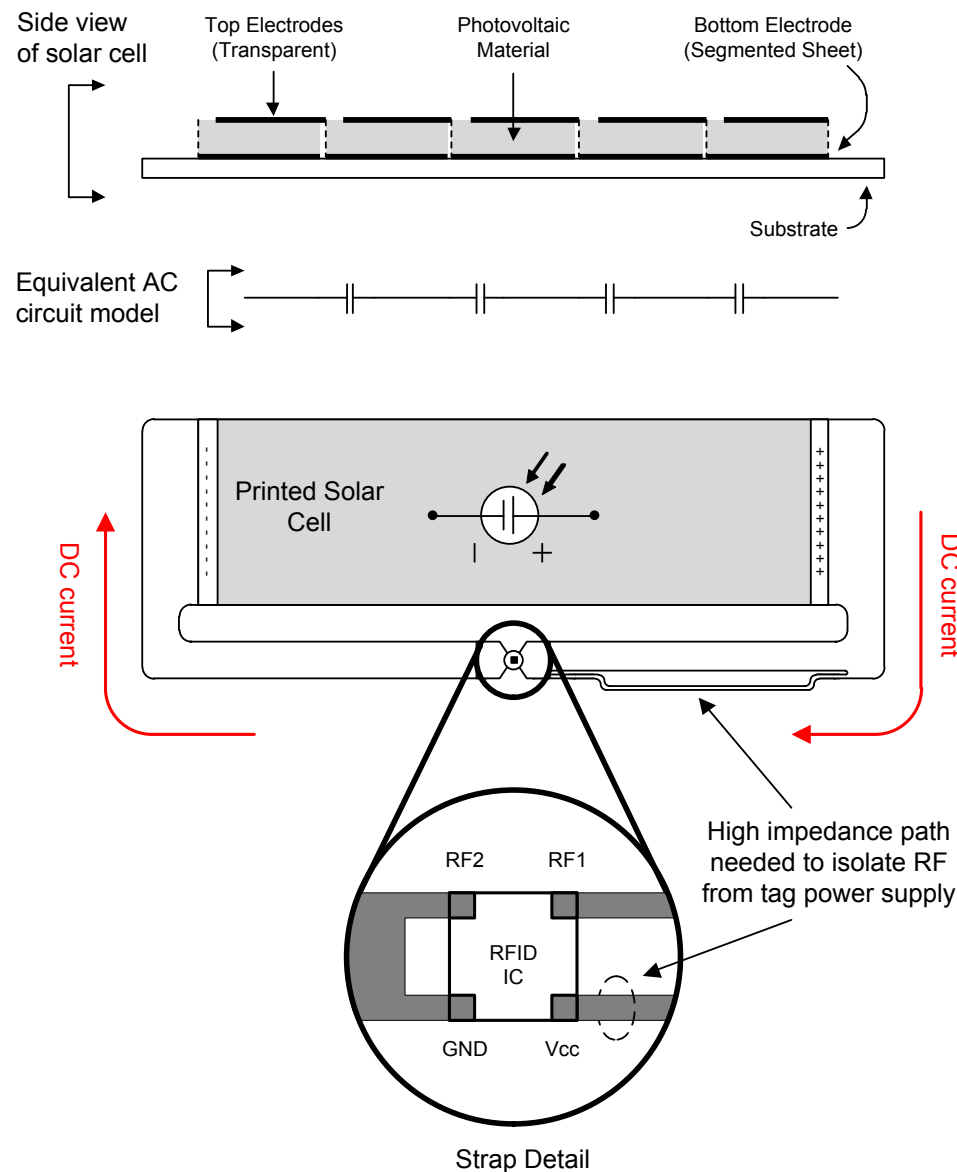


Figure 5.1: Conceptual diagram of a solar-enhanced RFID tag antenna with RFID IC. VCC is connected to the positive bus of the solar cell via a high-impedance trace. RF2 and Ground are connected to the same port of the antenna, and RF1 is connected opposite them.

that presents a high impedance path to the RF signal while allowing DC power to pass through to the IC.

5.3 Two Solar-Enhanced RFID Antenna Designs

The following sections describe the design and performance of two distinct solar-enhanced antennas. The first antenna presented is designed specifically for an RFID IC, and is intended to show the viability of constructing a low cost, size reduced antenna with integrated solar cells. Unfortunately, to date, there are no commercially available RFID ICs that expose the internal, unregulated power supply node. Thus, this first photovoltaic-enhanced antenna will only be able to demonstrate the RF antenna performance and not the impact that increased power will have on tag performance.

The second antenna design presented aims to show the benefit of increased available power provided by a photovoltaic-enhanced tag antenna on system performance using Intel Labs open-source WISP 4.1 platform [54]. The WISP is a fully passive (battery free) PCB RFID tag, and has the unregulated power supply pin exposed so that the tag's power source may be augmented. Although the WISP has many similar attributes to conventional RFID devices, it is not a direct stand-in for a commercial IC tag. Notably, the read range is less than half that of a commercial RFID tag, and the input impedance of the WISP is very different than an IC tag, and thus requires a different antenna design.

It is hoped that by validating the RF performance of the IC-specific solar antenna design, and by presenting the performance benefits of a solar antenna with the WISP, the viability of a complete system consisting of a photovoltaic enhanced antenna plus a custom RFID IC with exposed unregulated power pin can be concluded.

5.3.1 Prototype Solar Antenna Design for RFID ICs

Figure 5.2 illustrates the proposed IC-specific solar antenna design. The operation of the antenna can be viewed as a monopole mirrored over the solar cell, which is acting as a ground plane. An inductive strap is added to provide the necessary reactance to conjugate match to the capacitive RFID IC. The vertical section of the antenna arm (shown with

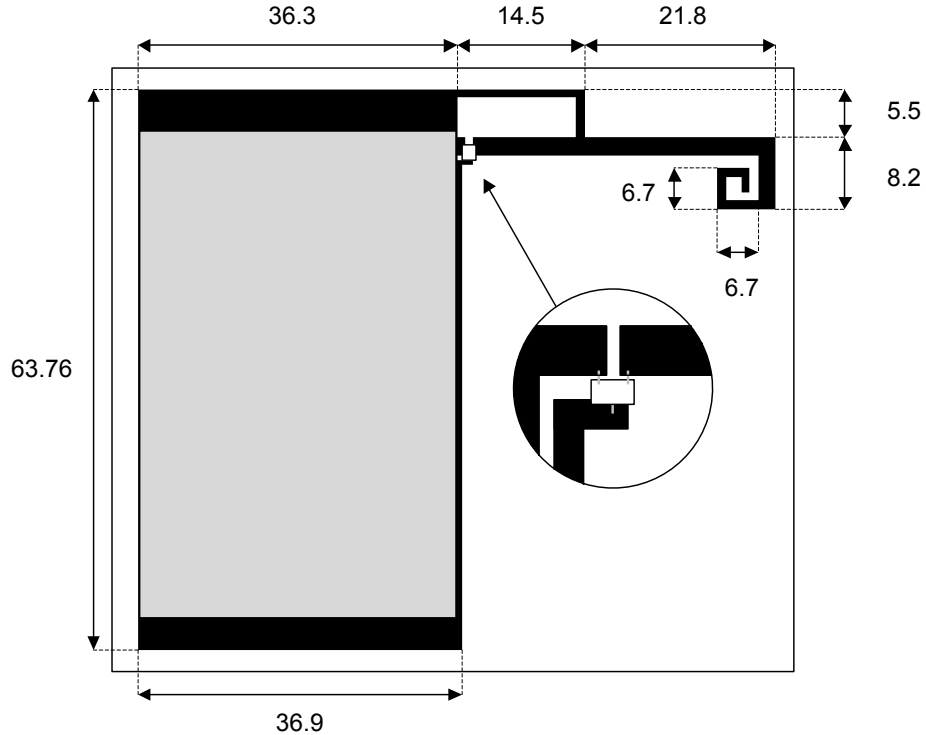


Figure 5.2: Diagram of the photovoltaic-enhanced antenna for an RFID IC. Solid black lines denote copper traces. The gray section represents the solar cell. A small, thin trace connects the positive terminal (bottom) of the solar cell to the IC, providing DC power. Lengths are given in mm, and trace widths are 1mm and 2mm.

length 8.2 mm) can be varied to tune the resonant frequency of the antenna. The small spiral on the end of the antenna enables additional fine tuning of reactance.

In order to draw power from the solar cell, the DC bus bars located at the two ends of the cell need to be connected to the IC. To accomplish this, the antenna's arm was relocated to the top of the cell and connected to the negative terminal of the solar cell. This allows the inductive strap and the GND pin of the tag to be at the same DC voltage potential. The positive terminal of the solar cell is located at the bottom and a thin trace is added to connect it to the IC. This can be seen in the detail pop out in figure 5.2 , where an RFID

IC with an extra terminal is shown connected to the antenna.

Figure 5.3 shows an image of the constructed photovoltaic-enhanced RFID antenna. The metal traces were cut with an automatic stencil cutter and mounted to a 1 mm thick Plexiglas backing for rigidity and testing purposes. The solar cell used in this prototype is the Powerfilm SP3-37 amorphous silicon solar cell. This particular solar cell is chosen because of its relatively small size, flexibility, and because it is produced through a low-cost roll-to-roll printing process. This low-cost manufacturing means that, in the future, the overall cost of large-scale production for the solar-enhanced antenna will be inexpensive and compatible with current RFID tag manufacturing processes. The prototype antenna is built on Plexiglas substrate for the purposes of this experiment, but in a real world application would likely be printed, along with the solar cell, onto a flexible substrate similar to current RFID tags. The SP3-37 solar cell has a peak output of 3.0 V at 22 mA under full sunlight (107,527 Lux) and an output of 2.5 V at 100 μ A under typical office lighting (330 Lux).

The Powerfilm solar cell was modified to expose the bus bars from the underside. It was then gently soldered to the copper traces of the antenna. Lastly, an Alien Higgs-3 SOT-323 packaged RFID IC was soldered to the antenna to complete the RFID tag. Again, the Higgs-3 tag is not able to use the DC power provided by the solar cell because the appropriate net is not exposed. However, the completed device does represent a tag-compatible antenna design which can be used to verify the RF performance of the photovoltaic-enhanced antenna.

Simulation results show that the antenna has a maximum gain of 1.7 dBi and a radiation pattern typical of a dipole antenna. Considering the complexity of the solar panels construction and material characteristics, simulations were run using a simple all-copper model with identical dimensions. Because the simulation was simplified in this manner, it is important to show that the addition of the photovoltaic material does not significantly alter the RF performance of the antenna. Figure 5.4 shows plots of the simulated input impedance, the measured input impedance of a copper-only version, and the measured input impedance of the full photovoltaic-enhanced antenna as shown in figure 5.3. The impedance plots show that the solar antennas reactance is slightly lower than that of the all-copper version, a difference small enough to be easily compensated for in future design cycles. Essentially, these results indicate that the solar panel is acting as a conductor at UHF frequencies.

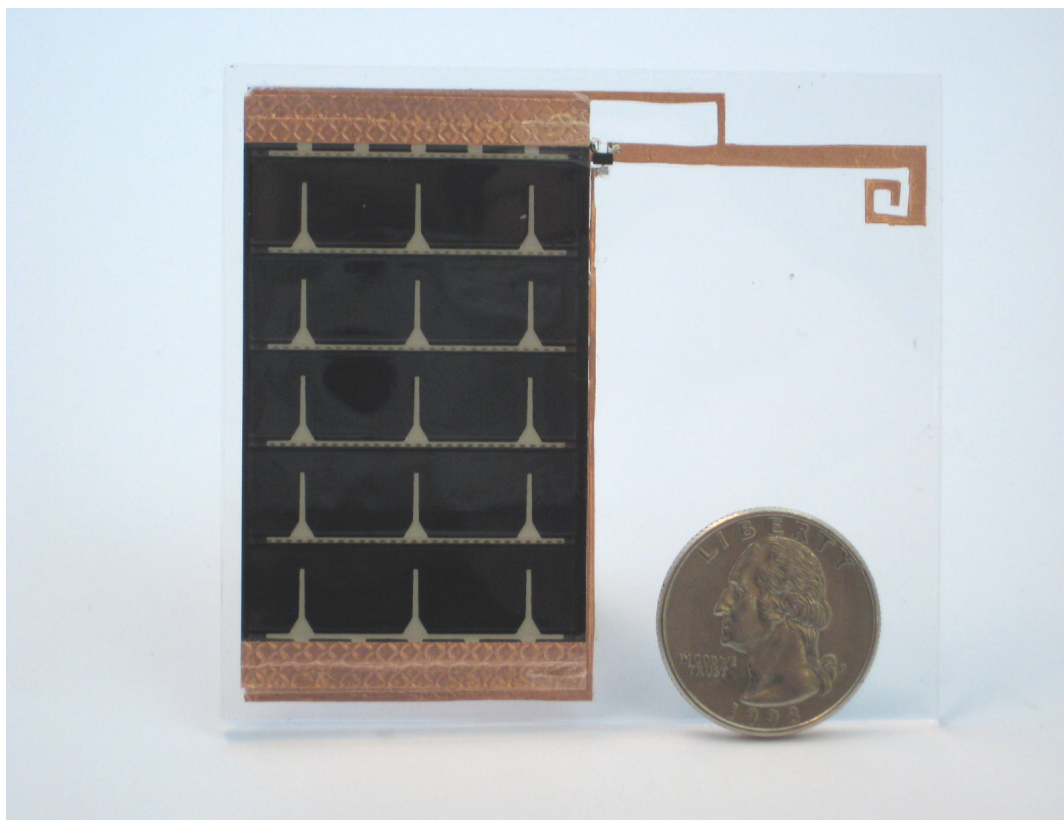


Figure 5.3: Image of the photovoltaic-enhanced RFID antenna connected to an Alien Higgs-3 SOT-323 packaged RFID IC. The solar cell is manufactured by PowerFilm Inc. part number #SP3-37. The completed tag prototype has been mounted to a 1mm thick layer of Plexiglas for rigidity. This tag shows the viability of incorporating photovoltaics into RFID antennas while maintaining RF performance.(For clarity, this IC does not accept solar power)

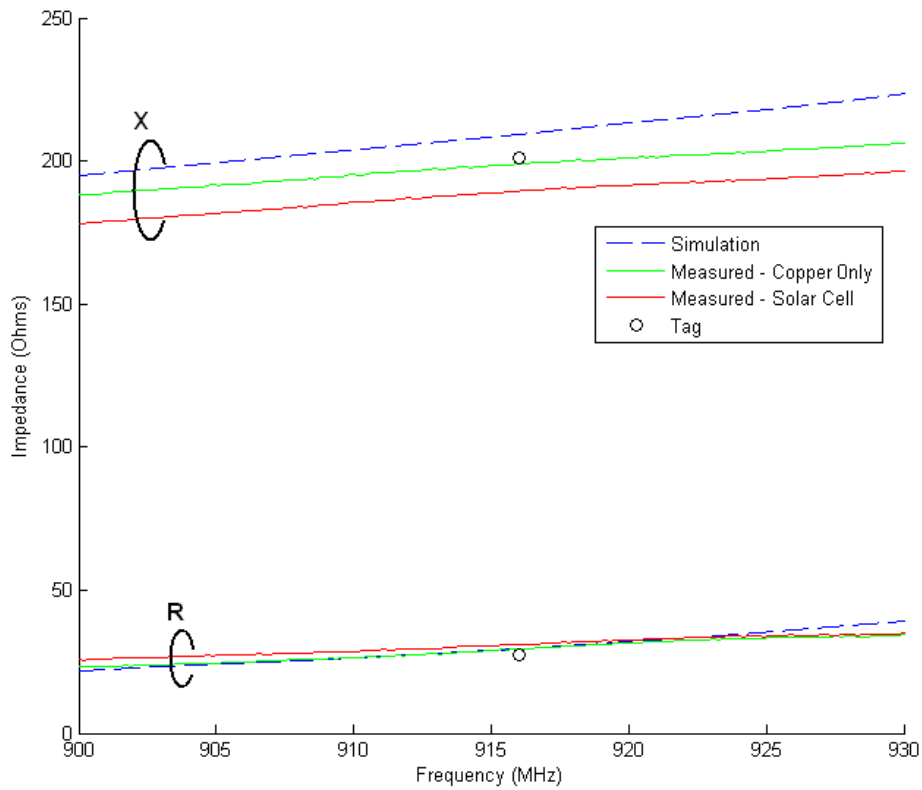


Figure 5.4: Simulated and measured input impedances for the IC specific solar antenna. The bottom group of traces shows the real impedance and the top group shows the complex. Measurements show a small deviation between the copper version of the antenna and the antenna that incorporates the solar cell.

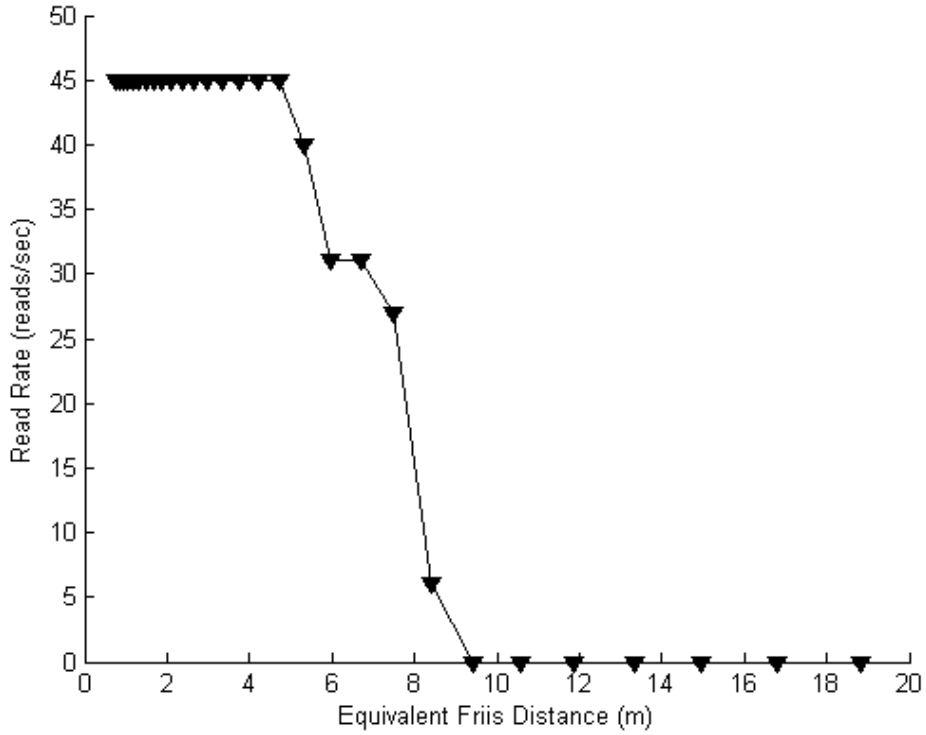


Figure 5.5: Read range of the prototype photovoltaic-enhanced RFID tag, using the Higgs-3 IC. Solar power was not used by the IC.

Next, the read range of the photovoltaic-enhanced antenna plus Higgs IC was tested for read range. In order to reduce the effects of multipath interference, a variable RF attenuator was used to simulate changes in distance. The reader antenna and tag were placed 0.75 meters apart and both were placed one meter above the ground. Care was taken to minimize reflections in the immediate environment. Figure 5.5 shows a plot of the equivalent distance, calculated using the Friis equation, which was determined to be comparable to commercial tags. Measurements show that tag sensitivity is approximately 1 dB lower than predicted using the simulated antenna gain, and the IC manufacturers specified RF sensitivity. This is attributed to the small impedance mismatch seen in figure 5.4 and manufacturing variation of the antenna geometry.

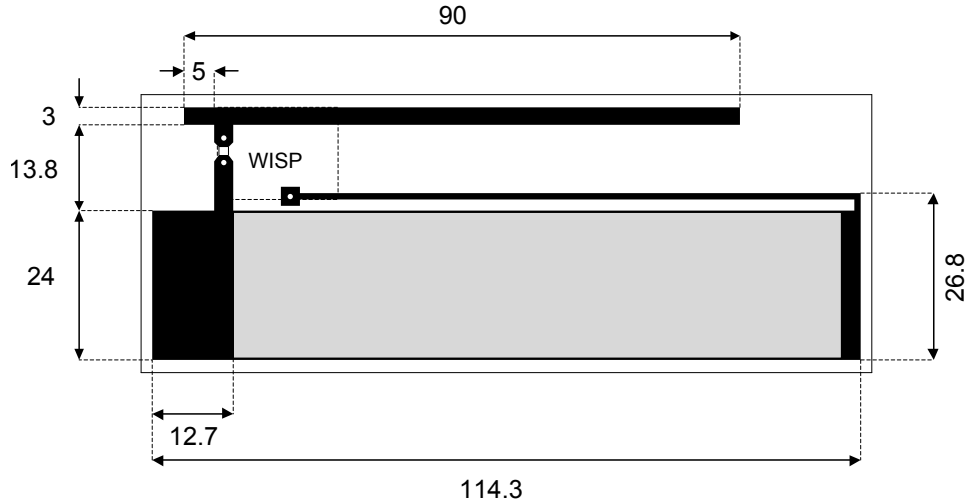


Figure 5.6: Solar-enhanced antenna design for WISP-based tag.

5.3.2 Solar WISP Antenna Design

In order to explore the performance gains of a complete photovoltaic-enhanced RFID tag that can use harvested solar power, a second antenna, intended for use with the WISP 4.1, has been prototyped. The antenna design, shown in figure 5.6, is a modified inverted F and connects to the WISP through vias in the antenna's substrate. This antenna, with attached WISP, is shown in figure 5.7.

A thin trace connects the positive bus of the solar cell to the unregulated power supply of the WISP to transfer the harvested solar power to the WISP. The DC trace is thin, so that it appears as a high-impedance port to the RF signal on the antenna and thus filters out the RF signal from the DC port. In the prototype design, a Schottky diode is added to the WISP to ensure that when the solar cell has a lower voltage than the unregulated power supply on the WISP, the WISP will not shunt harvested RF power into the solar cell.

The input impedance of this antenna is $40 + j150$ and can be easily matched to the WISP's rectifier using the discrete L-match network that is integrated into the WISP's analog-front-end. One common misconception is that the WISP requires a balun to convert

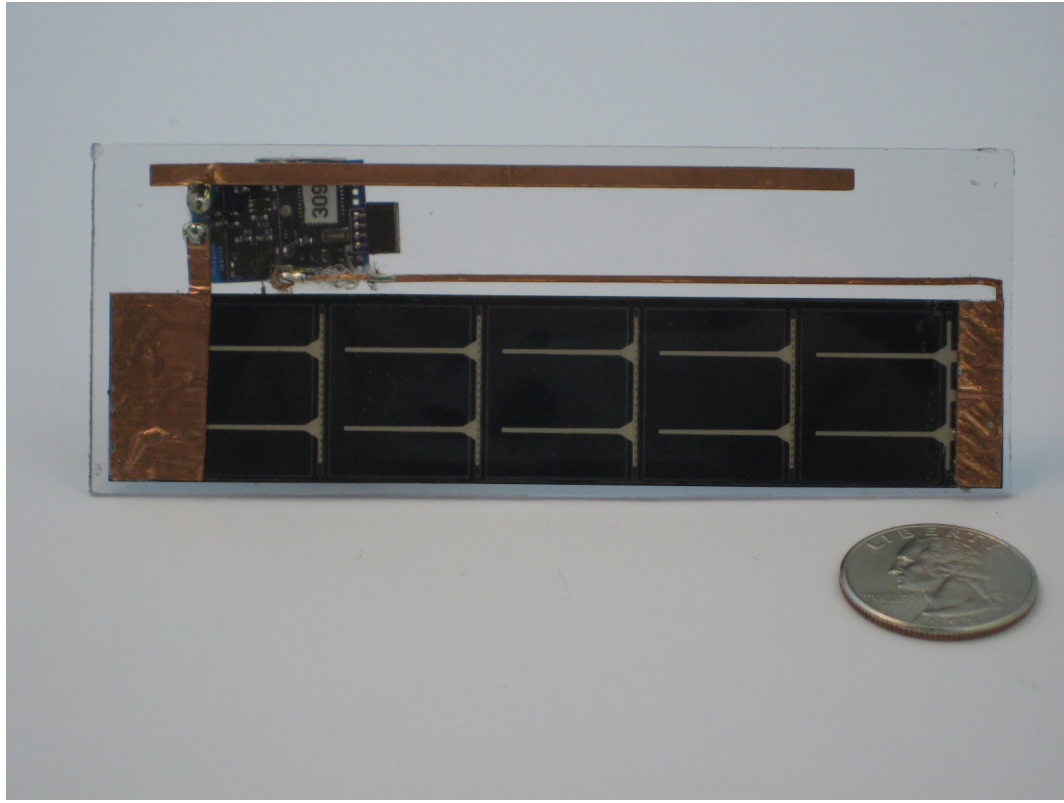


Figure 5.7: Inverted F antenna constructed from a solar cell and connected to the WISP.

the balanced antenna signal to the unbalanced analog-front-end. As is the case with most RFID tags; this step is not necessary and would cause undue loss of precious RF signal. The reasoning for the lack of a balun is that RFID tags have very low capacitive coupling to earth ground, thus their GND plane (or silicon substrate) can truly float with respect to earth ground. The same argument is true for the WISP. The only caveat is that the GND plane on the WISP is oscillating at 915 MHz, and therefore care must be taken when connecting probes and long wires.

5.3.3 Range improvement for Solar WISP

After characterizing the impact of replacing a standard copper antenna with a solar panel, the next step is to quantify the performance increase and additional benefits that the solar-enhanced antenna enables. Expected benefits of solar augmentation are an increase in read

rate and range, as well as the ability to perform functions such as computation and data logging while away from the reader.

Increasing the read range of RFID systems is an ongoing effort within the RFID community, as increased range allows for increased usability and a greater variety of applications. For instance, RFID sensor networks, which are composed of many tags with onboard sensing capabilities, could be made to communicate faster and operate over larger areas using solar-enhanced tags rather than purely RF-powered devices. The following experiment characterizes the read range improvements provided by the solar-enhanced antenna.

The solar antenna was conjugately matched to the RF front end of a WISP using an onboard discrete matching network. To quantify the range benefits of the solar antenna, the read rate of the attached WISP was measured as a function of simulated reader-to-tag distance under various lighting conditions and in the absence of light. In order to determine an upper limit for read range when available power is not a constraint, the solar antenna-based WISP was then externally powered using a battery and its performance measured.

The device was placed 0.75 m away from an RFID reader in a room that was made to have as little multi-path interference as possible. A variable RF attenuator was inserted between the reader antenna and an Impinj Speedway reader to serve as free-space loss for various tag distances. This attenuator was used instead of physically moving the tag in order to eliminate the effect of changes in multi-path interference patterns which would occur if the tag were moved. An incandescent light source was used to provide known lighting conditions for the solar-enhanced WISP, as measured by a Sper Scientific 840022 light meter. Lighting conditions for the solar-enhanced tag represent a variety of environments in which the tag might be used, and were each chosen to be near to minimum lighting requirements for those environments specified by the Occupational Safety and Health Administration.

The read rate of the solar-enhanced WISP was measured under four different lighting conditions at each of 31 attenuation levels, which simulate reader-to-tag distance. Figure 5.8 shows the resulting read rate vs. distance plot.

Using a 1-Watt transmitter, the solar antenna-based WISP with 150 lux of incident light was readable for up to 24 m. In contrast, the darkened solar antenna with less than 1 lux of incident light had a read range of only 4 m. However, as incident light intensity was

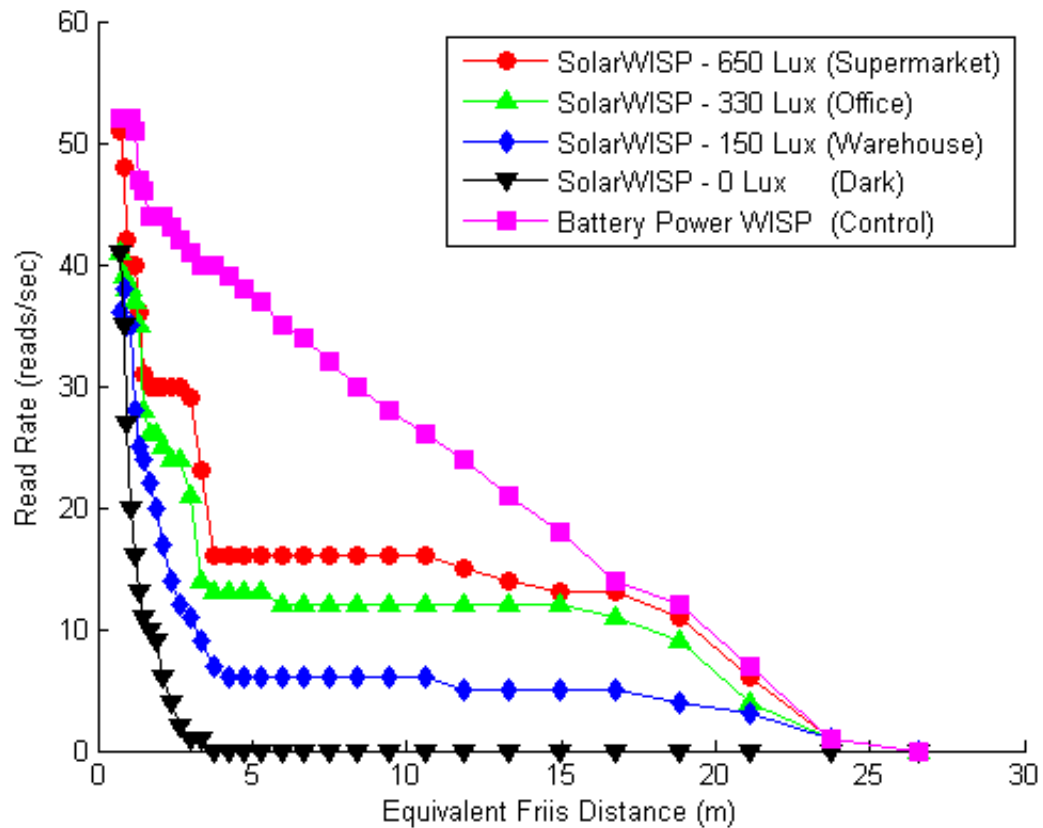


Figure 5.8: Read rate as a function of distance for WISP tags using the solar-enhanced antenna. Equivalent distance is calculated assuming a 1 Watt transmitter and a 6 dBi transmit antenna.

increased from 150 lux to 330 and then to 650, maximum read range did not significantly increase. Additionally, the battery-powered tag had a similar maximum read range to the solar powered devices. This near equivalence in range between each of the solar-powered tags and the externally supplied tag suggests that the determined maximum range in this experiment was limited by reader sensitivity, rather than by available power. A more sensitive reader could likely be used to further enhance the read range of these solar-augmented tags.

An interesting feature of the solar-augmented read rate plot is the sudden decrease in read rate as the simulated distance passes 4 m. This drop occurs at the point when the RF power provided by the reader is no longer sufficient to bias the harvesting circuit. At distances greater than 4 m the tags are entirely powered by the lit solar antenna, and so read rate becomes relatively constant with respect to reader-to-tag distance. Increasing the available power by increasing light intensity or adding an external supply significantly increases read rates for the solar-enhanced WISP, particularly at distances over 4 m where RF power is not a factor.

5.4 Reader Independent Operation

As well as increasing the RFID read range of a tag, the addition of a solar antenna allows the tag to become operational even when out of range of an RFID reader. This enables a solar antenna-based tag to perform sensing, data logging, computation, and other functions in any scenario where sufficient light is available. There are several foreseeable applications where it is desirable for a tag to perform sensing and data logging away from the reader. For instance, cold chain monitoring of food and pharmaceuticals could be improved through the use of data logging solar-enhanced tags, which could verify that products remained within a given temperature range throughout their processing and shipment. Sensitive equipment traveling across the country could also be augmented with temperature and orientation-logging tags which would enable shipping companies or the recipients of the shipment to determine what conditions the equipment had been exposed to during its journey. This experiment will explore the latter application by using a solar antenna-based WISP tag, shown in figure 5.9, to log a parcel's temperature and orientation throughout a simulated



Figure 5.9: Passive solar antenna-based data logger on a parcel.

shipment.

RFID tags have already found widespread application in shipping and parcel tracking. The use of a solar antenna-based enhanced-RFID tag could allow for important parameters of a parcels condition to be recorded throughout its entire route without the need for an RFID reader to accompany the tagged item and provide power to the tag. Arranging for RFID readers to be present in each stage of a shipment would be prohibitively expensive due to the cost of the reader, associated hardware, and infrastructure required. A cost-effective alternative which would allow for continuous data logging could be implemented with the simple addition of a light source to the inside of the shipping container or delivery vehicle, which would provide power for solar antenna-based data logging tags.

The solar antenna-based WISP is programmed such that, when ambient light conditions provide sufficient power, the device will take measurements from an onboard temperature sensor and 3-axis accelerometer and record these measurements to an EEPROM. The state

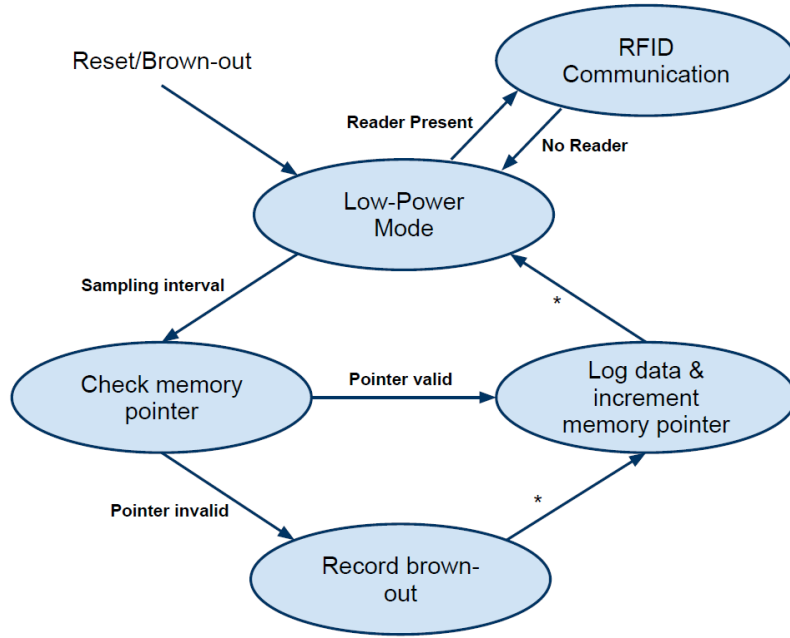


Figure 5.10: State diagram for solar-enhanced, data-logging WISP.

diagram in figure 5.10 provides an overview of the firmware design for the data-logging WISP. While out of range of the RFID reader, the device firmware puts the WISP into a low-power mode. In this state, the solar antenna charges a storage capacitor which provides power for the WISP’s microcontroller and various subsystems. Each second, a watch crystal-based timing circuit wakes the device, and data logging operations are performed. A 32.768 kHz watch crystal was chosen as the time base because it provides a high degree of accuracy with minimal power cost.

In the case where there is insufficient ambient light to support the timing circuit’s operation, the device will “brown out”, or lose power, and log the event. Any such loss of power recorded in the data log indicates that the tag has lost track of time, rendering timing information for the remainder of the data log inaccurate. This detection of brown-out events is accomplished by comparing a pointer value in the microcontroller’s volatile memory to a value in the non-volatile EEPROM. In normal operation, the two values should always be equal. If the two pointer values differ, it can be assumed that a brown-out reset event has

occurred.

When the device re-enters a reader's field and is queried by the reader, temperature and acceleration measurements recorded to the onboard EEPROM are sequentially transmitted to the reader. For simplicity, the data is transmitted as part of the tag's EPC, although in a real-world application the data would likely be sent in response to a read command.

In the simulated shipment, a parcel with the RFID data logger attached is carried around an office floor under typical lighting conditions, starting and ending within range of an RFID reader. Data is collected during the period when the tag is outside the reader's range. The plot in figure 5.11 contains the temperature, 3-axis acceleration, and brown-out events recorded by the tag. The tag is exposed to sufficient light for most of its trip, only experiencing a loss of power once at 215 seconds into the trip when it is placed in a darkened area. Several times during its travel, the parcel is placed on its side and the accelerometer detects an orientation change. To demonstrate temperature sensitivity, the parcel is heated under a lamp from the 50 to 100 second mark, then allowed to cool for the remainder of its trip.

Applications for such a solar antenna data logging device are constrained by power limitations. The light intensity necessary to perform data-logging operations will depend on such factors as the size and conversion efficiency of the solar antenna, the desired sampling interval, and the power requirements of the sensors and non-volatile memory used. Sensors and memory devices for this experimental setup were chosen for their low power requirements. An ultra low-power Texas Instruments MSP430 microcontroller implements the computation and control functions for the system, as well as the EPC Gen 2 RFID protocol. An 8 kB Microchip EEPROM provides non-volatile storage of logged data. Acceleration data is produced by an Analog Devices ADXL330 MEMS accelerometer.

Uses that require a high sensor sampling rate, or that require sensors to be continuously powered, will not likely be possible in such a system. For example, it would be difficult to use this device to measure the maximum acceleration experienced by a parcel, as this requires very fast sampling or continuous sensor operation. However, as sensing technologies advance and power requirements decrease, more and more applications will become possible with this system.

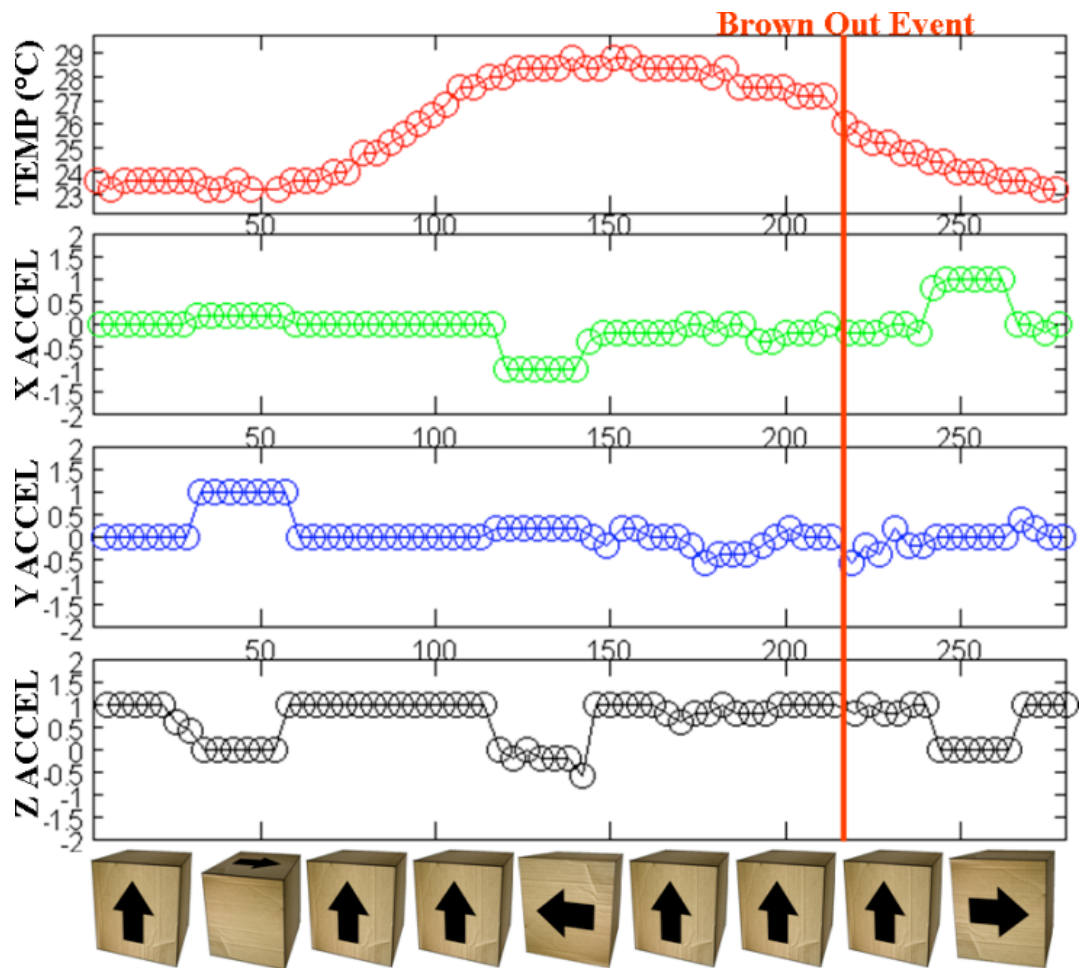


Figure 5.11: Temperature and orientation data recorded by the solar-enhanced RFID platform during a simulated parcel shipment.

Aside from power considerations, another concern which must be addressed before this system can be fully implemented is the amount of time required for the data logging RFID device to transmit its recorded history to the reader upon arrival at its destination. Procedures at the receiving station may need to be modified to allow the parcel-attached tag sufficient time to transmit all of its memory contents. To mitigate this issue, the tag could analyze the data during recording and identify important events, which it would then transmit first when within range of the reader. Power provided by the solar antenna allows for computation and data interpretation tasks such as this to take place on the tag itself, prior to encountering the reader.

5.5 Summary

This chapter has argued that the most challenging obstacle to improving passive RFID tag performance is the limited amount of power that can be rectified from the signal transmitted by the RFID reader. In order to augment this power supply, a novel, dual purpose RFID tag antenna that simultaneously harvests RF energy, communicates with the RFID reader, and harvests solar energy has been proposed.

A prototype of the solar-enhanced RFID antenna has been built and simulated in HFSS. Intel Labs WISP (an RFID development platform) was used to create and test a complete working prototype of a solar antenna-based RFID tag. The dual-harvesting antenna increased the effective read range of the tag by at least a factor of six under typical indoor office illumination conditions. In the same indoor lighting conditions, enough power was available to perform sensing and data logging, even while away from an RFID reader. The dual harvesting strategy presented here can enhance the read rate of RFID tags, provide increased power for more demanding workloads such as sensing and computation, and allow sensing, data logging, and computing operations away from RFID readers.

The tag architecture is compatible with low cost, high volume production processes. Since most existing UHF RFID tag ICs have 4 contacts (including two redundant ground pads), the hybrid solar-RF antennas presented here are compatible with existing RFID IC footprints. Photovoltaic harvesting materials can be printed using low-cost, high volume processes compatible with RFID manufacturing, and thus it should be possible to integrate

the photovoltaic and RFID manufacturing processes without extensive modification. The end result will be tags that are similar in cost to todays ordinary RFID tags, but with improved performance and additional capabilities enabled by the additional power source.

Chapter 6

A CAPACITIVE TOUCH INTERFACE FOR PASSIVE RFID TAGS

This chapter presents a novel method for incorporating a capacitive touch interface into existing passive RFID tag architectures without additional parts or changes to the manufacturing process. This approach employs the tag's antenna as a dual function element in which the antenna simultaneously acts as both a low-frequency capacitive fringing electric field sensor and also as an RF antenna. To demonstrate the feasibility of this approach, I have prototyped a passive UHF tag with capacitive sensing capability integrated into the antenna port using the WISP tag. Finally, I describe how this technology can be used for touch interfaces as well as other applications with the addition of a LED for user feedback.

6.1 Motivation

Current research efforts in Radio Frequency Identification (RFID) applications are exploiting the low-cost and unobtrusive form factor of RFID tags to serve as the glue between the real (physical) and virtual (electronically-represented) worlds. Traditional examples include the use of RFID tags for automatic electronic tracking of items in supply chains, payment for physical goods with electronically-represented money (vs. printed money), and physical building access with an electronic access card (vs. a physical key).

Recent non-conventional applications are applying the ubiquitous and pervasive nature of RFID to connect the physical and virtual world in new ways. Specifically, RFID is being used as a ubiquitous interface, embedded throughout the environment for data collection or to seamlessly call for services and information. Examples include the implementation of a living environment augmented with RFID to enhance the quality of life and independence of elderly citizens [49]. In this example, participants wear small mobile RFID reader bracelets that report interaction with tagged objects. Activities can be inferred from this data and reported to caregivers. In [51], tags function as symbols in an RFID-augmented environment

that represent actions and services available to the user; a cell phone enhanced with a mobile near-field RFID reader touches the tag to gain information or to activate a service.

These kinds of applications are based on a very simple binary model: the user's behavior determines whether the tag is inside or outside the interrogation field of the RFID reader. Enabling richer user-tag interactions by giving the user explicit control over how the tag is used and what information it sends has the potential to unlock new applications of RFID. Furthermore, it can potentially mitigate many of the current privacy and security issues relating to RFID used in passports, credit cards, and other RFID applications that involve personal data.

One can envision a simple scenario where the user touches an input on a passive UHF RFID tag, which communicates with a nearby RFID reader, in order to control a light switch. In this case the need for the individual to carry a mobile RFID reader in order to participate in an RFID-enhanced environment is not necessary. Alternatively a shopper purchasing items with a RFID enabled credit card could choose when to transmit his/her private data by touching an input on the card. This would thwart an attacker from wirelessly stealing passport or credit card information while the tag is in a mailing envelope, purse, or wallet; the tag must be touched to be enabled at the intended time of use.

The research presented here supports these types of new applications by allowing the user to interact directly with passive RFID tags via an embedded touch interface that does not change the tag's form factor or cost. Large scale passive tag production requires minimum cost per fully-assembled tag. Thus, a key challenge for incorporating new functionality into passive RFID tags is maintaining a cost-effective manufacturing process. Furthermore, the thin, unobtrusive label form factor of RFID tags is important in many applications. Sensing schemes that require no changes to the tag form factor or manufacturing processes therefore have significant practical advantages over less-integrated sensor tag schemes.

This chapter presents a technique for adding user touch sensing into a passive RFID tag in a fashion that is fully compatible with existing UHF tag form factors and manufacturing processes: the RFID antenna functions simultaneously as a capacitive touch sensor and UHF RFID antenna. The primary function of the antenna remains to provide power and communication for the tag. Additionally, the tag's circuitry uses the antenna's low frequency

self capacitance as an electric field touch or proximity sensor. When the user touches the input area on the tag's antenna, the RC time constant of the capacitance sensor is measured and a touch event is reported to the reader. The RFID tag user interface is further developed with the addition of an LED into the WISP platform for event notification or feedback.

In contrast, other methods for combining input devices with tags RFID tags are not compatible with existing processes. For example, there are a variety of prior examples of a push button or mechanical interface for RFID tags. The input devices in [28, 48] rely on the inclusion of a mechanical switch that couples the RFID chip to the antenna. Closing the mechanical switch enables the RFID chip to communicate with a reader. Present RFID assembly techniques rely on a flip-chip process where the IC's two or three antenna pads are directly bonded to the antenna using a conductive adhesive [19]. The inclusion of a third device, such as a switch, would not be compatible with this low-cost assembly technique, and would yield a much more expensive finished product.

The organization of this chapter is as follows: Section 6.2 describes the general design and operation principles of an RFID tag enhanced with a capacitive touch interface. Section 6.3 presents the implementation and performance of a UHF RFID tag with a capacitive touch input and an LED output for user feedback. Finally, applications are discussed in section 6.4 and a summary in section 6.5.

6.2 Passive RFID Capacitive Sensing Architecture

There are a variety of capacitive sensing methods that can be utilized to identify a touch event [35]. The simplest method relies on measuring the rate at which the sensing capacitor charges and discharges when different materials are placed within its electric fields. In related work the authors in [61] present an analysis of capacitive sensors made from conductive ink printed on paper, for use in interactive displays and print media. This sensor manufacturing method is directly applicable to RFID antenna construction which typically uses conductive ink printed on a plastic substrate.

In order to achieve a low-cost RFID touch interface, our proposed method relies on using the tag's antenna for power and communication while at the same time using it as a capacitive sensing element. The key is to take advantage of the frequency separation

between the RFID reader's carrier signal (HF or UHF bands) and the low frequency RC time constant of a capacitive sensor (DC to LF). By separating these two signals, the antenna will operate as a dual band device: the UHF signal only interacts with the radiating structures and the low frequency electric fields only interact with the capacitive sensing circuitry.

As an example of how an RFID antenna can form a capacitive sensing element, consider a simple dipole antenna. Inherently, at DC, the two halves of a dipole form a capacitor with energy stored in fringing electric fields. This capacitor can be charged by injecting a DC voltage across the two ports of the antenna. Even though the two halves of the antenna are at a different DC potential, the AC characteristics of the antenna are unchanged, and thus the dipole will continue to radiate energy (and through reciprocity receive energy).

Once charged, the voltage on the capacitor (antenna) will exponentially discharge in relationship to the resistance between the two capacitive plates (two sides of the dipole). When the dielectric constant of the material inside the electric fields is changed (e.g. when the user touches the sensor), the RC time constant changes measurably, thus allowing detection of a touch event.

Figure 6.1 shows a block diagram of an RFID tag enhanced with a capacitive touch circuit. The UHF antenna forms a parasitic capacitor at DC (depicted as dotted lines), which is used as the touch sensing element. The antenna is simply connected to the RFID chip through the two standard RF pads. As with traditional tags, the antenna's impedance (at the RF design frequency) is matched to the complex conjugate of the analog front-end of the RFID chip for maximum power transfer. In order to insure proper operation of the analog front end, a low-pass filter presents a high impedance path blocking the RF signal from the capacitive measurement circuits. Utilizing a first-order RC low pass filter, resistance in the order of $200\text{ k}\Omega$ and capacitance in the order of 5 pF meets the design criteria sufficiently.

The operation of an RFID tag enhanced with the touch sensors is as follows: Once the RFID tag is powered on and operating, the I/O port of the capacitive sensing circuit charges the positive side of the antenna. This DC signal is blocked from interfering with the Analog Front End of the IC due to the rectifier's AC coupling capacitors.

After the positive side of the antenna capacitor is charged to the regulated voltage of

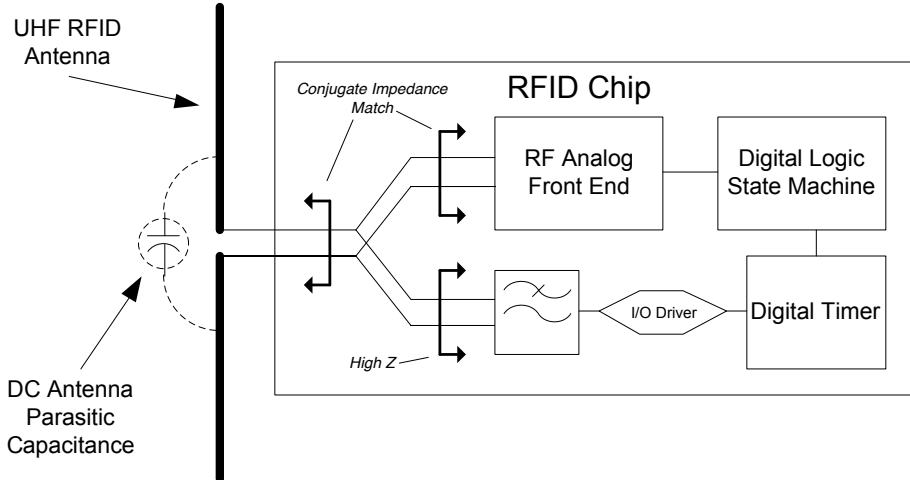


Figure 6.1: Block diagram of the capacitive touch sensor enhanced RFID tag. The antenna forms a sensing capacitor at low frequencies and its RC discharge rate is measured with the digital timer.

the IC, the direction of the port is changed from an output to an input and a digital timer is started to measure the rate of discharge. In order to register a user touch, the time at which the voltage on the capacitor reaches the threshold of the input port is compared to a calibrated or hard-coded threshold time value. Having the ability to change the trigger threshold for a touch event allows a single tag IC to be used in multiple antenna inlays with different absolute DC capacitances. Though the frequency separation of the RFID communication and sensing signals allows for isolation from each other, the event of the user touching the tag does have an effect on the antenna's resonant frequency. The phenomena of tags being detuned by environmental objects is well documented in [17,50]. Thus, careful antenna design is necessary to minimize the potential for the user to detune the antenna. The simple dipole antenna discussed above is only one example of the wide variety of planar antenna structures that are suitable for RFID tags. Alternative antenna designs have the potential to increase the robustness against detuning; however, for the purpose

of demonstrating the feasibility of this sensing method, only the performance of a dipole antenna enhanced is discussed.

It is believed that the proposed capacitive sensing method has the potential to enable a low-cost, mass manufactured solution for user input in passive RFID. In particular, the antenna can still be printed with conductive ink onto a variety of substrates. The complexity of assembly remains the same since only the two original RF ports are needed by the touch sensor. Incorporating the capacitive measurement circuit into the tag's IC would not significantly add to the overall die size. The digital timer and single digital I/O port would take up a relatively small amount of current consumption compared to the space allocated to the RF charge pump and EEPROM on a normal tag. Finally, due to the wide frequency gap between the RF input signal and the operating frequency of the capacitive sensing circuit the low-pass filter can be manufactured with less accurate, but space efficient, on-chip passive components.

6.3 Implementation and Experimental Results

An EPC Class 1 Generation 2 tag has been prototyped to demonstrate the feasibility of capacitive sensing through the tag antenna. Sensor measurements can be reported to a commercial RFID reader in a variety of forms: sensor measurements can be encoded in the tag's ID, used to prevent/allow ID transmission, or retrieved through a read operation to user memory. Finally, the application layer decodes and displays tag sensor information reported by the reader.

The tag prototype is shown in figure 6.2. The antenna consists of copper foil on an FR4 substrate. The antenna is laminated with an insulator to prevent resistive loading of the capacitive sensor. Three fins between the dipole branches increase the sensitivity of the capacitive sensor. Finally, a programmable passive tag is connected to the antenna for capacitive sensing and EPC Class 1 Generation 2 communication.

The tag prototype leverages the WISP (Wireless Identification and Sensing Platform) to perform the capacitive sensing and RFID communication. The WISP is a programmable battery-free sensing and computational platform designed to explore sensor-enhanced RFID applications. The WISP uses a 16-bit, ultra-low-power microcontroller to emulate the EPC

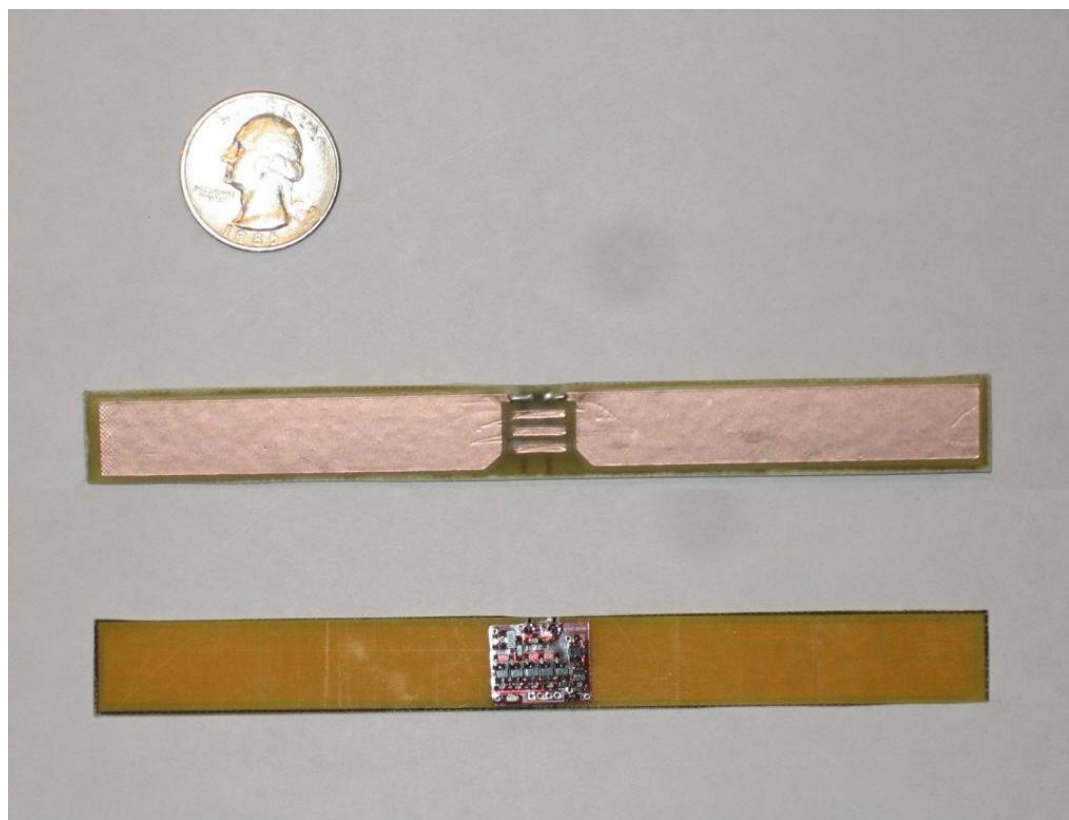


Figure 6.2: Image of the passive UHF RFID tag with a capacitive touch input and LED output for feed back.

Gen2 protocol and perform sensing and computation tasks while operating exclusively from harvested RF energy. A full discussion of the WISP's design and performance is presented in [54].

The features shown in figure 6.1 were added to the WISP in this prototype including a low pass filter and sensing routine to measure the discharge time constant of the antenna. Commercial ASIC tag implementations including this touch interface would also require addition of these components including the low pass filter, bidirectional I/O driver and digital counter for measuring the antenna RC time constant.

Additionally there are a number of applications in which user feedback is necessary; to explore these scenarios an LED is located on the lower left corner of the WISP. Although to date, the incorporation of a LED in to RFID ICs is not readily available, recent work in semiconductor optics has shown promising results. The authors in [2,30] have developed CMOS compatible LEDs operating at 2-3 volts. It is important to note that even with a CMOS compatible process, significant packaging and charge storage issues would have to be overcome. Alternatively, a two chip system (RFID IC and LED) assembled by 3D wafer stacking could be used.

The usage model for the touch-enhanced RFID tag demonstrated here is straightforward. When in the presence of an RFID reader, the touch tag transmits a standard EPC ID. When the user places his/her finger on the input region of the tag (center of the antenna) the LED flashes giving positive feedback that the touch event was registered by the tag and an alternate EPC ID encoding the touch event is transmitted to the reader. Finally, the reader passes the stream of IDs to a host computer which displays a touch event by changing the color of an image of a light bulb, based on when the sensor is touched. From the user's point of view the transaction is seamless; by touching the tag's sensor, the image on the screen is activated and deactivated.

Other encoding scenarios can easily be implemented. The "touched" and "un-touched" states can have different responses: no ID, a dummy ID, or an intended ID may be transmitted, depending on the application. For example, in credit card and passport scenarios it may be desirable that no ID is transmitted unless the sensor is touched.

6.3.1 Antenna Design

The design challenge is to create a 902-928 MHz antenna not adversely affected by the presence of a user's finger while simultaneously being sensitive enough for the RC time constant to be measured. This was accomplished by using Ansoft HFSS for simulation and an automatic stencil cutter for rapid prototyping of the antenna. The antenna was designed for 50 ohms impedance for ease of testing. Additionally, the WISP's analog front end has landings for a discrete matching network which was also tuned for a 50Ω impedance.

When considering how to incorporate the touch sensor it is useful to recall the operating principal of a half-wave dipole antenna. Each arm of the antenna is a quarter wavelength long and open at the ends. When driven at resonance, a sinusoidal standing wave pattern occurs with an oscillating voltage maximum at the ends of the antenna, and a voltage null at the feed point. Thus, the resulting electric field in the vicinity of the antenna port is small in magnitude and the effect of the user's finger is negligible, making an ideal location for the touch sensor.

It is well documented that nearby objects can have a large effect on UHF RFID tag performance as reported in [17, 50]. However in these publications the authors consider the effects of metal planes and objects larger than the scale of the antenna. In the case of the touch sensor, the space that the tip of the finger comes in contact with is sufficiently small in size compared to the overall antenna; thus if the user approaches the tag perpendicular to the antenna axis, the interference from the hand is tolerable.

The dipole antenna shown in figure 6.2 was widened to increase the DC capacitance for the sensing circuit, as well as increase the bandwidth at resonance to help avoid detuning. A design frequency of 920 MHz was used to allow for detuning to a lower frequency. When the user activates the touch sensor in the middle antennae, the change in DC capacitance is approximately 5-6 pF. Figure 6.3 shows simulated and experimental S11 results for the touch sensor augmented dipole antenna. The simulation shows a decrease in the magnitude and a frequency shift to left. This is expected because the increased capacitance of the finger decreased the resonant frequency which affects the ability of the antenna to resonate. The experimental data confirms the trend expressed by the simulation. However, due to

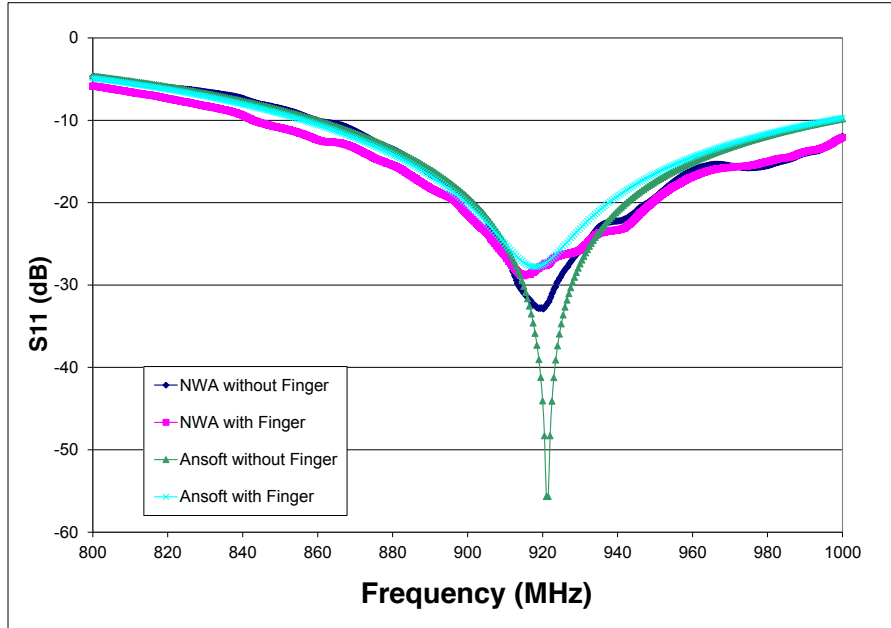


Figure 6.3: Simulated and experimental results showing the S11 response of the RFID touch antenna when active by the user’s finger and when left on touched.

variation in the manufacturing of the antenna and the lack of an anechoic chamber for precise measurement, the un-touched resonant peak is shallower than the simulation.

6.3.2 Capacitive Touch Sensor Performance

In order to add capacitive sensing capability to the WISP, a simple RC low pass filter was added to one of the data I/O pins on the MSP430. As discussed, this creates a high impedance path that blocks the RF signal from reaching the capacitive sensing circuitry in the tag. To create a consistent RC discharge time, an explicit parallel resistor in the mega-ohm range was added to provide a discharge path for the touch sensor.

In order to take a touch measurement, the WISP charges the antenna by outputting a

logical one on a digital I/O pin. The result is that a DC bias of 1.8 V (operating voltage) is applied to the positive port of the antenna. The AC coupling capacitors of the harvester prevent the DC signal from discharging through the RF rectifier. Next the microcontroller sets the I/O pin to an input and starts the digital timer. When the voltage level on the capacitor drops below the threshold of the input pin, an interrupt stops the timer and records the timer value. If the timed value is above the preset threshold a touch is recorded. The measurement is averaged eight times to improve noise immunity and sensitivity.

Using the existing RFID capabilities of the WISP, the onboard microcontroller embeds the touch sensor data into an EPC-complaint ID and reports the ID via EPC Class 1 Generation 2 RFID protocol. Figure 6.4 shows an EPC inventory round followed by the measurements events; the top set of oscilloscope traces shows the untouched tag and bottom set shows the user touching the tag. As expected, the presence of the user's finger adds capacitance which increases the RC time constant of the touch sensor.

Figure 6.5 shows the time series response of three touch events. In this example, the touch tag is configured to transmit raw sensor data back to the reader and host application. The "Timer Count" represents the average of eight consecutive RC discharge times from V_{dd} to $\frac{1}{2} V_{dd}$. This data is then encoded into the EPC ID and transmitted to the RFID reader for data collection. The read rate is 100 queries per second and there are three individual touch events lasting approximately one second each. Additionally, the touch tag is programmed with a threshold of 80 counts (determined empirically) which is used to trigger an LED blink event on the tag.

6.4 Applications

The technique presented here may be used for capacitive user input or other capacitive sensing applications. The user input applications can be divided into RFID-specific input and general-purpose input categories. RFID-specific input means that the primary purpose of the device is RFID (that is, identification, for access control or other purposes), but the behavior of the RFID tag is controlled by the user input. General-purpose input means that the RFID system is being used as a channel for power and data, but the user input is the ultimate purpose.



Figure 6.4: Two RFID tag touch measurement events showing EPC Gen2 protocol and senses capacitor RC discharge. The top plot shows the untouched event and the bottom plot shows the increase in discharge rate caused by the added capacitance of the user's finger.

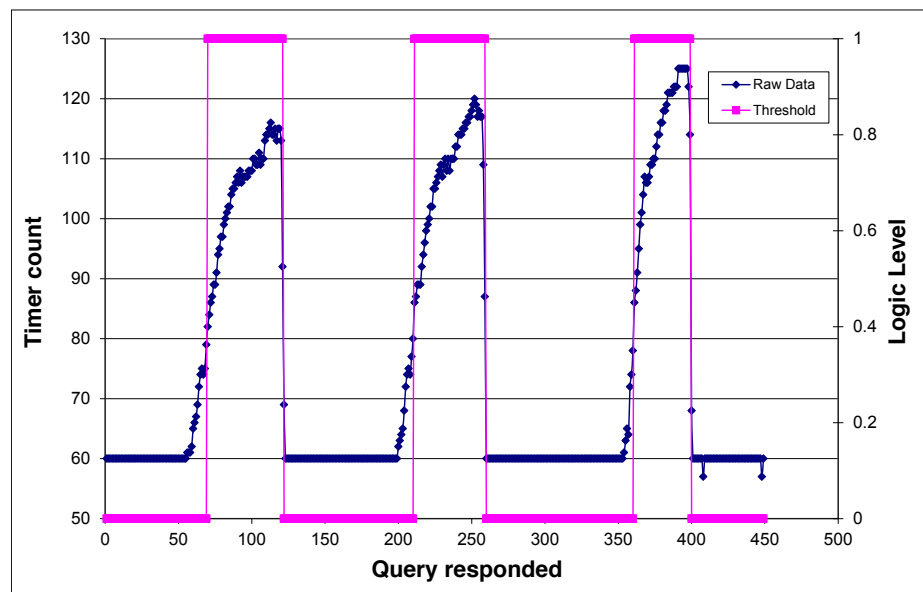


Figure 6.5: Raw capacitive sensor data and identified touch events transmitted to the RFID reader form the RFID tag.

The RFID-specific input applications can help address many of the known privacy and security problems of RFID by giving the user control over when and what type of data is transmitted by the tag. A basic attack involves an unauthorized RFID reader simply interrogating a target tag to track the user or clone the tag's ID. U.S. passports with embedded RFID tags were given a mylar pouch to shield RF signals from activating the tag. Unfortunately this solution relies on the user to be aware of the privacy and security risk associated with RFID, and it requires them to be vigilant about protecting their personal information.

The capacitive input technique presented here could enable a more elegant and cost effective solution to RFID access control. Figure 6.6 shows a touch-enhanced RFID tag that has been built into the form factor of a credit card. The tag indicates, via an LED, that a reader is making a read query. The user then has the option to explicitly authorize the tag to respond. RFID-based payment mechanisms can greatly benefit from bearer control by preventing unauthorized readers from conducting transactions (especially payments) without explicit authorization from the card owner. The authors in [16] have demonstrated a similar system where direct user inputs to a RFID tag enables and disables communication. In this case a 3D accelerometer is used as an orientation sensor and the user performs a secreted handshake or gesture which is analyzed by the tag for authentication.

If multiple buttons were implemented, numeric keypads for a personal identification number (PIN) input could be added to credit cards. This could provide even higher levels of security than single button authorization: if the card were lost, the thief could not authorize an RFID read, thus preventing unauthorized use of RFID access keycards, passports and credit cards. It may be possible to implement a numeric keypad using a single capacitive sensor channel. First, one would implement a linear position sensor by changing the width of the electrode along the position sensitive dimension, so that touch location was encoded by capacitance value. Then one would wrap this linear position sensor in serpentine fashion through the keypad locations. With 12 distinguishable capacitance values, a conventional numeric keypad could be implemented.

The general-purpose applications of the technology are also exciting. Fully wireless, battery-free controllers such as light switches could be implemented as thin, unobtrusive,



Figure 6.6: Touch enhanced UHF near-field RFID tag in the form factor of a credit card

and inexpensive RFID tags adhered to walls, furniture, or elsewhere. If a linear controller is deployed, it could function as a wireless light dimmer controller, fan speed controller, or other analog controlled device. Input devices such as remote controls could also be implemented using this technology. The minimal form factor and potential low cost would be a good match for plush or plastic toys. The technique could also be used for user presence detection. For example, it could be integrated into furniture to detect user presence and pose.

Pure sensing applications (non-user interface) are also compelling. The label form factor and low cost architecture enable integration of a capacitive sensor tag into many types of end-user packaging. For example [66] uses an external capacitive sensor to measure the level of milk in a carton. Alternatively the capacitive sensor could measure a wider variety of phenomenon by placing a material whose dielectric constant is affected by other physical parameters in the vicinity of the sense electrodes. There are a number of sensors that work in this fashion including humidity, temperature, pressure, and displacement.

6.5 Summary

This chapter presents a proof-of-concept of a dual use RFID antenna for traditional power and communication, as well as for detecting user input by means of a capacitive sensor. The method presented requires no change in form factor or manufacturing processes compared to ordinary passive UHF RFID tags.

This technique has the potential to solve a number of known RFID privacy and security problems, by giving the user of the tag, explicit control over whether it responds to a reader. Beyond security and privacy, it enables other tag user interfaces, where the goal is user interaction with the environment. For example, touch sensor tags could enable simple input devices (embedded in objects such as toys, adhered to walls, etc) that are unobtrusive, wirelessly powered, and potentially inexpensive. Finally, this technology could enable other types of capacitance-based environmental sensing without requiring any change in the form factor or manufacturing processes from today's passive RFID tags.

Further work will be necessary to design a robust antenna that is optimized for both wide-band RF performance and high sensitivity for capacitive sensing. The tag's integrated

circuit will need to be modified to include the RF isolating low pass filter, a bidirectional I/O circuit, and the digital timer for measuring the RC discharge.

Chapter 7

WIRELESS AMBIENT RADIO POWER

Radio frequency (RF) signals provide a near ubiquitous energy source due to the large number of TV, radio, cellular, and Wi-Fi transmitters that proliferate our urban environments. While the traditional use of RF transmission is for data transfer, it is possible to harvest, convert, and store this energy for use in a variety of applications. In general, the energy harvesting process includes four stages: excitation of current in an antenna by an incident electromagnetic wave, rectification of the resulting power at the antenna output, conversion of this power to optimal voltage and current levels, and finally, energy storage in a capacitor or battery for later use.

7.1 WARP TV Harvester

Ambient RF energy harvesting begins with a source, such as a TV or radio transmitter, where power is continuously transmitted in the form of data signals. Generally speaking, the RF energy is evenly radiated horizontally, with power intensity decreasing as it travels from the source. Consider the example depicted in figure 7.1, which shows a TV tower located at point “A”. The radiation pattern of the transmitter results in power contour lines that fall off as the reference point (or receiver) moves away from the transmitter. If, for example, an energy harvesting device with an activation threshold of $100 \mu\text{W}$ is brought towards the TV tower there will be a particular distance at which the device will begin to operate. Thus, the power requirements of the load application defines the maximum distance of operation. This distance represents a radius of operation around the TV tower which encircles an area, wherein the device will continually harvest energy for operation. Initial research on the Wireless Ambient Radio Power (WARP) project has demonstrated the feasibility of developing such a device, capable of having an operating area of several hundred square miles around the transmission tower.

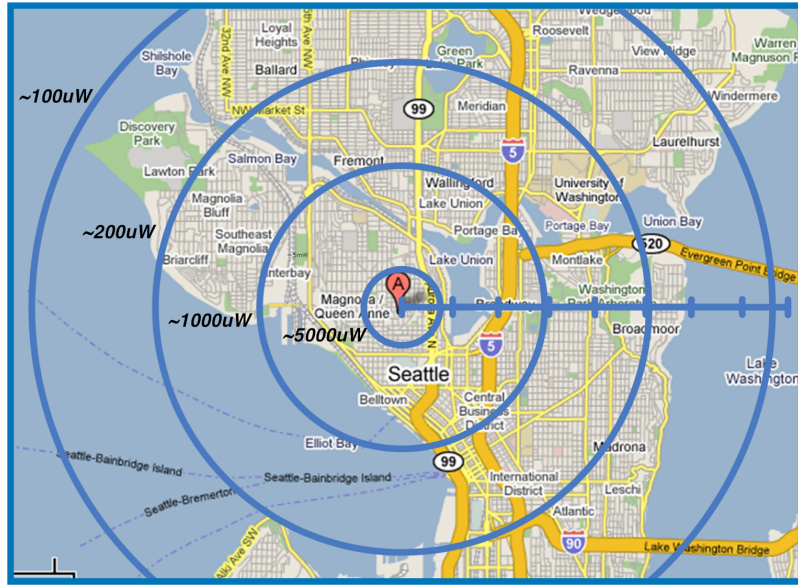


Figure 7.1: Position ‘A’ indicates the location of the KING-TV tower which transmits 960 kW. The contour rings estimate the available receive power for the Seattle region (assuming line of sight and a 5dBi receive antenna).

Figure 7.2 shows an image of the WARP TV harvester, consisting of a commercially available digital TV antenna and an RF rectifier. To demonstrate the harvesting functionality, a Radio Shack indoor/outdoor thermometer with hygrometer (Cat. No. 63-1032) is connected to the output of the rectifier as an example application. From the balcony at Intel Labs Seattle ($47^{\circ} 39' 41''$ N, $122^{\circ} 18' 60''$ W), I harvested RF power from the KING-TV tower ($47^{\circ} 37' 55''$ N, $122^{\circ} 20' 59''$ W), which broadcasts 960 kW EIRP on channel 48 at 674 - 680 MHz. The total distance is 4.1 km. The antenna used is a 5 dBi log periodic antenna designed for TV applications. The power harvester is a 4 stage, voltage multiplying rectifier, the design of which is similar to that of the one used on the WISP. The RF front end is tuned to the desired channel and has a bandwidth of approximately 30 MHz. With the antenna manually oriented towards the transmit tower, the measured open circuit voltage at the rectifier output was 5.0 V (i.e. the only load on the power harvester was the voltmeter). Next, an $8\text{ k}\Omega$ load was attached to the rectifier output, resulting in an output voltage of 0.7 V, which corresponds to $60\text{ }\mu\text{W}$ of power harvested. This is equivalent to the



Figure 7.2: Demonstration of a temperature and humidity meter (including LCD display) that is exclusively powered from ambient RF signals transmitted by the TV tower seen in the background, at a distance of 4.1 km.

net power budget of many of the WISP sensing applications.

Applying the Friis transmission formula with the parameters above, yields an expected power received of $220 \mu\text{W}$. Thus, the experimentally measured performance of the system is reasonably close to the theoretically expected performance. We then connected this ambient RF harvesting system to the battery terminals of the Radio Shack indoor/outdoor temperature and humidity meter (thermometer/hygrometer) with an LCD display. This device is normally powered by a 1.5 V AAA battery. The thermometer/hygrometer was measured to consume around $25 \mu\text{A}$, at 1.5 V , from a laboratory power supply. Approximately once per second, the current consumption briefly spiked up to around $50 \mu\text{A}$, presumably when the sensor measurements were made.

The thermometer/hygrometer functioned normally when connected to the power harvesting circuit with the antenna oriented at the appropriate transmission tower; the display

contrast appeared to be as good as when the system was powered by a battery. With the antenna oriented directly at the TV tower and the thermometer/hygrometer connected and operational, the loaded voltage was measured to be 1.7 V. As the antenna was oriented away from the tower to which it was tuned, the display contrast dropped and then, when the antenna was further mis-oriented, appeared to stop operating altogether.

7.2 WARP Sensor Node

The previous section showed the ability to harvest ambient RF energy and power a dedicated sensor and display. Although this example aptly demonstrates the possibility of RF energy harvesting, the application itself is somewhat limited in its scope. The next logical extension of ambient RF energy harvesting is to use this capability to enable new applications and usage models. One compelling area of application is wireless sensor nodes, which have computational, sensing, and bi-directional communication capabilities.

For as long as there have been wireless sensors, researchers have searched for ways to sustainably power them in remote locations. Today, there are numerous remote sensor applications deployed across a wide range of disciplines. These include environmental monitoring, such as volcano or hurricane sensors, to industrial monitoring of strain, vibration, consumable parts, and machine degradation. Solar power is generally viewed as the most usable source of ambient energy, and when present, it provides a viable source of power for remote sensors. However, solar powered systems suffer from the limitation that they must be placed in well-lit areas and must have line of sight to the light source. Additionally, since there is no sunlight at night, operation is often quite restricted. Batteries can mitigate this restriction and allow devices to continue operating for a short time after ambient light is removed. However, dependency on batteries can be troublesome, and in many cases, it is too costly or time consuming to replace each node after the battery is empty.

Furthermore, we must consider the total system complexity of solar powered sensor nodes. Typically, there is an integrated circuit for computation and sensing, an antenna for communication, a solar cell for power, and a battery for storage. In contrast, a passive RFID tag is simply made up of an antenna and an integrated circuit. If we extend the concept of a passive RFID tag to include energy harvesting from ambient RF sources, instead of

a deliberate source such as an RFID reader, we can see that this system is inherently less complex. Although ambient RF power is not as abundant as solar power, the low manufacturing complexity and potentially uninterrupted power supply of a WARP type solution will make it viable for a number of application scenarios.

The Wireless Ambient Radio Power (WARP) project aims to create wireless sensor nodes that are completely powered off of harvested RF energy. In order to accomplish this goal, the existing WARP energy harvesters were extended by adding the capability to sense the environment, perform computation, and communicate wirelessly. The first target application is a weather monitoring node. Figure 7.3 shows a block diagram of the system, which receives RF power from a TV transmitter and wirelessly reports that data back to a host computer.

Figure 7.4 shows a block diagram of the sensor node architecture. The harvesting antenna is connected with a SMA connector so that different frequency ranges and antenna gains can be easily tested. Received RF energy is fed to the rectifier via a tunable impedance matching network. Rectified energy is gathered over time and stored on the capacitor bank until the voltage threshold for the application is met. The power management circuit controls basic duty cycling and regulation. The MSP430 microcontroller provides a higher level of power management by choosing when to take sensor measurements and controlling when to power the CC2500 low power transceiver. When ready, the MSP430 takes sensor measurements, computes the data payload, and communicates back to the base station using the CC2500 radio IC. A back of the envelope calculation estimates the energy required for a burst of 16 bytes to be approximately 3 mJ.

7.2.1 RF Harvester and Power Management

Figure 7.5 shows a schematic of the WARP RF harvester consisting of a LC impedance matching network that conjugate matches the antenna's impedance to the input of the multi-stage rectifier. For this application, it was necessary to maximize output voltage so a five stage voltage doubler was used instead of the four stage used in the previous application. The rectified voltage is stored on eight $47 \mu F$ low loss ceramic capacitors, for a total of 376

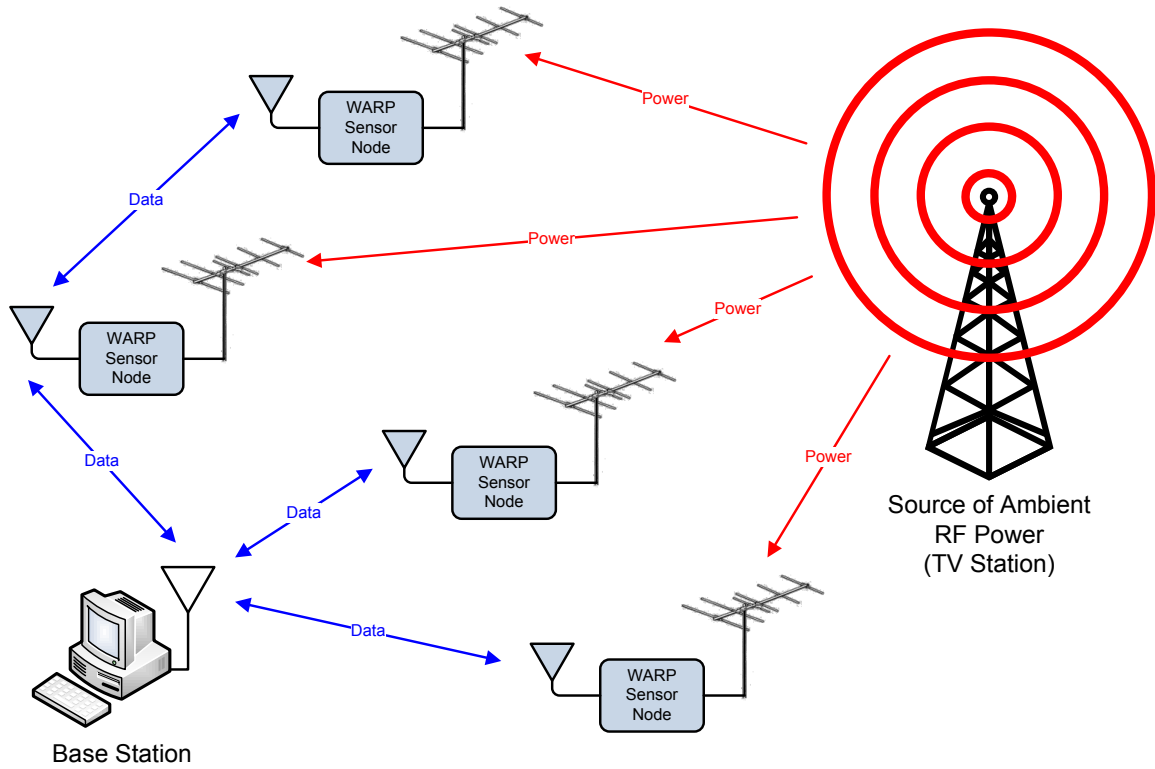


Figure 7.3: Conceptual diagram of a deployment of WARP sensor nodes. The WARP nodes harvest ambient RF power from TV stations for operation and communicate back to a base station using an onboard radio.

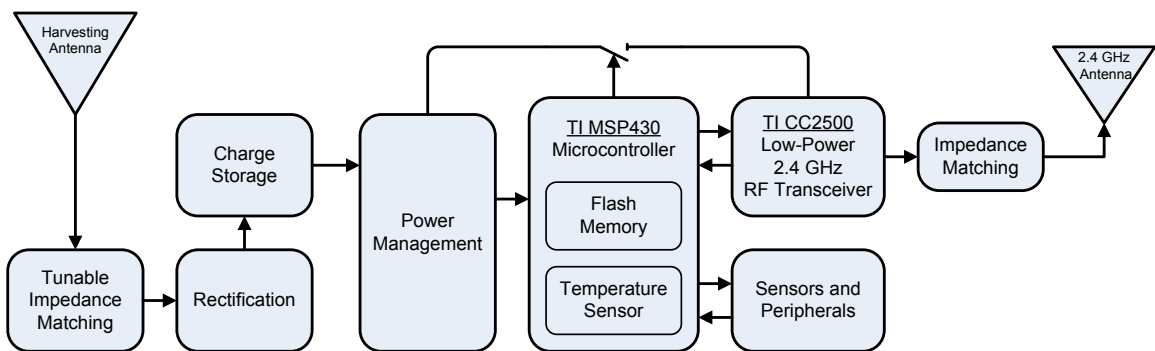


Figure 7.4: Block diagram of the proposed WARP sensor node with 2.4GHz transceiver.

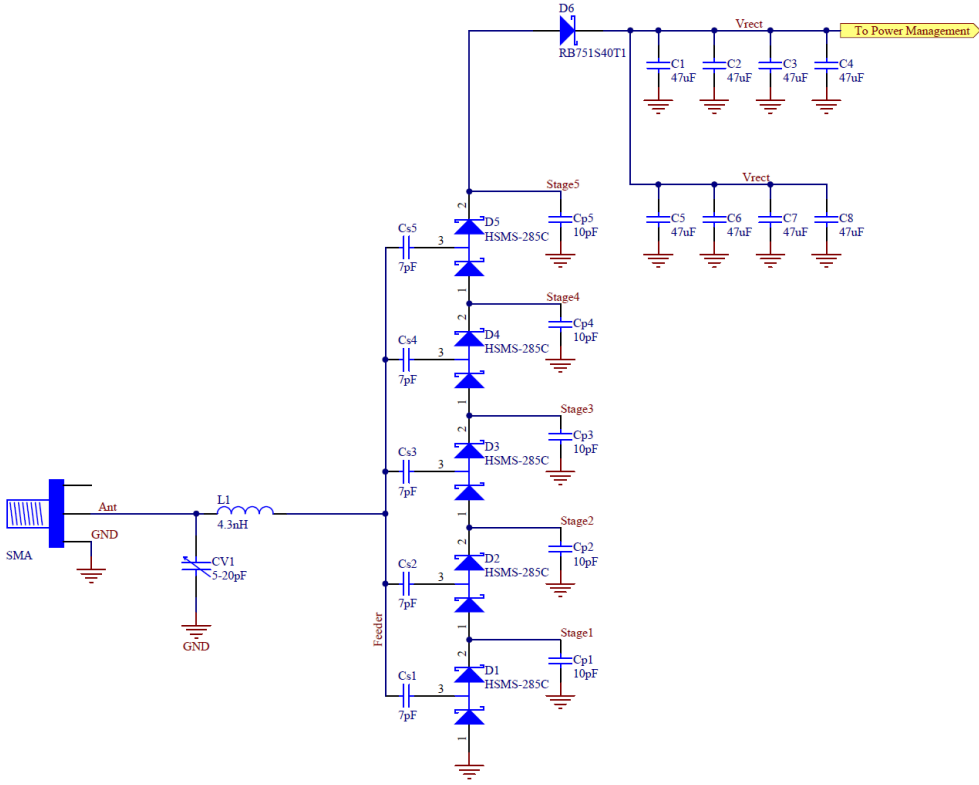


Figure 7.5: RF power harvesting circuit consisting of a LC impedance matching network, a 5 stage voltage multiplier, and a $376 \mu F$ capacitor storage bank.

μF of charge storage.

Figure 7.6 shows the power management circuit, which consists of a 3.3 V Low Drop Out (LDO) linear voltage regulator and two voltage supervisors with detection thresholds of 2.0 V and 4.5 V, respectively. The reason for the two voltage supervisors is that the control signal that enables the output of the regulator needs a wide hysteresis window. Consider the following example, at startup the rectified voltage is small and both supervisors are low, causing the regulator to be disabled. Thus, the quiescent current draw of the system is small, which allows the circuit to harvest and store energy on the capacitor bank. When the rectified voltage reaches 4.5 V, the primary supervisor enables the regulator, which supplies voltage to the MCU. Typically, these supervisors have only 0.1 V of hysteresis, which means

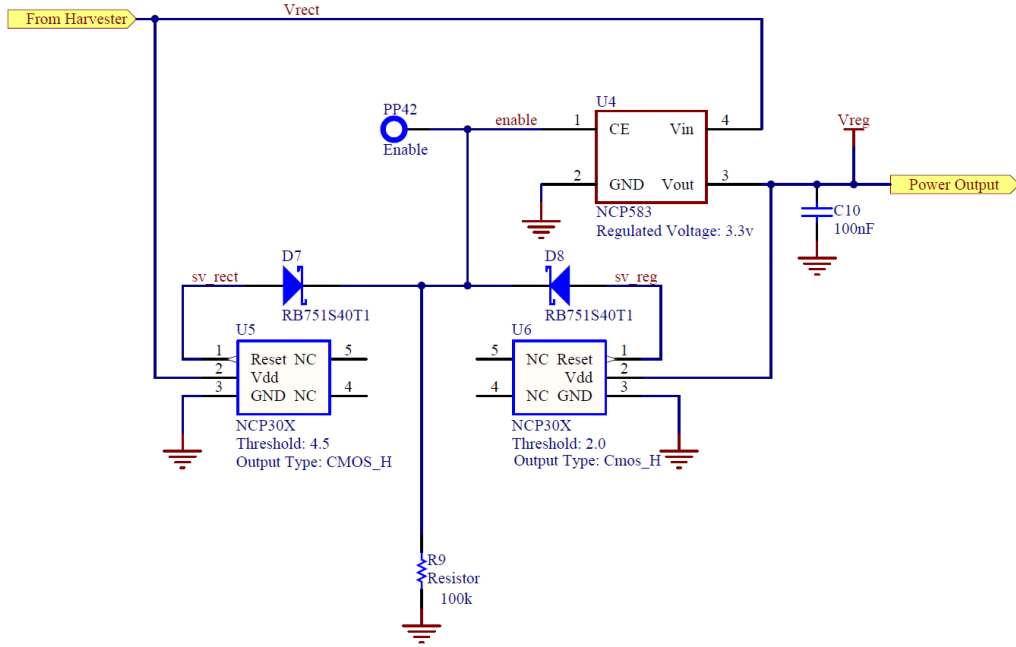


Figure 7.6: The power management circuit allows charge to accumulate on the capacitor bank until 4.5 V is reached, at which point the circuit enables the regulator until the storage charge drops below 2.0 V.

that when the voltage on the capacitor bank drops below 4.4 V, the primary supervisor will immediately disable the regulator, halting operation. To prevent this from happening, the secondary supervisor, which has a threshold of 2.0 V, is fed by the regulator output. This feedback circuit keeps the regulator enabled until the output drops below 2.0 volts. Once the rectified voltage is below 2.0 V, the system enters its low quiescent current state and the cycle repeats.

In this system, there are two additional key voltage conditions that should be kept in mind. One, the LDO regulator, when enabled, will pass current if the input voltage is less than its specified regulated output voltage (3.3 V in this case). This means for $V_{in} \geq 3.3V, V_{out} = 3.3V$ and for $V_{in} \leq 3.3V, V_{out} = V_{in}$. Two, the MSP430 will meet the required time constraints (for this application's clock speed) down to ~ 2.0 V. Therefore,

even though the voltage supplied to the MSP430 is unregulated from 3.3 V to 2.0 V, reliable operation will occur. The result is that all the charge that is stored on the capacitor bank from 4.5 V to 2.0 V is available for use. Future revisions of the WARP power management circuitry will focus on reducing the required MCU voltage down to 1.8 V by lowering the required clock speed for operation and by using a higher efficiency regulator.

Several sensors are also included on the WARP board. The analog to digital converter (ADC) and associated sensor circuits are constructed to minimize power consumption. The general technique used in creating the sensor circuits is that the microprocessor will control a line that enables the sensor by pulling a pin high. This prevents power leakage from the sensors when not in use. The sensors used in this design include an ambient light sensor, a thermometer, and a voltage divider connected to the capacitor bank. The voltage divider enables measurement of the energy stored in the capacitor bank.

7.2.1.1 Radio Transceiver and Embedded System

The WARP sensor node uses Texas Instrument's MSP430F2272 microcontroller for sensor measurement, computation, and to interface with the TI CC2500 low power 2.4 GHz RF transceiver. The MSP430 is an excellent device for low power sensing applications. It consumes 400μ A in active mode at 8 MHz and 600 nA in standby mode, and can operate from 3.3 V down to 1.8 V. The CC2500 low power radio also operates at 1.8 V and requires 15 mA while transmitting, and 400 nA while in sleep mode. Additionally, the CC2500 supports the TIs SimpliciTI protocol for small, low power RF networks.

The embedded software in this system performs three primary tasks. First, it manages the power usage and optimizes the circuit for low power consumption. Second, it collects data and constructs packets to send back to the access point. Third, it handles data transmission and communication protocols. Since power is very limited, the code is constructed in a way that minimizes the impact of unexpected power failures by sampling the stored voltage and entering low power mode until data transmission is possible.

When conducting the ADC measurements, there are three steps which help reduce power consumption. The sensor is normally disabled, so that it consumes no power. When a sensor

measurement is to be made, the sensor enabled pin is driven high to enable the sensor. Next, the microprocessor enters standby mode LPM1 for 250 cycles ($31 \mu\text{s}$) to conserve power while the ADC reference voltage settles. Then, the microprocessor wakes up and reads the measured voltage.

The transceiver architecture is based on the TI eZ430-RF2500 wireless development tool kit. A second TI eZ430-RF2500 board acts as a base station hub when attached to a host computer. The WARP board wirelessly communicates with the host node at a range of up to 30 feet using the Texas Instruments SimpliciTI protocol. In order for the system to operate off of ambient RF TV power, the protocol had to be modified in two ways to reduce power. In the SimpliciTI protocol, nodes randomly generate a 64bit identification number and broadcast it to initiate linking. Then, the access point replies with its address. Linking requires the node to spend power on transmitting its ID number and receiving an access point address. The linking process requires both TX and RX, which both draw 15 mA. Due to the power requirements of this project, we decided to bypass this linking procedure and give each node a hard coded, 8bit identification number. These two changes allow the microprocessor to transmit data reliably while reducing the amount of harvested power needed to accomplish packet transmission.

7.2.2 Analysis of Power Usage

Figure 7.7 shows an image of the complete WARP sensor board. Initial development of the system firmware was done with bench top equipment to better control system variables. In order to emulate the harvested RF power, an $8 \text{ k}\Omega$ resistor was placed in series between a bench power supply and the capacitor bank (i.e. the V_{rect} node in figure 7.5). This resistor approximates the output resistance of the rectifier. By adjusting output voltage of the power supply, different amounts of power can be injected into the WARP board. Measurements show that approximately $50 \mu\text{W}$ of harvested power is required to charge the capacitor bank up to 4.5 V at a cycling rate (charge/discharge) of 20 Hz.

Measurements of the microcontroller and transceiver showed that approximately 2.8 mJ of energy is consumed each time a packet is sent. The total transaction time is 8.3 ms.

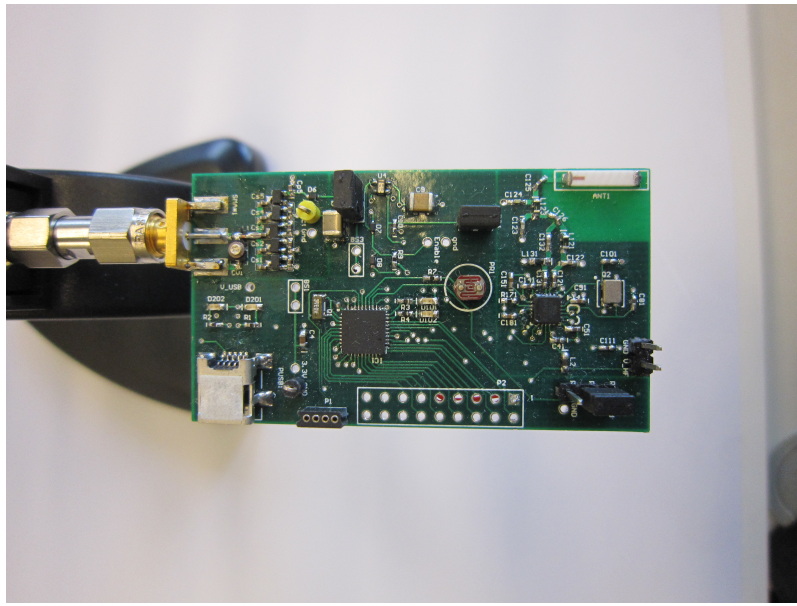


Figure 7.7: WARP sensor node consisting of a rectifier, power management circuitry, sensors, and 2.45 GHz transceiver with ceramic chip antenna (power harvesting antenna not shown).

In order to understand the details of where power was consumed, the microcontroller was programmed to toggle a debug pin at each stage of operation. In this experiment, the system was powered with the same RC circuit used earlier to emulate harvested power. Once the 4.5 V supervisor triggered the transmit cycle, an oscilloscope was used to record the change in voltage on the capacitor bank. Figure 7.8 shows the annotated transmission cycle. The general microcontroller operation and analog to digital conversion consumed a very small percentage of the overall power used. Only 8.4% of the power consumed went towards running the microprocessor and bringing the device back into active mode. While 9.1% was consumed by the analog to digital sensor readings, 13.6% of the power was spent by the SimpliciTI protocol preparing to send data, 19.5% was consumed initializing the CC2500, and 49.4% was spent transmitting data.

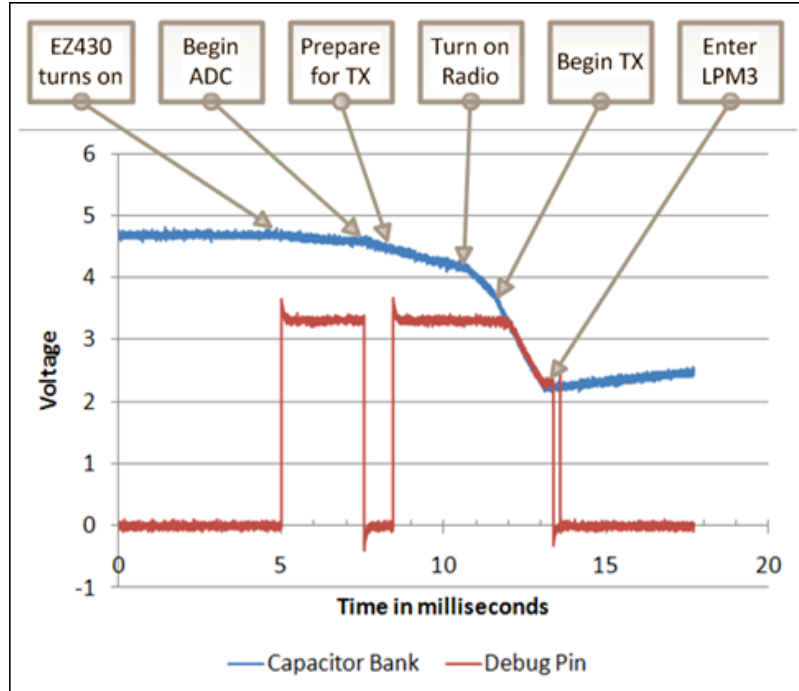


Figure 7.8: Scope plot of a packet transmission cycle annotated with program events.

7.2.3 Field Test of the WARP Sensor Node

Figure 7.9 shows the completed WARP sensor node, which uses the same 5 dBi log periodic antenna used in section 7.1. A trial run of the WARP sensor node was conducted on the balcony of Intel Labs Seattle. The base station and host computer were located inside the Intel office, approximately 10 feet from the WARP node. For this experiment the device was configured to take measurements and send data once every 5 seconds. This provides an extra margin of safety to ensure that harvested power remains higher than consumed power. During this trial run we successfully monitored ambient temperature, ambient light, and the voltage of the capacitor bank.

Figure 7.10 shows the collected data over a 24 hour period. The ambient light level drops off starting at 7:50pm and it is completely dark by 9:10pm. The temperature begins dropping off with the ambient light level and continues to decline until sunrise, at approximately 5:00am. In the figure, it can be seen that the energy harvested increases from 8:30pm to

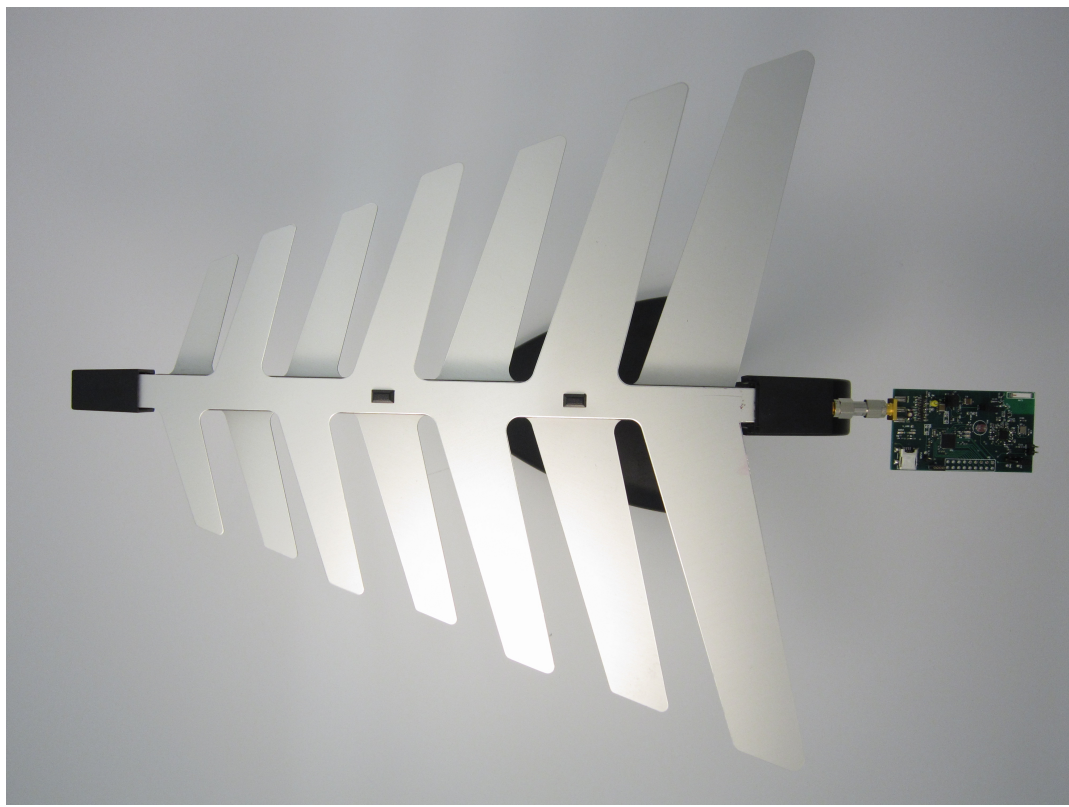


Figure 7.9: Image of the fully assembled WARP sensor node consisting of a 5 dBi log periodic antenna and custom circuit board.

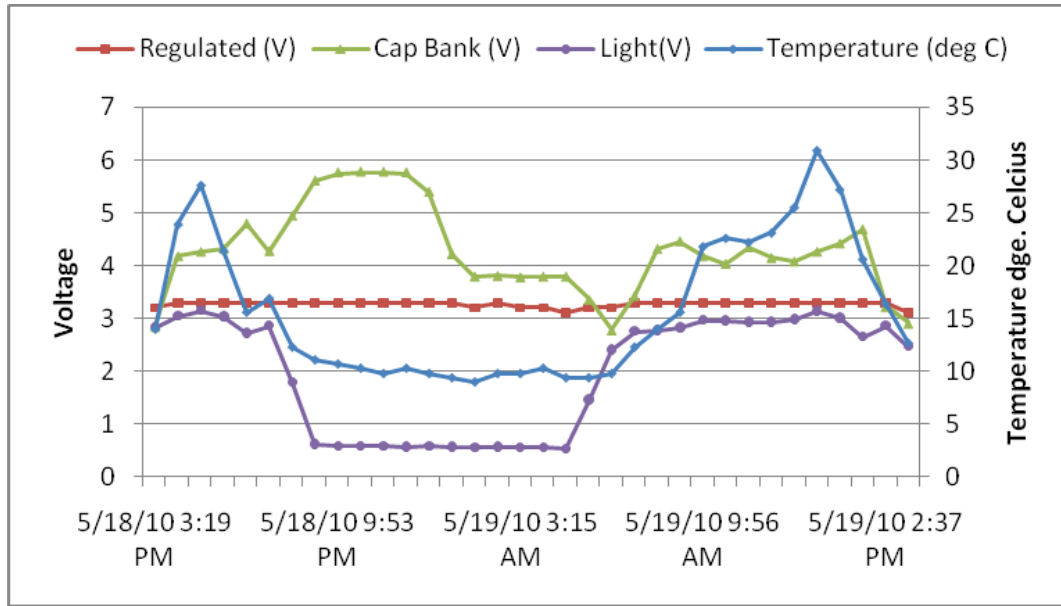


Figure 7.10: Data recorded over a 24 hour period while operating off of harvested RF power.

9:00pm and is sustained until approximately 12:30am. It is hypothesized that this is due to the station boosting the signal strengths to account for changes in the atmosphere, which is a common occurrence in long distance communication systems.

7.3 Summary

This project successfully demonstrated the ability to harvest wireless ambient radio waves and use them to power both a commercially available home weather station and a custom built wireless sensor node. We tested the sensor node at a distance of 4.1 kilometers from the TV broadcast tower and wirelessly reported sensor data back to a host computer at five second intervals. Future work will focus on refining the sensor node in several ways. First, optimizing the firmware to reduce the MCU clock speed will allow for operation at 1.8 V, thus saving power. Second, a switching regulator should be used in the power management circuit to more efficiently convert energy stored in the capacitor bank to the 1.8 V required for system operation. Finally, new antenna designs should be explored to optimize for size, bandwidth, and gain for a given application.

As hardware power requirements continue to drop, the viability of using ambient radio energy will continue to rise. The system described in this chapter is a first step towards harnessing this ambient RF energy. There are numerous wireless sensor networks in existence today, which are quite constrained by both battery power and the limitations of other harvesting techniques. The prospect of applying this system in new ways is exciting, given the abundance of ambient RF energy in urban areas. This platform enables wireless sensor systems to run perpetually, with no battery or data collection maintenance required.

Chapter 8

CONCLUSION

This dissertation has focused on developing methods of wirelessly powering electronic devices. The applications presented range from micro-powered sensor systems to full laptop computers and the distance at which these devices can be wirelessly powered ranges from meters to kilometers. The source of the wireless power can be dedicated transmitters that are highly coupled into an end-to-end system, or ambient radio waves that permeate our environment.

These capabilities offer the potential to fundamentally change the way people use technology, just as wireless communication has enabled many new mobile sensing and computing applications. Effective means of wireless power will allow for these mobile devices to be seamlessly embedded into our environment, into our tools and equipment, and even implanted into our bodies. Furthermore, wireless power offers the ability to remove the last wired connection needed to charge our mobile devices, potentially enabling smart work spaces where devices are effortlessly powered and charged simply by being placed within the field of a transmitter.

8.1 Dissertation Summary

Wireless power technology offers the promise of cutting the last cord, allowing users to seamlessly recharge mobile devices as easily as data is transmitted through the air. Magnetically coupled resonant structures offer a unique set of benefits as well as design challenges when used for wireless power transfer. One of the remarkable results is the existence of the ‘magic regime’, where efficiency remains nearly constant over distance as long as the receiver is within the operating range of the transmitter. This is not the case for conventional far-field and near-field wireless power systems, whose efficiencies decline sharply with range.

The work in this dissertation provides a deeper understanding of the underlying princi-

plies of coupled magnetic resonance, as well as a straight forward circuit model of the system. A derivation of the transfer function of this model reveals which concepts play a critical role in system performance: frequency splitting, critical coupling, and impedance matching. In order to accurately characterize the wireless power system, measurement techniques that use a network analyzer for circuit parameter extraction have been implemented. Excellent agreement between the circuit model and measurements has been demonstrated, with a coefficient of determination of $R^2 = 0.9875$. The issue of receiver alignment sensitivity is also addressed with an adaptive tuning algorithm. We demonstrate that for nearly any receiver position and/or orientation, a frequency can be identified that maximizes power transfer efficiency. Lastly, a tracking algorithm allows for the peak efficiency to be maintained as the receiver is moved in space. In addition to near-field wireless power transfer techniques I have also worked on far-field systems, including enhancing micro-powered UHF RFID tags and RF energy scavenging devices.

The Wireless Identification and Sensing Platform (WISP) is a programmable, battery-free sensing and computational platform, designed to explore sensor-enhanced radio frequency identification (RFID) applications. WISP uses a 16-bit, ultra low power microcontroller to perform sensing and computation, while exclusively operating from harvested RF energy. Sensors that have successfully been integrated into the WISP platform to date include: temperature, ambient light, rectified voltage, and orientation. Since the WISP is essentially a software defined RFID tag, the MCU was programmed to emulate the EPC Gen 2 protocol to communicate sensor data back to a RFID reader. To the authors knowledge, WISP is the first fully programmable computing platform that can operate using power transmitted from a long-range (UHF) RFID reader and communicate arbitrary multi-bit data in a single response packet.

Finally, the Wireless Ambient Radio Power (WARP) project aims to create wireless sensor nodes that are completely powered off of harvested ambient RF energy. This work has many similarities to the WISP, but the transmitters that wirelessly power WARP devices were never intended to be sources of far-field wireless power. Radio frequency signals provide a near ubiquitous energy source, due to the large number of TV, radio, cellular, and Wi-Fi transmitters distributed throughout our urban environments. While the traditional use of

RF energy is information transmission, it is possible to harvest, convert, and store this energy using dedicated devices. The WARP project successfully demonstrated the ability to harvest ambient radio waves and use them to power both a commercially available home weather station and a custom built wireless sensor node. The sensor node is capable of sensing the environment, performing computation, and communicating wirelessly with a base station, all while being powered off of harvested RF energy. We tested the sensor node at a distance of 4.1 kilometers from the TV broadcast tower and wirelessly reported the light level, temperature, and harvested voltage level back to a host computer, located 10 feet away.

8.2 WISP Challenge

The Wireless Identification and Sensing Platform (WISP) project presented in this dissertation is intended to be a research vehicle that allows people both inside and outside of the RFID community to explore new applications and usage models for RFID. Traditionally, RFID tag designers have been specialists in integrated circuit design. They have generally focused on innovating CMOS circuit blocks, such as RF rectification, power management, and low power state machines, with the goal of increasing tag read range. The process of manufacturing these custom integrated circuit tags presents a significant barrier to entry when considering the high cost of software, servers, chip fabrication, and specialized testing equipment, not to mention the long fabrication cycles.

Consequently, when researchers do add additional functionality, such as ADC and light sensors, the focus is on the device and is not driven by any particular application. It is important to note that custom IC tag design will undoubtedly offer longer range, better performance vs. power consumption, and lower manufacturing costs in large volumes. However, it is difficult under this design paradigm to develop new applications that will take RFID beyond simple item tracking and item identification.

In contrast, WISPs are PCB-based, flexible platforms that allow a relative novice to prototype both hardware and software RFID designs in a bench-top setting. The full-featured microcontroller allows for fast code development with debugging support. Sensors and peripherals can be easily added via the exposed headers or by using an optional daughter

board. Testing equipment generally consists of an RFID reader and an oscilloscope. When compared to IC tags, probing and debugging circuit elements is easy and straightforward, as many of the signal lines are exposed by the PCB design.

The WISP fundamentally lowers the barrier to entry and allows people from a wide variety of fields to develop RFID technology. Whether it is students as part of a class project, security specialists, consumer electronics designers, or even artists, it is believed that a diverse group of people will be able to advance RFID technology and find new application spaces and usage models. The hope is that when compelling ideas are discovered, IC tag designers will be able to draw upon the lessons learned from the WISP when designing their custom tags.

In order to enable the wider research community to gain access to WISP technology, the WISP team, consisting of UW and Intel Labs Seattle members, launched the WISP Challenge in December of 2008. This program open-sourced the firmware and hardware for public use and created a wiki and software repository. Next, the team solicited proposals from the academic community and made merit based awards of small batches of WISPs and RFID readers. To date, over 300 WISPs have been donated to over 50 research groups and universities around the world. Thus far, 50 publications have been produced by the WISP community. Applications range from RFID encryption, activity inference, sleep monitoring and evaluation, implanted medical devices, and many others.

8.3 Future Work

8.3.1 Adaptive Impedance Matching Rectifier

One of the most significant problems facing the widespread use of magnetically coupled resonators for wireless power transfer in uncontrolled environments is the issue of regulatory compliance. For this reason, it is desirable for the system to operate in a narrow frequency band, rather than in a wider frequency band used in the adaptive frequency tuning method previously described in chapter 3.6. For example, one might want the wireless power system to stay inside one of the dedicated Industrial Scientific and Medical (ISM) bands. One key fact is that when magnetically coupled resonators are driven at a fixed frequency their

output impedance will vary as a function of distance (i.e. k_{23} coupling). To accomplish fixed frequency operation, I propose to design and build an RF rectifier capable of dynamically adjusting its input impedance to match changes in the coils' output impedance.

In the adaptive frequency tuning work, we were effectively retuning the operating frequency to a point where the input impedance of the coils was 50Ω , which resulted in optimal power transfer. Further mathematical analysis has shown that when operating at a fixed frequency, the output impedance of magnetically coupled resonators changes as a function of distance (i.e. k_{23} coupling). Thus, frequency tuning a system of fixed loads is analogous to impedance tuning a system driven at a fixed frequency. One caveat is that impedance tuning alone may not be able to produce maximum efficiency at very close ranges for all types of coil configurations. This is because at short transmitter to receiver distances the k_{23} coupling may be so large that it forces the target load impedance to be very close to zero ohms (0Ω), which may not be practical to achieve.

Therefore, in order to develop a wireless power system using magnetically coupled resonators that operates at a fixed frequency, it is necessary to control the input impedance of the rectifier. In order to control the input impedance of the rectifier, the ratio of the output voltage and current (i.e. impedance) that is drawn off the rectifier must be properly controlled. Thus, I propose an active impedance matching rectifier that will control its input impedance to optimize the source to load power transfer efficiency.

A diagram of the matching rectifier is shown in figure 8.1. Starting from the left, the WREL system is represented by a RF source with variable output impedance. It should be noted that, for a system with symmetric transmit and receive coils, the output impedance variations are purely real, as shown on the Smith Chart pop out. Next, the rectification stage will demonstrate load and source dependencies as described above. To address this issue, an adaptive impedance matching circuit is added. The topology of this circuit is made up of a feed forward buck converter. By varying the duty cycle of the converter, the ratio of voltage to current that is pulled off of the rectifier will be changed. Buck converters are typically used for voltage regulation, but can be thought of as a non-linear impedance matching circuits. The active impedance matching circuit will deliver maximum power transfer from the output of the WREL system to the next stage, but the voltage

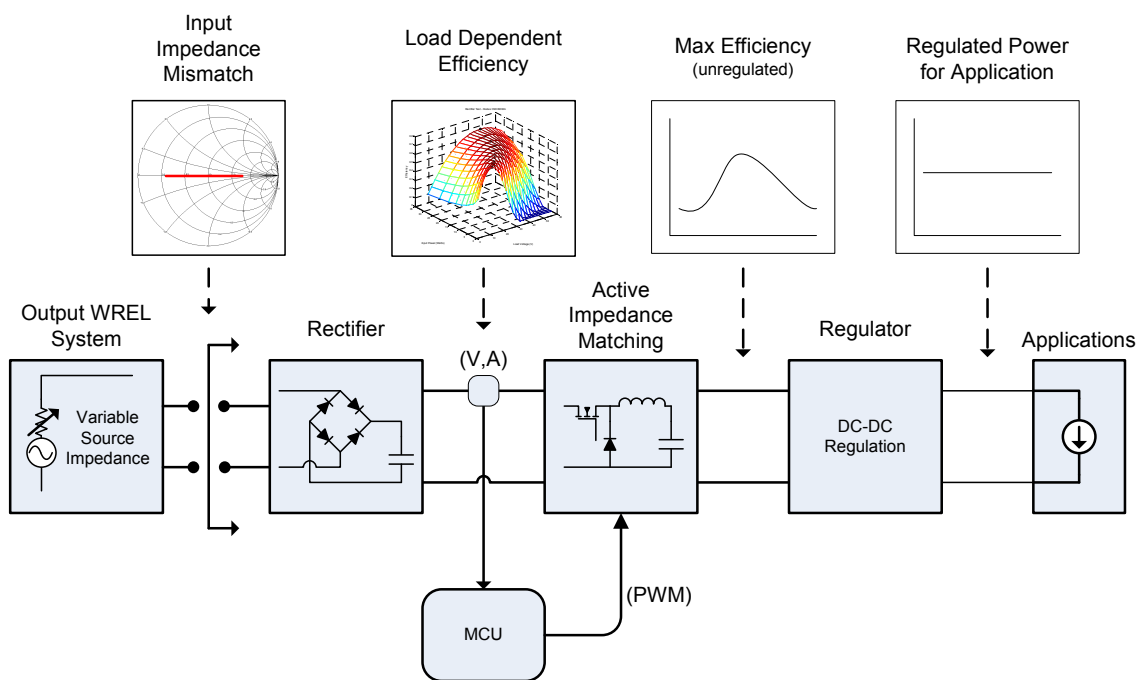


Figure 8.1: The proposed method uses an active feed forward buck converter and microcontroller to control the input impedance of the enhanced rectifier.

will be unregulated. The final power conversion state is to regulate the voltage for the load application.

8.3.2 Wirelessly Powered Ventricular Assist Device using WREL

A compelling application area for the Wireless Resonant Energy Link (WREL) project is powering implanted medical devices. WREL has the advantage that it can transfer large amounts of power safely and efficiently over short distances. Plus, it can adapt to changes in the environment, such as the patient moving orientation or position. One application that is being pursued is wirelessly powered ventricular assist devices (VAD), which are used to help a damaged heart pump blood.

Ventricular assist device (VAD) therapy has significantly improved patient outcomes by technological innovations based on smaller, frictionless, single moving part pumps that have overcome the failures associated with earlier larger and more complicated models. However, the continued presence of drive-lines (which are the wires that exit the body) undermines the full potential these newer VADs can offer. Drive-lines are well recognized as a source for infection, increased morbidity, re-hospitalizations, and limit the movement that patients demand and deserve. Older, inductive based technologies used for wireless power are hampered by a short range of a few millimeters, alignment issues, and poor efficiency.

Figure 8.2 shows a sketch of the VAD connected to a patients heart. In this scenario, the drive-line has been replaced with the WREL system, allowing for a completely wireless and fully implanted solution.

Figure 8.3 shows the experimental set-up (panel A) consisting of the transmit unit made up of a single turn drive loop and multi-turn spiral coil. The transmitter is driven by an power amplifier (not shown) capable of automatic frequency tunning. The receiver loop and coil drive an RF-DC rectifier to convert the oscillating 13.56 MHz RF signal at to DC power, which is used to directly power the heart pump and/or to charge a back-up battery that would be implanted in the body. A battery clip was modified to accept power from the regulator (figure 8.3 panel B). The axial pump was set at 9400 rpms before being connected to the above system without any batteries and submerged in water. A series of 240 samples

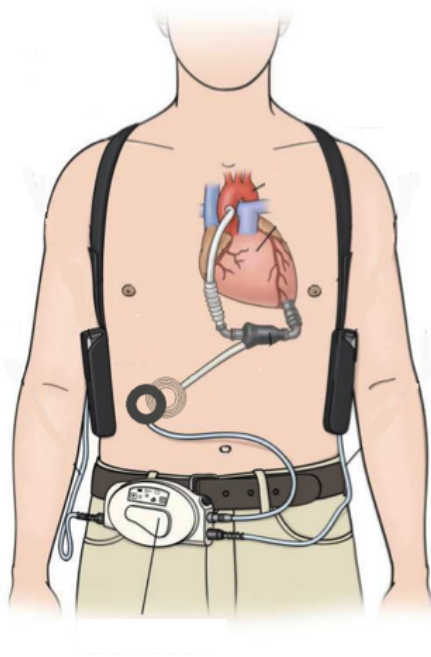


Figure 8.2: Sketch of the patient with a ventricular assist device wirelessly powered by a WREL system.

at 15 second intervals were collected at F=13.43 MHz and RF gain=2900.

The system ran the pump without any interruptions or failure of the circuitry. The pump worked without interruption even when the receiving coil diameter was reduced to 4.3cm (figure 8.3 panel C). The coil efficiency was 91.8%, the system efficiency was 79.2%, and the rectifier efficiency was 86.2%.

The WREL principle affords an exciting avenue to make a totally implantable VAD with the ability to power the device at a distance. The advantage of this system over the older induction based technology, is that it works totally tether free, which can have significant implications for reducing adverse events and improving the quality of life for the patient.

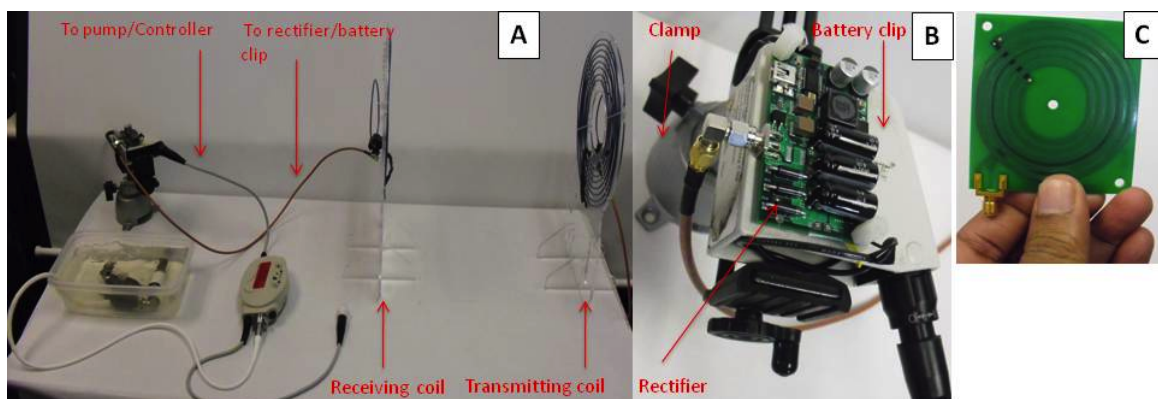


Figure 8.3: A: Experimental set up with transmitting and receiving coil, note the pump is in continuous operation. B: Modified battery clip held in place by a clamp, with the RF-DC rectifier mounted directly on the top and output connected to the pump controller. C: Depicts a small inner coil mounted on a PC board (4.3 cm in diameter) that was used to power the pump.

BIBLIOGRAPHY

- [1] Syed Ahson and Mohammad Ilyas. *RFID handbook : applications, technology, security, and privacy*. Boca Raton: CRC Press, 2008.
- [2] Chappell Brown. St lights up silicon led for cmos fab lines. EE Times., November 2011.
- [3] W.C. Brown. The history of power transmission by radio waves. *Microwave Theory and Techniques, IEEE Transactions on*, 32(9):1230–1242, Sep 1984.
- [4] W.C. Brown. The history of power transmission by radio waves. *Microwave Theory and Techniques, IEEE Transactions on*, 32(9):1230–1242, Sep 1984.
- [5] B.L. Cannon, J.F. Hoburg, D.D. Stancil, and S.C. Goldstein. Magnetic resonant coupling as a potential means for wireless power transfer to multiple small receivers. *Power Electronics, IEEE Transactions on*, 24(7):1819–1825, July 2009.
- [6] J.J. Casanova, Zhen Ning Low, and Jenshan Lin. A loosely coupled planar wireless power system for multiple receivers. *Industrial Electronics, IEEE Transactions on*, 56(8):3060–3068, Aug. 2009.
- [7] S. Cecil, G. Schmid, K. Lamedschwandner, J. Morak, G. Schreier, A. Oberleitner, and M. Bammer. Numerical assessment of specific absorption rate in the human body caused by nfc devices. pages 65 –70, apr. 2010.
- [8] NASA / Marshall Space Flight Center. Dryden flight research center, beamed laser power for uavs. www.nasa.gov/centers/dryden/news/FactSheets/FS-087-DFRC.html, October, 10 2003.
- [9] Hee-Jin Chae, Daniel J. Yeager, Joshua R. Smith, and Kevin Fu. Maximalist cryptography and computation on the WISP UHF RFID tag. In *Proceedings of the Conference on RFID Security*, July 2007.
- [10] H.L. Chan, K.W.E. Cheng, and D. Sutanto. A simplified neumann’s formula for calculation of inductance of spiral coil. In *Power Electronics and Variable Speed Drives, 2000. Eighth International Conference on (IEE Conf. Publ. No. 475)*, pages 69–73, 2000.
- [11] J. Chen. *Feedback Networks:theory and circuit application*. World Scientific Publishing Company, City, 2007.

- [12] Namjun Cho, Seong-Jun Song, Sunyoung Kim, Shiho Kim, and Hoi-Jun Yoo. A 5.1-mu;w uhf rfid tag chip integrated with sensors for wireless environmental monitoring. In *Solid-State Circuits Conference, 2005. ESSCIRC 2005. Proceedings of the 31st European*, pages 279 – 282, sept. 2005.
- [13] J. Choma and W. Chen. *Feedback networks: theory and circuit applications*. World Scientific, 2007.
- [14] Shane S. Clark, Jeremy Gummesson, Kevin Fu, and Deepak Ganesan. Towards autonomously-powered CRFIDs. In *Workshop on Power Aware Computing and Systems (HotPower 2009)*, October 2009.
- [15] K.L. Corum and J.F. Corum. Rf coils, helical resonators and voltage magnification by coherent spatial modes. In *Telecommunications in Modern Satellite, Cable and Broadcasting Service, 2001. TELSIKS 2001. 5th International Conference on*, volume 1, pages 339 –348 vol.1, 2001.
- [16] Alexei Czeskis, Karl Koscher, Joshua R. Smith, and Tadayoshi Kohno. Rfids and secret handshakes: defending against ghost-and-leech attacks and unauthorized reads with context-aware communications. In *Proceedings of the 15th ACM conference on Computer and communications security*, CCS ’08, pages 479–490, New York, NY, USA, 2008. ACM.
- [17] D.M. Dobkin and S.M. Weigand. Environmental effects on rfid tag antennas. In *Microwave Symposium Digest, 2005 IEEE MTT-S International*, page 4 pp., june 2005.
- [18] Federal Communication Commission (FCC). Title 47: Telecommunication, part 15 radio frequency devices. www.fcc.gov, January, 31 2011.
- [19] Klaus Finkenzeller. *RFID Handbook : Fundamentals and Applications in Contactless Smart Cards and Identification*. John Wiley & Sons, second edition, May 2003.
- [20] N.H. Fletcher and T.D. Rossing. *The Physics of Musical Instruments*. Springer-Verlag, 1998.
- [21] Peter Harrop and Raghu Das. Organic and printed electronics in north america (2009). *Iidtechex*, January, 7 2009.
- [22] N. Henze, M. Weitz, P. Hofmann, C. Bendel, J. Kirchhof, and H. Fruchting. Investigation of planar antennas with photovoltaic solar cells for mobile communications. In *Personal, Indoor and Mobile Radio Communications, 2004. PIMRC 2004. 15th IEEE International Symposium on*, volume 1, pages 622 – 626 Vol.1, sept. 2004.
- [23] ICNIRP. Guidelines for limiting exposure to time-varying electric, magnetic and electromagnetic fields (up to 300 GHz). *Health Physics*, 74:494–522, 1998.

- [24] PowerMat Inc. www.powermat.com, November 2011.
- [25] Institute of Electrical and Electronics Engineers (IEEE) SCC28. *IEEE Std C95.1 IEEE Standard for Safety Levels with Respect to Human Exposure to Radio Frequency Electromagnetic Fields, 3 kHz to 300 GHz*. IEEE Standards Department, International Committee on Electromagnetic Safety, The Institute of Electrical and Electronics Engineers, Inc. 3 Park Avenue, New York, NY 10016-5997, USA, 1999.
- [26] Institute of Electrical and Electronics Engineers (IEEE) SCC28. *ANSI/IEEE C95.1-1992, IEEE Standard for Safety Levels with Respect to Human Exposure to Radio Frequency Electromagnetic Fields, 3 kHz to 300 GHz*. IEEE Standards Department, International Committee on Electromagnetic Safety, The Institute of Electrical and Electronics Engineers, Inc. 3 Park Avenue, New York, NY 10016-5997, USA, 2005.
- [27] Institute of Electrical and Electronics Engineers (IEEE) SCC28. *IEEE Std C95.1 - 2005 IEEE Standard for Safety Levels with Respect to Human Exposure to Radio Frequency Electromagnetic Fields, 3 kHz to 300 GHz*. IEEE Standards Department, International Committee on Electromagnetic Safety, The Institute of Electrical and Electronics Engineers, Inc. 3 Park Avenue, New York, NY 10016-5997, USA, 2005.
- [28] Fung-Jou Chen Eric F. Wagner Jeffrey D. Lindsay, Heriberto F. Velazquez. Activating a data tag by load or orientation or user control. (USA Patent: 7151455), December 2006.
- [29] D. Kajfez and E.J. Hwan. Q-factor measurement with network analyzer. *Microwave Theory and Techniques, IEEE Transactions on*, 32(7):666–670, Jul 1984.
- [30] Carl L Dohrman Kamesh Chilukuri, Michael J Mori and Eugene A Fitzgerald. Monolithic cmos-compatible algainp visible led arrays on silicon on lattice-engineered substrates (soles). *Semiconductor Science and Technology*, 22(2):29–34, February 2007.
- [31] M. Kanda, D.O. McCoy, M.A. Schamberger, and Q. Balzano. Measurement of localized specific absorption rate (sar) for contactless smartcard readers operating in the hf band. *Electromagnetic Compatibility, IEEE Transactions on*, 40(4):370 –376, nov. 1998.
- [32] Aristeidis Karalis, J.D. Joannopoulos, and Marin Soljacic. Efficient wireless non-radiative mid-range energy transfer. *Annals of Physics*, 323(1):34 – 48, 2008. January Special Issue 2008.
- [33] Karl F. Kiefer. Combination photovoltaic cell and rf antenna and method. (U.S. Patent 6 590 150), July 8th 2003.
- [34] Yong-Hae Kim, Seung-Youl Kang, Myung-Lae Lee, Byung-Gon Yu, and Taehyoung Zyung. Optimization of wireless power transmission through resonant coupling. In *Compatibility and Power Electronics, 2009. CPE '09.*, pages 426–431, May 2009.

- [35] F. Kocer and M.P. Flynn. A new transponder architecture with on-chip adc for long-range telemetry applications. *Solid-State Circuits, IEEE Journal of*, 41(5):1142 – 1148, may 2006.
- [36] Andre Kurs, Aristeidis Karalis, Robert Moffatt, J. D. Joannopoulos, Peter Fisher, and Marin Soljacic. Wireless Power Transfer via Strongly Coupled Magnetic Resonances. *Science*, 317(5834):83–86, 2007.
- [37] Andre Kurs, Aristeidis Karalis, Robert Moffatt, J. D. Joannopoulos, Peter Fisher, and Marin Soljacic. Wireless Power Transfer via Strongly Coupled Magnetic Resonances. *Science*, 317(5834):83–86, 2007.
- [38] Zhen Ning Low, R.A. Chinga, R. Tseng, and Jenshan Lin. Design and test of a high-power high-efficiency loosely coupled planar wireless power transfer system. *Industrial Electronics, IEEE Transactions on*, 56(5):1801–1812, May 2009.
- [39] J.O. McSpadden and J.C. Mankins. Space solar power programs and microwave wireless power transmission technology. *Microwave Magazine, IEEE*, 3(4):46–57, Dec 2002.
- [40] R. G. Medhurst. H. f. resistance and self-capacitance of single-layer solenoids. *Wireless Engineering*, 24:35–43, 1947.
- [41] Microchip Technology Inc., 2355 West Chandler Blvd, Chandler, AZ 85224-619. *MCRF202 - 125 kHz Passive RFID Device with Sensor Input*, 2003.
- [42] R. Mongia, P. Bhartia, and I.J. Bahl. *RF and Microwave Coupled-Line Circuits*. Artech, 2 edition, 1999.
- [43] Rajesh Mongia. *Rf and Microwave Coupled-Line Circuits*. Artech House Publishers, City, 2007.
- [44] Jagadish Nadakuduti, Mark Douglas, Myles Capstick, Sven Kühn, and Niels Kuster. Application of current density sensor for assessment of em exposure from energy saving bulbs. *Submitted to Bioelectromagnetics*, August 2010.
- [45] National Council on Radiation Protection and Measurements (NCRP). *Biological Effects and Exposure Criteria for Radiofrequency Electromagnetic Fields, Report 86*. NCRP, 1986.
- [46] J.P O'Loughlin. Circuit and electromagnetic system design notes, note 42. Technical report, University of New Mexico, 1998.
- [47] Joseph A. Paradiso and Thad Starner. Energy scavenging for mobile and wireless electronics. *IEEE Pervasive Computing*, 4:18–27, January 2005.

- [48] M. Philipose, J.R. Smith, B. Jiang, A. Mamishev, Sumit Roy, and K. Sundara-Rajan. Battery-free wireless identification and sensing. *Pervasive Computing, IEEE*, 4(1):37 – 45, jan.-march 2005.
- [49] Matthai Philipose, Kenneth P, Mike Perkowitz, Donald J. Patterson, Dieter Fox, Henry Kautz, and Dirk Hhnel. Inferring activities from interactions with objects. *IEEE Pervasive Computing*, 3:50–57, 2004.
- [50] Xianming Qing and Zhi Ning Chen. Proximity effects of metallic environments on high frequency rfid reader antenna: Study and applications. *Antennas and Propagation, IEEE Transactions on*, 55(11):3105 –3111, nov. 2007.
- [51] J. Riekki, T. Salminen, and I. Alakarppa. Requesting pervasive services by touching rfid tags. *Pervasive Computing, IEEE*, 5(1):40 – 46, jan.-march 2006.
- [52] A. Sample and J.R. Smith. Experimental results with two wireless power transfer systems. In *Radio and Wireless Symposium, 2009. RWS '09. IEEE*, pages 16–18, Jan. 2009.
- [53] A.P. Sample, D.A. Meyer, and J.R. Smith. Analysis, experimental results, and range adaptation of magnetically coupled resonators for wireless power transfer. *Industrial Electronics, IEEE Transactions on*, 58(2):544 –554, February 2011.
- [54] A.P. Sample, D.J. Yeager, P.S. Powledge, A.V. Mamishev, and J.R. Smith. Design of an rfid-based battery-free programmable sensing platform. *Instrumentation and Measurement, IEEE Transactions on*, 57(11):2608–2615, Nov. 2008.
- [55] A.P. Sample, D.J. Yeager, P.S. Powledge, and J.R. Smith. Design of a passively-powered, programmable sensing platform for uhf rfid systems. *RFID, 2007. IEEE International Conference on*, pages 149 –156, march 2007.
- [56] A.P. Sample, D.J. Yeager, and J.R. Smith. A capacitive touch interface for passive rfid tags. In *RFID, 2009 IEEE International Conference on*, pages 103 –109, april 2009.
- [57] David Schneider. A critical look at wireless power. *IEEE Spectrum*, 47(5):34–39, May 2010.
- [58] S.V. Shynu, M.J. Roo Ons, M.J. Ammann, S. McCormack, and B. Norton. Dual band a-si:h solar-slot antenna for 2.4/5.2ghz wlan applications. In *Antennas and Propagation, 2009. EuCAP 2009. 3rd European Conference on*, pages 408 –410, march 2009.
- [59] Will Stewart. APPLIED PHYSICS: The Power to Set You Free. *Science*, 317(5834):55–56, 2007.

- [60] Nikola Tesla. Apparatus for transmitting electrical energy. (Patent 1,119,732), 1, December 1914.
- [61] T. Unander, H.-E. Nilsson, and B. Oelmann. Printed touch sensor for interactive packaging and display. In *Polymers and Adhesives in Microelectronics and Photonics, 2007. Polytronic 2007. 6th International Conference on*, pages 12 –17, 16 2007-yearly 18 2007.
- [62] S. Vaccaro, J.R. Mosig, and P. de Maagt. Two advanced solar antenna "solant" designs for satellite and terrestrial communications. *Antennas and Propagation, IEEE Transactions on*, 51(8):2028 – 2034, aug. 2003.
- [63] J. Vujic, A. Marincic, M. Ercegovac, and B. Milovanovic. Nikola tesla: 145 years of visionary ideas. In *Telecommunications in Modern Satellite, Cable and Broadcasting Service, 2001. TELSIKS 2001. 5th International Conference on*, volume 1, pages 323 –326 vol.1, 2001.
- [64] R. Vyas, V. Lakafosis, Z. Konstas, and M.M. Tentzeris. Design and characterization of a novel battery-less, solar powered wireless tag for enhanced-range remote tracking applications. In *Microwave Conference, 2009. EuMC 2009. European*, pages 169 –172, 29 2009-oct. 1 2009.
- [65] A. Woodruff, K. Anderson, S. Mainwaring, and R. Aipperspach. Portable, but not mobile: A study of wireless laptops in the home. *Proc. Pervasive*, pages 216–233, May 2007.
- [66] D.J. Yeager, P.S. Powledge, R. Prasad, D. Wetherall, and J.R. Smith. Wirelessly-charged uhf tags for sensor data collection. In *RFID, 2008 IEEE International Conference on*, pages 320 –327, april 2008.
- [67] Q Yuan, Y Chen, L Li, and K Sawaya. Numerical analysis on transmission efficiency of evanescent resonant coupling wireless power transfer system. *IEEE Transactions on Antennas and Propagation*, 58(5):1751–1758, 2010.
- [68] Chunbo Zhu, Kai Liu, Chunlai Yu, Rui Ma, and Hexiao Cheng. Simulation and experimental analysis on wireless energy transfer based on magnetic resonances. In *Vehicle Power and Propulsion Conference, 2008. VPPC '08. IEEE*, pages 1–4, Sept. 2008.

VITA

Alanson Sample earned his Ph.D. in Electrical Engineering from the University of Washington in June of 2011. He received his M.S. in 2008 and B.S. in 2005, both from the University of Washington. Alanson is a member of the Sensor Systems Lab, which is directed by Joshua R. Smith. Throughout his graduate studies, Alanson has worked as a full time employee at Intel Labs Seattle (either by internship or by multi-year contract). Intels Seattle lab focuses on exploring context aware and sensor driven computing systems that are integrated seamlessly into daily life.

Alanson has authored several articles on RFID, wireless power, energy harvesting, and robotics. His research interests lie broadly in the areas of RF engineering and integrated circuit design, including: antenna theory and design, energy harvesting, wirelessly powered systems, transceiver design, and design of novel sensing systems.